Summer 7-2013

Velocity Measurements of the Flow over a Gate-Controlled Weir Structure

Mohamed M. Jalloh
University of Nebraska-Lincoln, mohamed.jalloh31@huskers.unl.edu

Velocity Measurements of the Flow over a Gate-Controlled Weir Structure

by

Mohamed Mamadu-Jan Jalloh

A THESIS

Presented to the Faculty of

The Graduate College at the University of Nebraska

In Partial Fulfillment of the Requirements

For the Degree of Master of Science

Major: Civil Engineering

Under the Supervision of Professor David Admiraal

Lincoln, Nebraska

July 2013

Velocity Measurements of the Flow Over a Gate-Controlled Weir Structure

Mohamed Mamadu-Jan Jalloh,M.S.

University of Nebraska, 2013

Advisor: David Admiraal

The South Florida Water Management District (SFWMD) uses G304 control structures to manage flow into and out of a large storm-water treatment area (STA). These structures consist of a lateral unsuppressed weir, a sluice gate and a corrugated culvert for flow control and transfer through an embankment. For better flow control in the STAs, it is imperative to accurately measure the discharge through the G304 control structures and to determine the approach velocity over the weir for different field scenarios.

Flow behavior of the G304 structure was examined in a prototype during two days of testing for two canal headwater elevations. The complexity of the inflow over the weir and the difficulty and cost of varying flow in the field made it desirable to use a model to further investigate the structure. Thus, a 1:6.26 Froude-based physical model was used to simulate additional flow conditions over the weir.

Large-Scale Particle Tracking Velocimetry (LPTV) was used to determine surface velocity contours for both the prototype and the model. By applying standard assumptions about the velocity profiles in the flow, the mean velocity and discharge were calculated from the surface velocity measurements. These measurements were compared with discharge measurements using an Acoustic Doppler Flow Meter (ADFM) and an array of Acoustic Doppler Velocimeters (ADVs) in the prototype and a weigh tank in the model.

For the prototype tests, the LPTV discharge measurements upstream of the weir were in close agreement with the discharge measured using ADFM and ADV devices. The results also showed that LPTV discharge measurements directly above the weir were very low. Laboratory results confirmed that LPTV is a good method for estimating discharge over this type of structure, especially when the discharge is measured well-upstream of the weir where the velocity distributions approach uniform flow behavior. It

was also observed that wind and side abutments had a significant influence on the measured surface velocity and the distribution of flow over the weir.

Dedication

Dedicated to my late mother; Haja Umu Jalloh

Acknowledgements

I would like to take this opportunity to express my deepest appreciation to the Fulbright Program for giving me this opportunity to pursue graduate studies here in the US. I would like to give a special thanks and appreciation to Dr. David Admiraal, without your persistent help, tolerance and guidance this thesis would not have been possible. I must also thank you Dr David Admiraal for the help and support you continue give my family and me. My admiration of your work in research and teaching would greatly influence my career goals.

My sincerest thanks and love goes to my late mum without your hard work and perseverance education would not have been a possibility for me. We both dreamt about this moment for many years, it sad you are not here to celebrate with me but I know you are proud of me. My appreciation also goes to my brothers and sisters for your tremendous support and sacrifice through adversity, without each of you I would not have made it this far.

To my sons Abdul Razak and Abdul Raheem, I owe my determination to succeed to you people. I also want to thanks you for the joy and happiness you brought into my life and your understanding for the long hours I would spend doing my schoolwork especially when you people want to play. To my wife I want to thank you for you love and support.

I would like to also thank the following graduate students for your role in helping me throughout this journey.

Clark: Those huskers game ticket meant a lot to me, I thank you very much. I am also grateful that you were always there for me educationally and socially, if it was not for you school would have been boring.

Reinaldo: Thanks you I thank you for all your help in data collection and analysis. If it was not for you my work would have been very tedious, but your continuous support made things easier. I am also grateful for all the times we spent together of school those were fun times.

Miles: Thanks for your patience and time listening to my boring conservations and most importantly you willingness to always assist me and answer foolish questions. I learnt a lot from you.

Alex: Thanks for bring the fun to school; they were very helpful especially in stressful time.

Finally and most importantly, I must recognize God for giving me the opportunity of life and for providing me with the strength, determination and wisdom through my quest for higher learning. Without you this journey would not have begun.

Table of Contents

Dedication i
Acknowledgements ii
Table of Contents iv
List of Figures vii
List of Tables xii
Chapter 1. Introduction 1
1.1 Background 1
1.2 Objectives 4
1.3 Thesis Chapter Overview 5
Chapter 2. Literature Review 6
2.1 Introduction 6
2.2 Weirs 6
2.3 Sharp Crested Weirs 7
2.4 Broad-Crested Weir 8
2.5 Suppressed Rectangular Weir 10
2.6 Discharge Coefficient for Sharp-Crested Weir 12
2.7 Discharge Coefficient of Broad-Crested Weirs 15
2.8 Weirs with End Contractions 16
2.9 Velocity Profiles of Sharp-Crested Weirs 18
2.10 Velocity Profiles of Broad-Crested Weirs 20
2.11 Side Weirs 22
2.12 Particle Tracking Velocimetry 33
2.12.1 History 33
2.12.2 Image Velocimetry 34
2.12.3 Particle Image Velocimetry 37
2.12.4 Particle Tracking Velocimetry 38
2.12.5 Effects of Wind-Induced Water Currents on Surface Velocity 42
2.13 Summary 45
Chapter 3. Instruments and Tools 46

3.1 Introduction 46
3.2 High Definition Digital Camcorders 46
3.3 Weigh tank 47
3.4 Acoustic Doppler Flow Meter (ADFM) - Pro 20 Velocity Profiler 48
3.5 SonTek 16-MHz Acoustic Doppler Velocimeter (ADV) 50
3.6 Additional Tools 51
3.7 Flow Field Captor Multi-Dimensional PIV/PTV Analysis Program 51
3.7.1 Preprocessing Image Filters in FFCMD 52
3.7.2 FFCMD Image Processing 55
3.7.3 Post processing Filters in FFCMD 59
3.7.4 Ancillary Functions of FFCMD 61
3.7.5 Vector Plotting 62
3.7.6 Contour and Program Settings 63
Chapter 4. Prototype and Laboratory Experiments 64
4.1 Introduction 64
4.2 Prototype Measurements 64
4.2.1 Stage Measurements 65
4.2.2 ADFM Measurements 68
4.2.3 ADV Measurements 68
4.2.4 Large-Scale Particle Tracking Velocimetry Measurements 71
4.2.5 Pre-filtering LPTV Images with FFCMD 72
4.2.6 Calculation of the Pixel-to-Distance Ratio 76
4.2.7 Vector Output Files 78
4.2.8 Application of Velocity Filters during Post-Processing 78
4.2.9 Water Surface Profile Measurements 87
4.3 Laboratory Measurements 91
4.3.1 G304 Model Construction 91
4.3.2 Experimental Procedure 95
4.3.3 Calculation of the Pixel-to-Distance Ratio 96
4.3.4 Discharge Measurements 97
4.3.5 Model LPTV Measurements 98

4.4 Field and Laboratory Average Velocity and Discharge Computations 99
4.4.1 Depth Averaged Velocities 99
4.4.2 Average Surface Velocity Estimations 103
4.4.3 Discharge Calculations 106
Chapter 5. Results and Discussion 108
5.1 Introduction 108
5.2 Surface Velocity Measurements using LPTV 108
5.3 Average Surface Velocity 116
5.4 Measured Discharges 116
5.4.1 Field Discharge 117
5.4.2 Laboratory Discharge Measurements 121
5.5 Prototype Abutment Effects 123
Chapter 6. Conclusions 128
6.1 Overview 128
6.2 General Observations 128
6.3 Future Work 131
References 133
Appendix A. High Density Vector Plots in the Prototype 137
Appendix B. Contours of Surface Velocity Magnitudes in the Prototype 139
Appendix C. Locally Averaged Velocity Transects in the Prototype 141
Appendix D. High Density Vector Plots in the Model 145
Appendix E. Contours of Surface Velocity Magnitudes in the Model 149
Appendix F. Locally Averaged Velocity Transects in the Model 153

List of Figures

Figure 1.1 STA -1W structures and flow (after Gonzalez, J. 2007) 1
Figure 1.2 G304 head box and culvert layout (after Gonzalez, 2005)..... 2
Figure 1.3 Photographs of the (a) supply canal and head box, and (b) the culvert outlet .. 2
Figure 2.1 Sharp-crested weir geometry..... 7
Figure 2.2 Broad-crested weir..... 9
Figure 2.3 Suppressed weirs with length of crest equal to channel width..... 11
Figure 2.4 Comparison of equations for a suppressed sharp crested weir (from Ackers, P. 1978)..... 14
Figure 2.5 Weir with end contractions (Ackers 1978)..... 16
Figure 2.6 Limiting proportions of a fully contracted weir (Finnemore and Franzini, 2002) 17
Figure 2.7 Definition sketch showing section of pressure and velocity measurement (Rajaratnam and Muralidhar 1971)..... 18
Figure 2.8 Velocity distributions at (a) section O-O, (b) at the crest (Rajaratnam and Muralidhar, 1971) 19
Figure 2.9 Free surface velocity profiles (Hager and Schwalt, 1994) 20
Figure 2.10 Lateral velocity profiles upstream and at selected sections over the weir crest (Hager and Schwalt, 1994) 21
Figure 2.11 Velocity distributions along a broad-crested weir (Felder and Chanson, 2012) 22
Figure 2.12 Definition diagram of side weir, (Subramanya and Awasthy 1972)..... 23
Figure 2.13 Types of flow regime for side weirs: (a) subcritical flow; (b) supercritical; (c) hydraulic jump (Borghei et al. 1999)..... 24
Figure 2.14 Definition sketch of side weir (Bagheri and Heidarpour, 2011) 27
Figure 2.15 Distribution of longitudinal velocity (V_x) alongside weir (Bagheri and Heidarpour, 2011)..... 28
Figure 2.16 Longitudinal velocity (Vx) profiles (Bagheri and Heidarpour, 2011) 29
Figure 2.17 Distribution of vertical velocity (Vy) alongside weir (Bagheri and Heidarpour, 2011)..... 29

Figure 2.18 Vertical velocity (Vy) profiles (Bagheri and Heidarpour, 2011) 30
Figure 2.19 Distribution of lateral velocity (Vz) alongside weir (Bagheri and Heidarpour, 2011) 31
Figure 2.20 Lateral velocity (V_z) profiles (Bagheri and Heidarpour, 2011)..... 31
Figure 2.21 Variation of dimensionless local discharge along the crest of side weir (Bagheri and Heidarpour, 2011) 33
Figure 2.22 (a) Shows a simple nearest neighbor mismatch. (b) Shows a particle that has not been detected in the second frame. Full and open circles represent particles in the first and second frames respectively, whereas the full rectangles denote the current estimate (Ruhnau et al., 2005) 41
Figure 2.23 Effect of wind-induced current on water surfaces (Tang el al.1978) 43
Figure 2.24 Plot of ratio of drift velocities to mean wind speed against mean wind speed (after Tang et.al, 1978)..... 44
Figure 3.1 Weigh tank mounted on a Toledo scale 48
Figure 3.2 Pulse Doppler velocity profiling (Teledyne Isco 2009) 49
Figure 3.3 ADV transmitting and receiving probes..... 50
Figure 3.4 Image filter window 53
Figure 3.5 Point rejection window..... 54
Figure 3.6 Fixed pixel/distance ratio calculator..... 55
Figure 3.7 Particles in first and second image frames 57
Figure 3.8 Superimposed first and second image 58
Figure 3.9 Possible particle matches..... 58
Figure 3.10 Velocity filter dialog window..... 60
Figure 3.11 Image velocimetry batch operations..... 62
Figure 3.12 Special analysis tools batch operations 62
Figure 3.13 Contour interpolation settings window 63
Figure 4.1 Depiction of an ADFM installation and operation in a pipe flow (Teledyne Isco 2009)..... 68
Figure 4.2 End view of G304 outlet depicting transect along which velocity measurement was taken..... 69
Figure 4.3 Camera plane view of the G304 structure 71

Figure 4.4 Prototype G304 LPTV image prior to filtering 74
Figure 4.5 Prototype G304 LPTV image after it has been filtered 74
Figure 4.6 Survey rod used for pixel/distance estimation (low head tests, left abutment) 77
Figure 4.7 Survey rod used for pixel/distance estimation (low head tests, right abutment) 78
Figure 4.8 Vectors plotted for prototype Test B5 before applying vector filters 79
Figure 4.9 Vectors marked red for deletion after applying universal and regional filters (Test B5) 81
Figure 4.10 Vector plot after applying universal and regional filters(Test B5)..... 82
Figure 4.11 Final filtered Test B5 (4.0 ft gate opening - south side)..... 83
Figure 4.12 Final filtered Test B5 (4.0 ft gate opening - north side) 84
Figure 4.13 Overlapping north and south images with the abutments aligned face to face 85
Figure 4.14 Combined images representing the entire G304 weir structure 85
Figure 4.15 Velocity distributions over the entire G304 weir structure for Test A5..... 86
Figure 4.16 Depth of water in canal upstream of weir above apron and above weir face 89
Figure 4.17 Plan view of the G304 weir structure 89
Figure 4.18 Plan view of model layout (Admiraal, D.M. 2009)..... 91
Figure 4.19 Profile view of model layout (Admiraal, D.M. 2009) 91
Figure 4.20 Model inlet weir box 93
Figure 4.21 Head tank and model culvert 93
Figure 4.22 Metal framed mesh used for estimating pixel sizes (model tests)..... 97
Figure 4.23 Velocity vectors for model Test 10 after filtering 99
Figure 4.24 Average velocity calculation locations for prototype measurements..... 102
Figure 4.25 Average velocity calculation locations for model measurements 103
Figure 4.26 Example grid cells at the prototype weir face 105
Figure 4.27 Average velocity distributions for field Test B5 106
Figure 5.1 Surface velocity distribution (Test A5) 109
Figure 5.2 Surface velocity distribution (Test B5) 109
Figure 5.3 Surface velocity distributions (Model Test 8) 109
Figure 5.4 velocity contour plot for prototype Test A5 110

Figure 5.5 Surface velocity contour plot for prototype Test B5. 110
Figure 5.6 Surface velocity contour plot for model Test 8 110
Figure 5.7 Wind speed and direction on February 10, 2009 at PBI (after Weather Underground, 2013 114
Figure 5.8 Wind speed and direction on February 12, 2009 at PBI (after Weather Underground, 2013) 114
Figure 5.9 Orientation of canal, weir structure and wind-direction (at the time of testing) with respect to north axis 115
Figure 5.10 Comparison of LPTV Discharges measured above the weir and upstream of weir with ADFM discharges measured inside the culvert 119
Figure 5.11 Comparison of LPTV discharges measured above the weir and upstream of weir with ADV discharges measured inside the culvert 120
Figure 5.12 Comparison of PTV discharges measured above the weir and upstream of weir with discharges measured using a weigh tank at the culvert outlet 122
Figure 5.13 Discharge measurements across eight equal cross-sectional areas 123
Figure 5.14 Distribution of discharge over weir for low head tests..... 126
Figure 5.15 Distribution of discharge over weir for high head tests 126
Figure A.1 Surface velocity distribution plots for the prototype for (a) Test A2, (b) Test A3, (c) Test A4, (d) Test A5, and (e) Test A6 137
Figure A.2 Surface velocity distribution plots for the prototype for (a) Test B2, (b) Test B3, (c) Test B4, (d) Test B5, and (e) Test B6 138
Figure B.1 Surface velocity contour plots for the prototype for (a) Test A2, (b) Test A3, (c) Test A4, (d) Test A5, and (e) Test A6 139
Figure B.2 Surface velocity contour plots for the prototype for (a) Test B2, (b) Test B3, (c) Test B4, (d) Test B5, and (e) Test B6..... 140
Figure C.1 Average surface velocity plots for the prototype for (a) Test A2, (b) Test A3, (c) Test A4 141
Figure C.2 Average surface velocity plots for the prototype for (a) Test B2, (b) Test B3, (c) Test B4..... 143
Figure D.1 Surface velocity distribution plots for the prototype for (a) Test 1, (b) Test 2, (c) Test 3 145

Figure E.1 Surface velocity distribution plots for the prototype for (a) Test 1, (b) Test 2, (c) Test 3 149
Figure F.1 Average surface velocity plots for the prototype for (a) Test 1, (b) Test 2, (c) Test 3 153

List of Tables

Table 2.1 Experimental data associated with a sharp-crested weir (Rajaratnam and Muralidhar, 1971) 19
Table 2.2 Side weir discharge co-efficient presented by various researchers 25
Table 2.3 Summary of model characteristics and testing conditions (Bagheri and Heidarpour, 2011) 28
Table 2.4 Ratio of drift velocities to mean speed velocities reported by several researchers (Tang et al 1978) 44
Table 4.1 Stage and discharge data summary for February 10, 2009 66
Table 4.2 Stage and discharge data summary for February 12, 2009 67
Table 4.3 Distance-To-Water surface measurements 87
Table 4.4 Depth of water above the apron and above the weir at locations U and A 90
Table 4.5 Experimental model conditions 96
Table 5.1 Wind speed and direction for the prototype tests 114
Table 5.2 Prototype estimated discharges 118
Table 5.3 Model discharge measurements 121
Table 5.4 Percentages of total flow over the weir across four equal cross sections 125

Chapter 1. **Introduction**

1.1 Background

The South Florida Water Management District (SFWMD) manages the flow into and out of several very large storm-water treatment areas (STAs) with a variety of flow control structures. The operational layout of one such STA, STA-1W, is depicted in Figure 1.1.

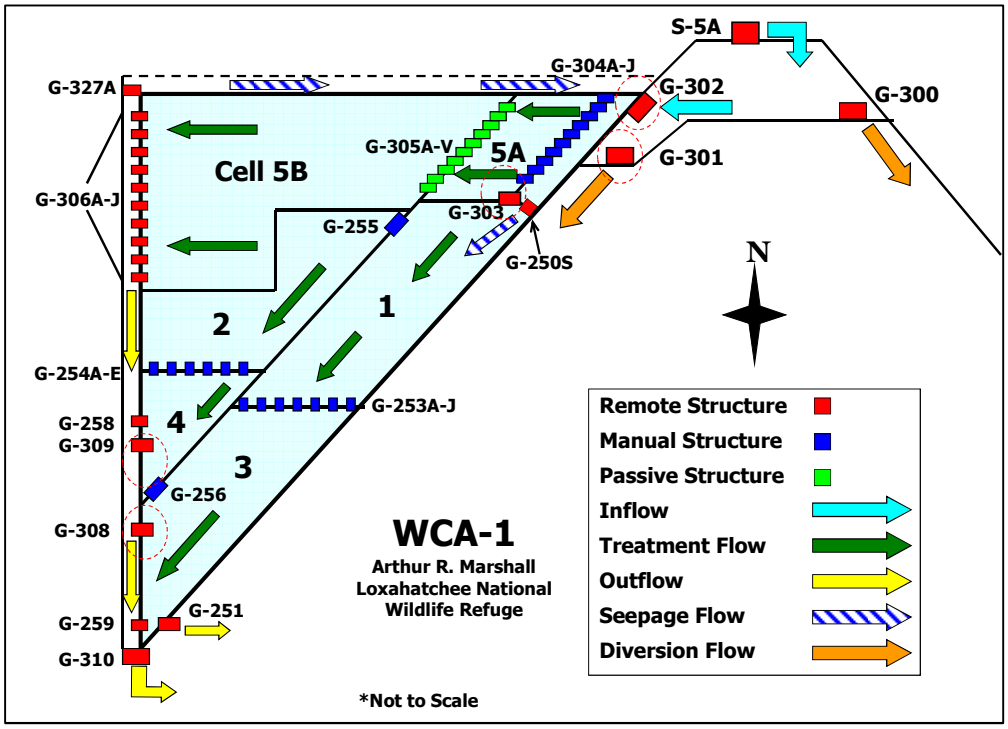

Figure 1.1 STA -1W structures and flow (after Gonzalez, J. 2007)

One set of hydraulic structures identified in Figure 1.1 that is of particular interest to SFWMD is the set of G304 structures; these structures are symbolically shown as blue rectangles in Figure 1.1. These structures deliver flow from a distribution canal to Cell 5A of the STA. Each G304 structure consists of a side weir with abutments, a flow control sluice gate and a circular corrugated culvert to transfer water through an embankment from the supply canal to treatment cell 5A. Multiple structures are necessary to evenly deliver the flow into the treatment cell over a wide area. A diagram

of the profile of a G304 structure is given in Figure 1.2, and photographs of the inlet and outlet of one of the G304 structures are given in Figure 1.3.

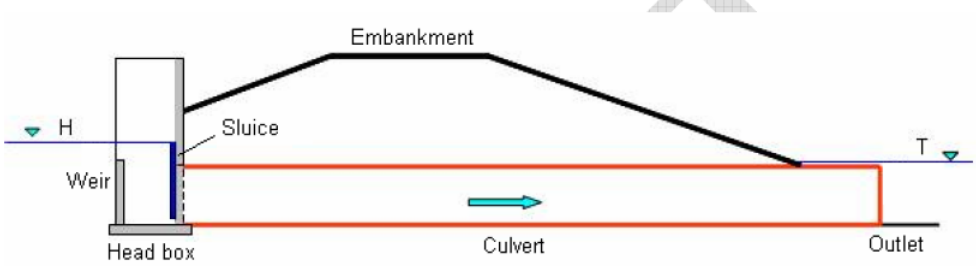

Figure 1.2 G304 head box and culvert layout (after Gonzalez, 2005)

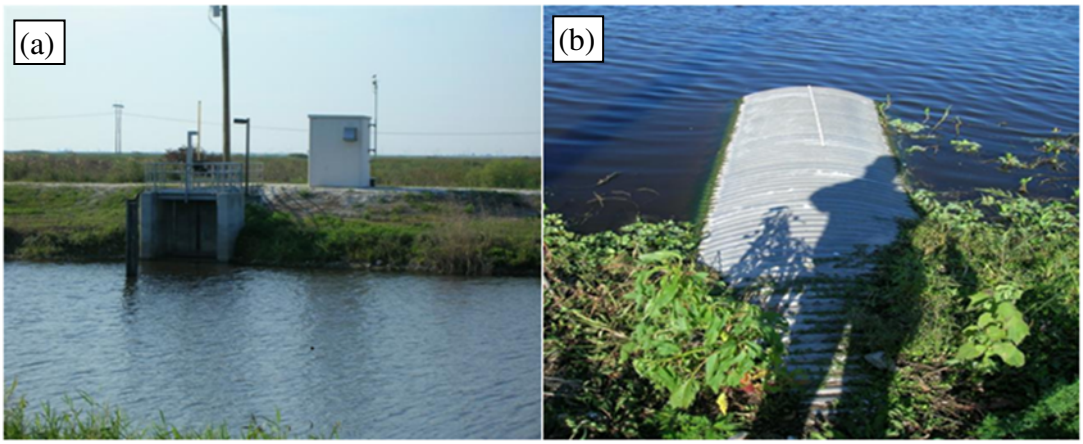

Figure 1.3 Photographs of the (a) supply canal and head box, and (b) the culvert outlet

For regulatory purposes, it is imperative to accurately measure the discharge through the G304 structures. Understanding the velocity distribution upstream of the weir and inside the culvert for different field conditions is particularly relevant for assessing the accuracy of low-flow measurements. Flow through the structure may be controlled by the weir, the sluice gate, the culvert, or by a combination of these three components. The total discharge depends on the sluice gate opening, and head and tail water conditions on both sides of the structure. The complex nature of the flow over the weir together with the influence of the gate makes the use of conventional weir and culvert discharge estimation equations with standard discharge coefficients uncertain for some flow conditions.

Additionally, during low flows the G304 behaves as a broad-crested weir structure (see Section 2.4), and the accuracy of using broad crested weir formulas is questionable for discharge measurements. Thus, the equations require calibration and validation with field measurements.

SFWMD sometimes mounts Acoustic Doppler Flow Meters (ADFMs) inside the G304 culverts to get discharge measurements. However, it is possible that for some operating conditions the flow in the G304 culvert is not fully developed- even at the outlet of the culvert. This will potentially violate the operational principles of acoustic Doppler flow meters (ADFM) or other traditional flow measurement equipment used to measure flow rates inside the culvert and could yield inaccurate flow rate estimates from these devices. In this study, Large-scale Particle Tracking Velocimetry (LPTV) was used to measure the surface velocity of water flowing into a prototype G304 structure for a variety of flow and operating conditions. LPTV is a Velocimetry technique used to estimate the surface velocity of a flow by seeding the flow with tracer particles. The displacements of the individual particles between successive frames of a video of the flow are then estimated, and velocities are calculated by dividing particle displacements by the time difference between the two successive frames. By applying standard assumptions about the velocity profiles in the flow, the mean velocity can be estimated from the surface velocity measurements, and the discharge can be calculated for the flow (see Section 4.4.1 for detail explanation). The accuracy of the discharge estimates is often closely related to adequacy of the assumptions about the velocity profiles. In the present case, estimated discharges were compared to ADFM and acoustic Doppler velocimeter (ADV) measurements conducted for the same flow conditions.

Due to the complexity of the STA water system and the difficulty and cost of varying flow conditions in the prototype, a physical model was used to further investigate weir flows. A 1:6.26 scale Froude-based physical model of the G304 structure was built in the University of Nebraska-Lincoln Hydraulics Laboratory. Particle Tracking Velocimetry (PTV) was also used in the model to estimate surface velocities and discharges over a wide range of flow conditions. A weigh tank at the tail end of the structure was also used to measure the discharge over the weir, and the results were compared to corresponding PTV measurements. The effects of the abutment walls on the discharge over the weir were also studied.

1.2 Objectives

The objectives of this study were to:

1. Examine potential methods of accurately measuring discharge over the G304 weir structure,
2. Estimate discharges using Particle Tracking Velocimetry and compare the results to discharges measured with other devices for a wide range of flow conditions,
3. Better understand the velocity distribution upstream of the weir and inside the culvert for different field conditions,
4. Estimate weir approach velocities, and
5. Examine abutment and wind effects on the discharge over the weir.

1.3 Thesis Chapter Overview

This thesis is the result of research conducted at the University of Nebraska-Lincoln (UNL) Hydraulics Laboratory and at an SFWMD Storm water Treatment Area in partnership with the South Florida Water Management District. The research focuses on the measurement of velocity and discharge over a gate controlled weir structure and through a corrugated culvert. Chapter 2 is a review of literature related to the research. Chapter 3 describes the various instruments and tools used for this research. Whereas, Chapter 4 describes the applied measurement processes. Chapter 5 presents the results and discussion of the results from the data analysis. Finally, Chapter 6 summarizes the conclusions of the research and proposes future work that would supplement the results of this research.

Chapter 2. **Literature Review**

2.1 Introduction

This literature review covers relevant topics from previous research, including flow characteristics of weir structures, velocity distributions near and above weirs, and Particle Tracking Velocimetry (PTV).

2.2 Weirs

A weir is an overflow structure that controls flow and often has a known relation between head and discharge. Weirs provide a simple method of discharge measurement. Empirical equations and/or graphical methods relate discharge to the height of water above the crest of the weir. As water flows over a weir, it forms a contracted and depressed shape called a nappe. According to King (1918), when the weir design is such that the nappe only touches the upstream edge of the crest, the weir is classified as a sharp-crested or thin plate weir. When the design is such that the weir crest is broad in the direction of the flow and the upstream head is small relative to the top weir breadth then it is classified as broad-crested (Bureau of Reclamation, 1997). Weirs are commonly designed as rectangular, trapezoidal, or triangular (V-shaped) cross-sections. Additionally, a weir can be designed to span the entire width of a channel, and is then referred to as suppressed (it has no end contractions). If the weir design includes a contraction in the channel width, the weir is called an unsuppressed weir (it has end contractions). For unsuppressed weirs, the nappe only touches the upstream edges of the weir and not the sides of the channel. When the elevation of the water surface downstream of the weir is below the weir crest, the weir is called an unsubmerged or free over-fall weir; otherwise, it is a submerged weir. Parameters that define the geometric

properties of weirs and that are applicable to both sharp and broad crested weirs are shown in Figure 2.1.

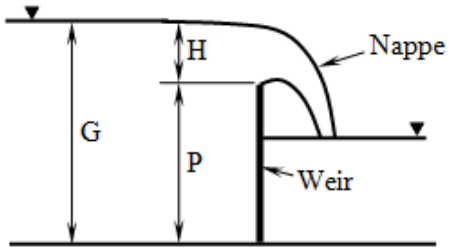

Figure 2.1 Sharp-crested weir geometry

In Figure 2.1, H represents the head measured above the weir crest, P is the height of the weir crest above the approach channel bed, and G is the total depth of the water in the upstream channel.

Another important weir parameter is the approach velocity. According to the U.S. Bureau of Reclamation, approach velocity is important, because it can effectively reduce the crest length and/or head and therefore can change weir calibration.

2.3 Sharp Crested Weirs

Sharp crested rectangular weirs are smooth, planar and mounted normal to the direction of the flow. The known geometry of the weir makes it possible to develop a rating curve between the depth of water behind the weir and the volumetric flow rate over the weir. The crest and end contractions of the weir have sharp edges that are beveled on one side to cause the nappe to spring clear of the weir (Mays, 2001). In general, the lower surface of the nappe should be ventilated to ensure that the pressure is atmospheric on all sides, and the downstream water surface level must be maintained well below the crest, to prevent interference with the ventilation. Ackers (1978) reported that failing to properly ventilate the nappe would result in a radical change of the flow. Since it is difficult to

accurately account for an unventilated nappe in weir discharge equations, it is better to make sure that the nappe remains ventilated for all flows.

Flow measurement with the weir requires that the flow regime upstream of the weir is subcritical and that as it approaches the weir, the free surface slowly decreases in elevation, resulting in acceleration of the flow. The flow becomes critical in the vicinity of the weir crest and continues to accelerate and discharge as supercritical flow (Cengel, 2010).

2.4 Broad-Crested Weir

A broad-crested weir, unlike a sharp-crested weir, is elongated in the direction of the flow over the weir, as shown in Figure 2.2. The streamlines above the elongated crest are parallel to the crest invert for a significant portion of the weir breadth, and hydrostatic pressure exists above the weir crest. The Bureau of Reclamation (1997) reported that a weir flow is truly broad-crested when the flow is such that the upstream head above the crest is between the limits of about 1/20 and 1/2 of the breadth of the crest (L_w). On the other hand, if the flow over a broad crest weir is such that the approach head is large enough to cause the flow to spring from the upstream corner, then the weir can be treated as a sharp-crested weir. There is no need for ventilation of a broad-crested weir, as the effect of tail water submergence is negligible as long as critical depth occurs at some location along the weir crest.

The broad-crested weir, like the sharp-crested weir, can take on many geometric forms. However, only the rectangular shaped broad-crested weir is of interest in this research. The reported advantages of the broad-crested weir include the simplicity of its geometry; its ease of construction and its robust nature (Ackers, 1978). Disadvantages

include a variable discharge coefficient and possible damage to the upstream corner, which will subsequently affect the calibration characteristic of the weir structure (Hager and Schwalt, 1994). However, it is also reported that even though the broad-crested weir is not the most reliable or the most accurate discharge measurement structure, it will produce fairly accurate results under certain specified conditions. These conditions include: (1) the upstream face must be vertical, (2) the upstream weir corner is sharp and has a smooth, horizontal corner, (3) the tail water submergence is below the modular limit, (4) the channel geometry is prismatic, (5) $\frac{H_t}{L_w}$ is within the limits given below and (6) the flow depth (d) above the weir is at least 50 mm. Note that H_t is the total head and is the sum of the head above the crest (H) and the approach velocity head.

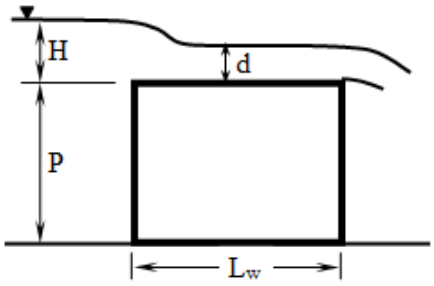

Figure 2.2 Broad-crested weir

According to Hager and Schwalt (1994), Govinda et al. (1963) categorized weirs based on the ratio of total head to weir length $\left(\frac{H_t}{L_w}\right)$ as follows:

$0 < \frac{H_t}{L_w} \leq 0.1$ long-crested weir

$0.1 < \frac{H_t}{L_w} \leq 0.4$ broad-crested weir

$0.4 < \frac{H_t}{L_w} \leq 1.5$ short-crested weir

$1.5 < \frac{H_t}{L_w}$ sharp-crested weir

The values of $\frac{H_t}{L_w}$ for the G304 structure for the field measurements reported in this thesis ranged from 0.57 to 1.16 for the two days of testing. Based on the ranges given above, the expected weir behavior is short-crested for the field tests presented herein. However, it is important to point out that backwater caused by the control gate and the tail water influenced flow over the weir structure for many of the flow tests, making unsubmerged weir equations invalid. For laboratory tests, values of $\frac{H_t}{L_w}$ ranged from 1.33 to 2.83. Thus, in the tests in the model, the behavior of the weir ranged from short crested to sharp-crested. In the case of laboratory tests, all of the tail waters were unsubmerged. Admiraal (2007), also noted that for normal operation, the G304 weir structure can behave either as a sharp-crested weir or a broad-crested weir, depending on the head in the supply canal.

2.5 Suppressed Rectangular Weir

A suppressed rectangular weir is one in which the length of the weir crest is the same as the width of the channel in which it is placed. In these types of weirs, the lateral flow condition is suppressed. Thus, there are no end contractions or abutments that can cause additional reduction of the effective flow cross section of the weir.

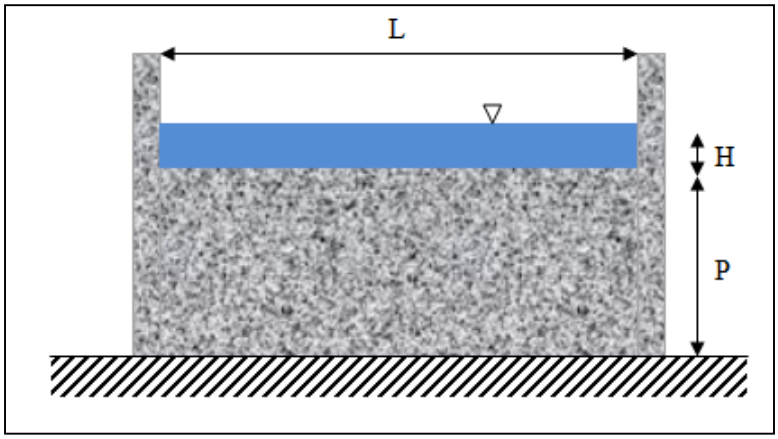

Figure 2.3 Suppressed weirs with length of crest equal to channel width

The theoretical formula for discharge over a rectangular weir is given by the following equation:

$$Q = {}^{2}/_{3}\sqrt{2g}\,LH^{3}/_{2} \tag{2.1}$$

where L is the length of the weir and g is the acceleration due to gravity. An empirical discharge coefficient (C_d) was introduced into Equation 2.1 to account for losses due to drawdown and subsequent contraction of the flow area. Hence, the total discharge equation becomes,

$$Q = {}^{2}/_{3}\,C_d\sqrt{2g}\,LH^{3}/_{2} \tag{2.1}$$

This equation is applicable for both sharp-crested and broad-crested rectangular weirs. However, the discharge coefficient C_d for a sharp-crested weir differs from that of a broad-crested weir. The discharge coefficient is determined and calibrated experimentally, but it is not completely constant. In addition, the discharge over a weir is affected by the approach velocity, which increases the discharge. According to Ackers (1978), the total head above the weir is given as:

$$\mathrm{H_t} = \mathrm{H} + \frac{\mathrm{Q}^2}{2\mathrm{gA}^2} \tag{2.2}$$

or in terms of the approach velocity V_a, and a non-unity energy coefficient α:

$$H_t = H + \frac{\alpha V_a^2}{2g} \tag{2.3}$$

Researchers have suggested many formulas for estimation of the discharge coefficient over standard shaped rectangular weir structures. The following two sections present results and compare the many formulas for both sharp and broad-crested weirs.

2.6 Discharge Coefficient for Sharp-Crested Weir

Several researchers suggested empirical equations for determining C_d for sharp-crested weirs. The first equation is from Bazin (1898):

$$C_d = \left(0.405 + \frac{0.00984}{H}\right)\left(1 + 0.55\left(\frac{H}{P+H}\right)^2\right) \tag{2.4}$$

According to Finnemore and Franzini (2002) , Rehbock (1929) provided a second equation:

$$C_d = 0.605 + \frac{1}{305H} + 0.08\frac{H}{P} \qquad (English\ Units) \tag{2.5}$$

$$C_d = 0.605 + \frac{1}{1000H} + 0.08\frac{H}{P} \qquad (Metric\ Units) \tag{2.6}$$

According to Finnemore and Franzini (2002) and Rehbock (1929) , the formulas above are accurate when the ratio $\frac{H}{P} < 1$; and it is valid for $\frac{H}{P} > 1$ if the water surface of the downstream channel is low enough so that back water does not influence the upstream head (Finnemore and Franzini 2002).

Kindsvater and Carter (1959) proposed the following equation:

$$C_d = 0.602 + 0.075\frac{H}{P} \tag{2.7}$$

Kindsvater and Carter suggested that the boundary layer effect on the upstream face of the weir due to viscosity would slightly reduce the length of the crest because of the downward displacement of the nappe. Consequently, they reduced the length of the weir by 1 mm and increased the approach head by 1 mm. This resulted in the following equation for discharge over a suppressed rectangular sharp crested weir:

$$\mathrm{Q} = {}^{2}/_{3}\,\mathrm{C_d}\sqrt{2\mathrm{g}}(\mathrm{L} - 0.001)(\mathrm{H} + 0.001)^{3/2} \qquad (S.I.\,Units) \qquad (2.8)$$

According to Ackers (1978), the Kindsvater and Carter equations are more accurate for $\frac{H}{P} < 2$.

The Institut de Macanique des Fluides de Toulese (I.M.F.T) (Castex, 1969) expressed the head in terms of total head instead of gauged head as shown by:

$$\mathrm{H_1} = \mathrm{H} + \frac{\mathrm{V}^2}{2\mathrm{g}} \qquad (2.10)$$

$$\mathrm{C_d} = 0.627 + 0.018\frac{\mathrm{H_1}}{\mathrm{P}} \qquad (2.11)$$

$$Q = {}^{2}/_{3}\,C_d\sqrt{2g}\,LH_1{}^{3/2} \qquad (2.12)$$

The above equation is more accurate for $\frac{H}{P} < 2.5$. Ackers (1978) presents a graphical comparison of $\mathrm{C_d}$ versus H for various researchers as shown in Figure 2.4 Comparison of equations for a suppressed sharp crested weir (from Ackers, P. 1978).

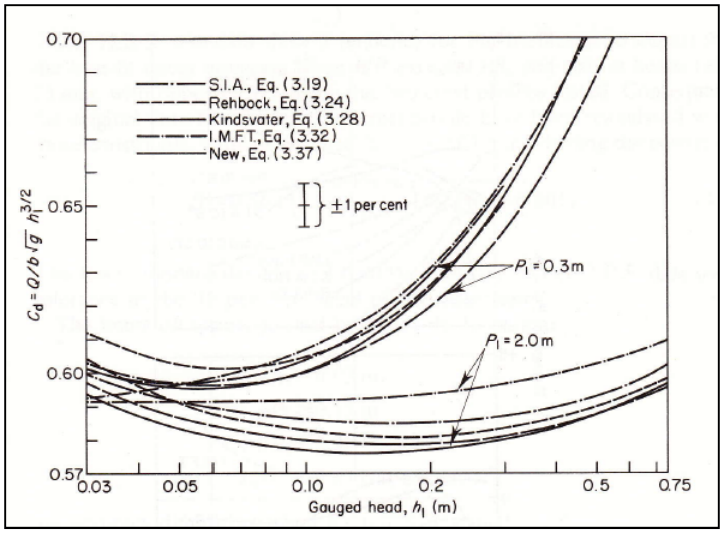

Figure 2.4 Comparison of equations for a suppressed sharp crested weir (from Ackers, P. 1978)

The Bureau of Reclamation (2001) emphasized that some researchers have inaccurately assumed that all correction for the approach velocity can be accounted for by adjusting the approach head alone. However, the Kindsvater equation went further to account for the effect of the approach velocity on the effective crest length and the contraction coefficient in addition to the measured head. For this reason, the Bureau approved the Kindsvater equation as the best for estimating discharge over a suppressed weir. For the best results using any of the above formulas, the following precautions must be taken: the head should be measured at a distance of at least 2.5H upstream of the weir, to avoid error due to drawdown of the water surface level. The nappe must be properly ventilated, a hook gage should be used in a stilling well to measure head, and H must be determined as a mean of several measurements before and after each test. The nappe must also spring free of the weir crest, since a nappe clinging to the weir crest will result in inaccurate measurement.

2.7 Discharge Coefficient of Broad-Crested Weirs

As was mentioned earlier in Section 2.2.2 one major disadvantage of the broad-crested weir is that it has a variable coefficient of discharge. According to Ackers, P. (1978), Singer (1964) explained that the co-efficient of discharge depends on the ratios H/L_w and $H/(H+P)$. The discharge coefficient for a broad-crested rectangular profile weir was suggested, according to Ackers (1978) as:

$$0.461 \text{ (constant)} \begin{cases} 0.08 \leq \frac{H}{L_w} \leq 0.33 \\ 0.18 \leq \frac{H}{(H+P)} \leq 0.36 \end{cases} \tag{2.13}$$

Or

$$0.461\text{- } 0.530 \text{ (variable)} \begin{cases} 0.33 \leq \frac{H}{L_w} \leq 0.85 \\ 0.36 \leq \frac{H}{(H+P)} \leq 0.60 \end{cases} \tag{2.14}$$

Similarly, Hager (1999) developed the following equation for estimating the coefficient of discharge as a function of relative weir length $\frac{H}{L_w}$ given by the equation:

$$C_d = 0.461 \left(\frac{1 + \left(\frac{9}{7}\right)\left(\frac{H_t}{L_w}\right)^4}{1 + \left(\frac{H_t}{L_w}\right)^4} \right) \tag{2.15}$$

For the following conditions:

$$\begin{cases} 0.08 \leq \frac{H}{L_w} \leq 0.85 \\ 0.18 \leq \frac{H}{(H+P)} \leq 0.60 \end{cases}$$

Both Acker's and Hager's equations provide approximately the same value for C_d and both suggest that C_d approaches the same constant (C_d=0.461) for small values of relative weir length. However, unlike Equation 2.13, Equation 2.15 is variable and provides a well-defined value of C_d throughout its entire range of application.

2.8 Weirs with End Contractions

If the weir crest length is less than the width of the channel then the weir is referred to as unsuppressed weir. As shown in Figure 2.5, for unsuppressed weirs, the nappe will have end contractions that cause the effective length of the weir to be less than that of the actual weir crest length.

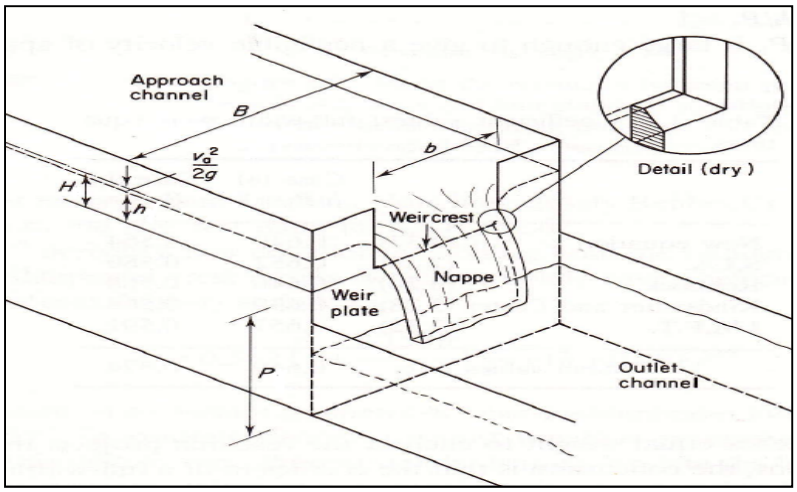

Figure 2.5 Weir with end contractions (Ackers 1978)

According to Ackers (1978), if the sidewall of the upstream channel is far enough from the end contraction so that it does not interfere with the development of the contraction flow, then such a weir is referred to as a fully contracted weir. He reported that by dimensional reasoning, the discharge over a rectangular weir allowing for end contraction is given by the following equation:

$$Q = Q_{fw} - constant \times \sqrt{g} H^{5/2} \tag{2.16}$$

where Q_{fw} is the discharge for the weir if contraction effects are negligible. The last term accounts for the loss of crest length associated with additional contraction of the nappe.

Ackers (1978) went further explaining that Francis defines the equation for a fully contracted weir as follows:

$$Q = {}^{2}/_{3}\, C_d \sqrt{2g}\,(L - 0.1nH)H^{3/2} \tag{2.17}$$

where, n is the number of end contractions,(0 1, or 2). Finnemore and Franzini (2002) reported that the above equation is applicable for the conditions depicted in Figure 2.6, which shows that the crest and end contractions must be at least 2H from the channel boundary, and the length of the crest must be greater than 3H.

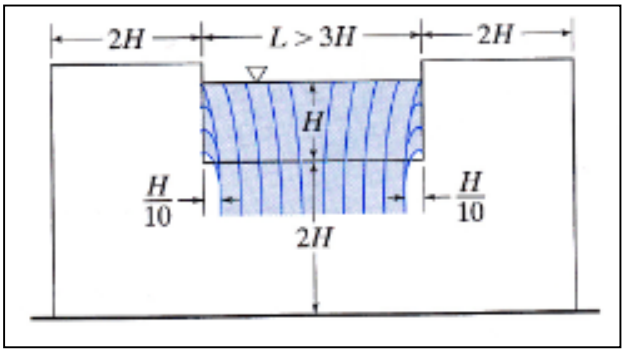

Figure 2.6 Limiting proportions of a fully contracted weir (Finnemore and Franzini, 2002)

Other experimental research has shown that the factor 0.1 is a large allowance for end contraction effects even though it is widely cited (Ackers 1978). Ackers also reports other suggestions of equations for fully contracted weirs. He further reports that if the sidewall of the upstream channel is close enough to the sidewalls of the weir, such that it interferes with the development of the contraction, then such a weir is called a partially contracted weir. Note that the end contraction effects discussed here are not identical to those in the G304 structures. The G304 structures have end wall abutments that jut out into the flow so that flow may not approach the weir parallel to the face of the weir.

2.9 Velocity Profiles of Sharp-Crested Weirs

Rajaratnam and Muralidhar (1971) investigated the pressure and velocity distribution in the region of a suppressed sharp-crested weir for a range of H/P values. They conducted 10 experiments with H/P ranging from 0.191 to 8.57. In these experiments the pressure and velocity were measured at the weir face and at section O-O as shown in Figure 2.7.

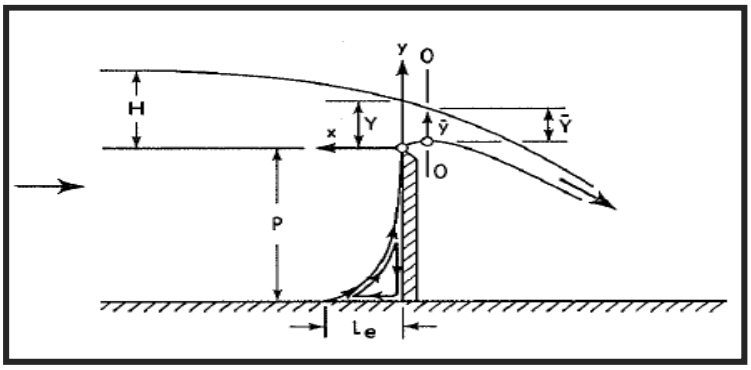

Figure 2.7 Definition sketch showing section of pressure and velocity measurement (Rajaratnam and Muralidhar 1971)

Table 2.1 and Figure 2.8 present the experimental results and velocity distributions, respectively, for the experiments conducted by Rajaratnam and Muralidhar (1971).

Table 2.1 Experimental data associated with a sharp-crested weir (Rajaratnam and Muralidhar, 1971)

Expt. No. *No. d'Essai*	*P* (ft/*pied*)	*H* (ft/*pied*)	*H/P*	*q* (cfs/ft/*pied*²/s)	L_e (in/″)
A1	0.974	0.608	0.625	1.815	1.75
A2	0.974	0.678	0.697	2.154	1.88
A3	0.974	0.335	0.344	0.711	1.63
A4	0.974	0.186	0.191	0.340	1.37
B1	0.580	0.650	1.122	2.098	2.13
C1	0.094	0.177	1.882	0.320	0.38
C2	0.094	0.180	1.915	0.350	–
C3	0.094	0.323	3.440	0.988	–
C4	0.094	0.444	4.730	1.720	–
D1	0.056	0.480	8.570	1.713	–

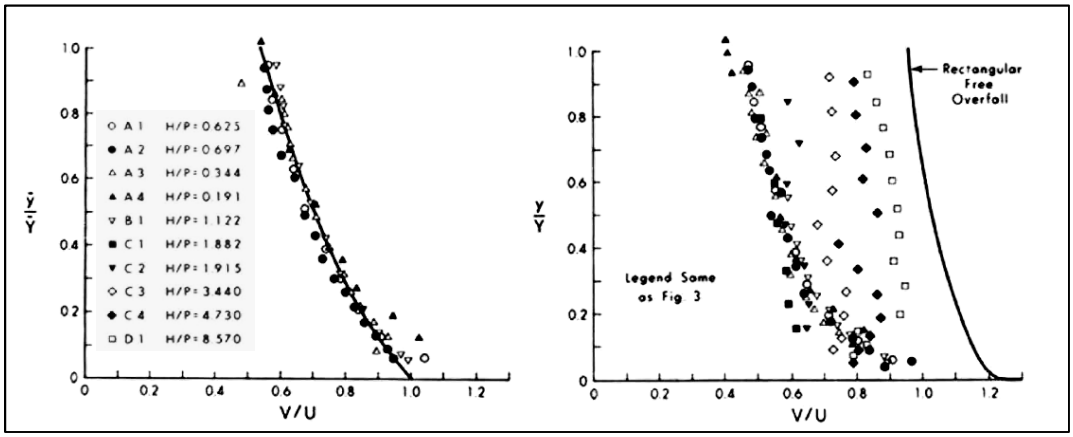

Figure 2.8 Velocity distributions at (a) section O-O, (b) at the crest (Rajaratnam and Muralidhar, 1971)

According to Rajaratnam and Muralidhar (1971), V is the velocity magnitude at each point in the profile, whereas U is the reference velocity equal to $\sqrt{2gH}$. They went further to explain that for Figure 2.8(a)and for values of H/P ranging from 0.191 to 1.122, the data falls on a single curve and V/U decreases from unity at y/Y=0 to 0.54 at y/Y=1.0. Figure 2.8 shows that for flow over a sharp-crested weir the maximum longitudinal velocity is near the weir crest and it decreases towards the water surface. In Figure 2.8(b), and for values of H/P ranging from 0.191 to 1.915, the distribution was represented by a single curve and the data points asymptotically approach the free over

fall curve for higher values of H/P. Furthermore, they studied the velocity field upstream of the weir for the first two series of tests and found out that for x/H ≥0.6 the weir did not significantly affect the velocity, whereas for smaller x/H the upper layer velocity increases significantly. They went further to explain that for larger values of Reynolds number the effect of viscosity could be neglected. In addition, the ratio of the length of the standing eddy on the upstream side of the weir L_e (see Figure 2.) to the height of the weir above the approach channel P (i.e L_e/P) is primarily a function of only H/P. They showed that L_e/P increases monotonically with H/P (Rajaratnam and Muralidhar, 1971).

2.10 Velocity Profiles of Broad-Crested Weirs

Hager and Schwalt (1994) studied broad-crested weirs, and in their work they used a miniature propeller meter to measure the stream wise velocity components at a height of 10mm and at selected sections. Fourteen (14) tests were conducted at low Froude numbers but for turbulent conditions. The condition $0.1 < \frac{H_t}{L_w} \leq 0.4$ was satisfied for all of the tests. Figure 2.9, and Figure 2.10 show the measured free surface profiles and lateral velocity distributions, respectively. In these figures, h represents the flow depth with respect to the weir crest, and H_o represents the approach head with respect to the weir crest.

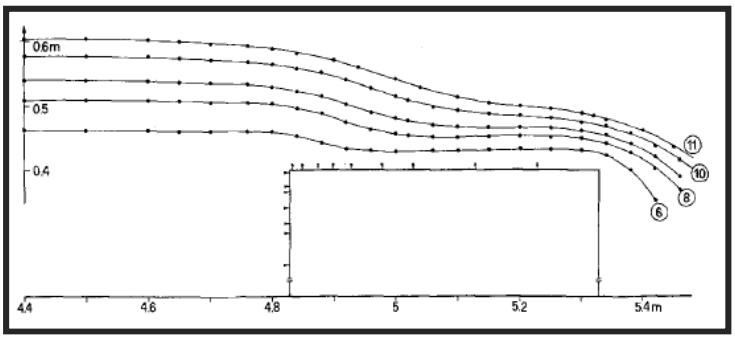

Figure 2.9 Free surface velocity profiles (Hager and Schwalt, 1994)

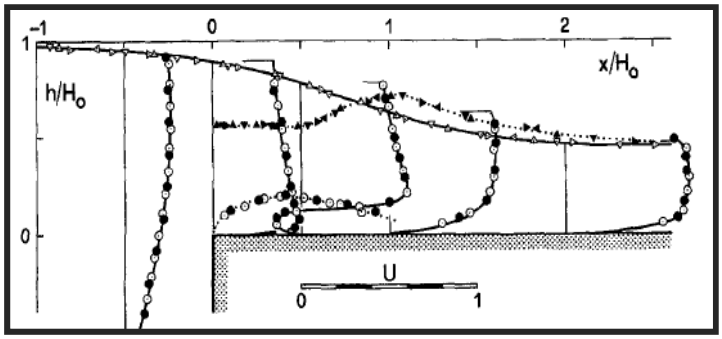

Figure 2.10 Lateral velocity profiles upstream and at selected sections over the weir crest (Hager and Schwalt, 1994)

According to Hager and Schwalt (1994), the maximum velocity in a vertical velocity profile at a distance upstream of the weir of $x/H_o = -0.5$ occurs very close to the water surface. Because of the curvature of the streamlines, the maximum velocity does not occur at the water surface for velocity profiles that are above the weir crest, especially at the leading edge of the crest. Consequently at the upstream edge of the weir crest ($x/H_o = 0$) the velocity increases from the water surface downwards to the top of a small boundary layer. Within the boundary layer, the velocity decreases to zero at the crest surface. At $x/H_o = 0.5$ the velocity profile is similar to the profile at $x/H_o = 0$, except that immediately adjacent to the crest there is a small separation zone in which the velocity direction is reversed. At $x/H_o = 1$ and $x/H_o = 2$ the vertical location of the maximum velocity again approaches the water surface; for the latter distribution, the streamlines are nearly parallel and the velocity distribution is once again similar to a uniform velocity distribution.

Gonzalez and Chanson (2007) and Felder and Chanson (2012) did similar work on an upstream rounded edge broad-crested weir. The stream-wise velocity distributions at selected sections above the crest are shown in Figure 2.11.

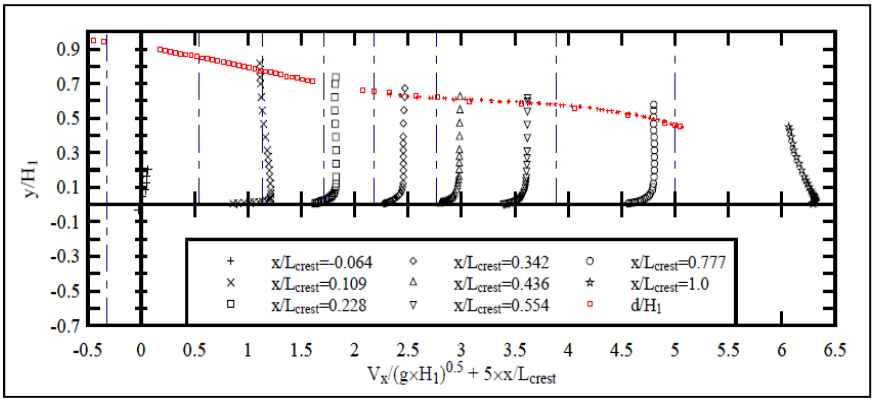

Figure 2.11 Velocity distributions along a broad-crested weir (Felder and Chanson, 2012)

The results are analogous to those of Hager and Schwalt (1994). As shown in Figure 2.11, the velocity very close to the upstream weir edge increases from the surface to the bed except within the small boundary layer near the bed. In addition, the maximum velocity in the downstream-most velocity distributions shifts towards the surface and a uniform velocity distribution develops at the sections farthest downstream of the leading edge of the weir crest.

2.11 Side Weirs

Side weirs are extensively used in hydraulic engineering for purposes of flow control and diversion in irrigation, urban sewer systems, land drainage and sanitary engineering. A side weir is a weir built as part of a channel embankment with its crest parallel to the flow direction in the channel. The weir situated in the prototype G304 is similar to a side weir in that the flow in the channel that supplies the G304 is parallel to the crest of the weir. Therefore, understanding the concept and hydraulic behavior of side weirs is relevant to this research. Figure 2.12 shows the profile and plan of a typical side weir.

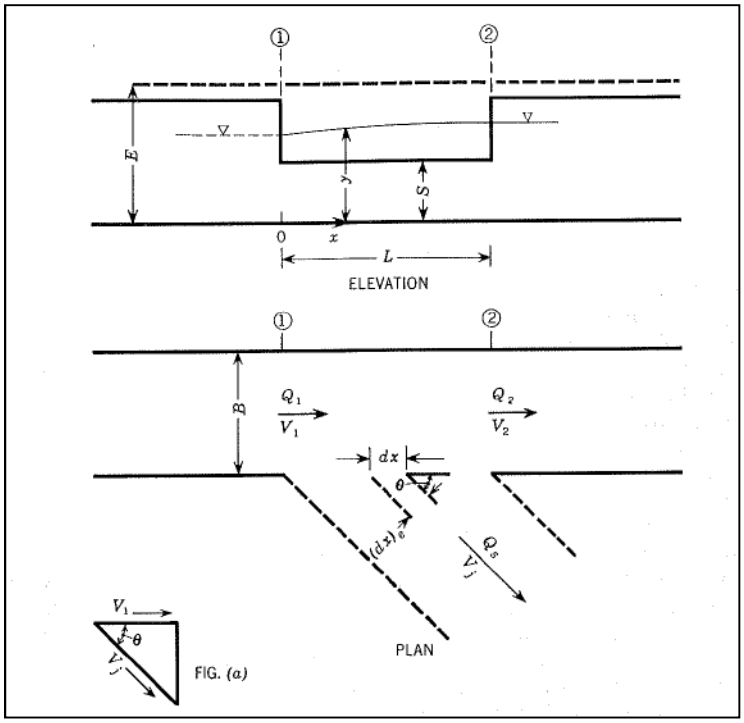

Figure 2.12 Definition diagram of side weir, (Subramanya and Awasthy 1972)

Side weirs can be designed with various geometric shapes just like normal weirs, but only rectangular sharp-crested side weirs are relevant for the present research.

Many researchers have investigated flow over a rectangular sharp-crested side weir using different experimental techniques with the primary aim of estimating the discharge coefficient. There are three common flow conditions in the channel in the vicinity of the side weir. These include; subcritical, supercritical and hydraulic jump as illustrated in Figure 2.13. When the flow depth at the upstream end of the side weir is greater than the critical depth, the water level at the downstream end becomes subcritical, resulting in a decrease in weir flow along the length of the weir (Figure 2.13a). Alternatively, if the depth just upstream of the weir goes through critical, then the flow downstream becomes supercritical as shown in Figure 2.13b. Finally, if the upstream

depth is critical and the downstream depth is subcritical a hydraulic jump occurs somewhere along the length of the weir crest as in Figure 2.13c.

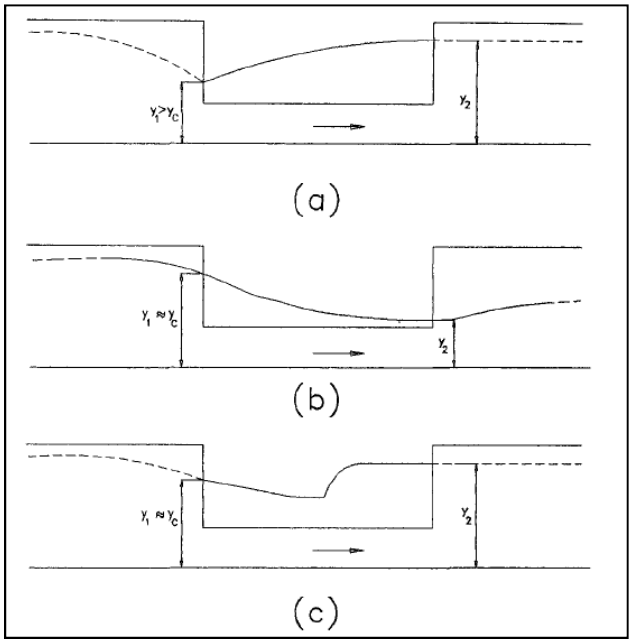

Figure 2.13 Types of flow regime for side weirs: (a) subcritical flow; (b) supercritical; (c) hydraulic jump (Borghei et al. 1999)

The subcritical flow condition is the most common as in the case of the prototype. The main purpose in the design of side weirs is to divert a fraction of the main channel flow; therefore, accurate estimation of the discharge coefficient is very important (Bagheri and Heidarpour 2011). Several researchers have done experiments to investigate the discharge co-efficient of a rectangular side weir in subcritical flow (Hager and Schwalt 1994; Subramanya and Awasthy 1972; Borghei et al. 1999; Ranga Raju et al. 1979; Hager 1978; Singh et al. 1994). Muslu (2001) used energy principles to develop a numerical analysis model to estimate flow over side weirs. Ramamurthy et al. (2006) used empirical equations based on the Partial Least Squares method to define a modified discharge co-efficient of a rectangular side weir. Many other researchers have

approached this subject from different points of view but a commonly accepted equation still does not exist (Borghei et al. 1999).

The discharge per unit length of a side weir (q) can be derived from De Marchi's equation and it is given as:

$$q = \frac{dQ}{dx} = \frac{2}{3} C_M \sqrt{2g(y - P)^{3/2}} \tag{2.18}$$

where C_M is the De Marchi's discharge coefficient, y is the depth of flow in the channel and P is the weir height. The discharge coefficient is dependent on the geometric characteristics of the side weir as well as the Froude number of the flow in the channel and the flow depth of the channel at the starting point of the weir. Based on dimensional analysis, the discharge coefficient can be expressed as:

$$C_M = f\left(F, \quad \frac{L}{B}, \quad \frac{y_1}{L}, \quad \frac{P}{y_1}\right) \tag{2.19}$$

where F is the Froude number of the main channel and the other parameters are related to the geometry of the flow (see Table 2.2).

Table 2.2 Side weir discharge co-efficient presented by various researchers

No.	***Discharge coefficients for rectangular side weirs***	***Source***
1	$C_M = 0.864\left(\frac{1 - F_1^2}{2 + F_1^2}\right)^{0.5}$	Subramanya and Awasthy, 1972
2	$C_M = 0.81 - 0.6F_1$	Ranga Raju et al., 1979
3	$C_M = 0.864\left(\frac{1 - F_1^2}{2 + F_1^2}\right)^{0.5}$	Hager, 1978
4	$C_M = 0.33 - 0.18F_1 + 0.49\left(\frac{w}{y_1}\right)$	Singh et al., 1994
5	$C_M = 0.71 - 0.41F_1 - 0.221\left(\frac{w}{y_1}\right)$	Borghei et al., 1999

Some researchers agree that the approach Froude number is the only parameter that significantly affects the weir flow discharge coefficient, (Subramanya and Awasthy 1972; Ranga Raju et al. 1979; Hager 1978). However, other researchers (Borghei et al. 1999; Singh et al. 1994) include an additional parameter of $\frac{w}{y_1}$ (where y_1 is the flow depth upstream of the side weir and w is the height of weir). Borghei et al. (1999) and Singh et al. (1994) do not agree on the extent of influence of this additional parameter. Singh et al. (1994) argues that $\frac{w}{y_1}$ will have a greater influence on the discharge whereas, Borghei et al. (1999) argue otherwise. However, both believe that as $\frac{w}{y_1}$ increases (that is with increase in water depth upstream) the overflow discharge will decrease. They therefore suggest that $\frac{w}{y_1}$ be given a negative sign. Ramamurthy et al. (2006) suggest a much more complex exponential equation for the discharge coefficient given as:

$$\begin{aligned} C_M = & \left[1.0 + 0.33\left(\frac{L}{B}\right) - 0.105\left(\frac{L}{B}\right)^2\right] \\ & * \left[1.0 + 0.034\left(\frac{w}{y_1}\right) - 0.491\left(\frac{s}{y_1}\right)^3 + 0.421\left(\frac{s}{y_1}\right)^4\right] \\ & * \left[[0.348 + 0.022(F_1) - 0.203(F_1)^2 + 0.303(F_1)^3 \right. \\ & \left. - 0.168(F_1)^4]\right] \end{aligned} \tag{2.20}$$

Admiraal, (2007), in a literature review prepared for the SFWMD, mentions that this equation proposed by (Ramamurthy et al. 2006) does not capture the physics behind the coefficient. He further explains that, even though the G304 structure has some similarities to a side weir, the following dissimilarities exist: (1) side weir studies are commonly conducted using sharp-crested weirs (though not always); (2) the extent of the width of the G304 canal compared to the weir length is quite large; (3) the G304 outlet

structure is built into the canal instead of into the canal boundary wall, and (4) treatment of the flow as one-dimensional is questionable. Considering these differences, the complex layout of the structure, and the flow over the weir, the equations developed for side weirs may offer insight about the behavior of the G304 structures but are not practical for accurately predicting discharge.

Bagheri and Heidarpour, (2011) studied the distribution of three-dimensional velocity over the crest and in the vicinity of a sharp-crested rectangular side weir using an acoustic Doppler velocimeter (ADV). The experimental layout of the weir structure used by Bagheri and Heidarpour is given in Figure 2.14 while the modeling characteristics and test conditions are given in Table 2.3.

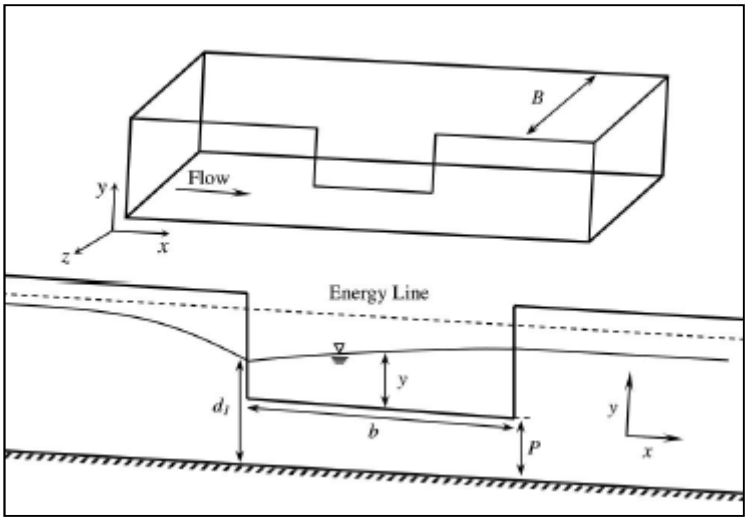

Figure 2.14 Definition sketch of side weir (Bagheri and Heidarpour, 2011)

Table 2.3 Summary of model characteristics and testing conditions (Bagheri and Heidarpour, 2011)

Weir width (cm)	Weir height (cm)	F_1	P/d_1	b/B	Q_S (l/s)
20	5, 10, 15	0.08–0.61	0.22–0.83	0.50	2.1–29.2
30	5, 10, 15	0.10–0.72	0.28–0.91	0.75	2.8–29.5
40	5, 10, 15	0.14–0.88	0.33–0.87	1.00	2.6–26.8

According to Bagheri and Heidarpour (2011) the results of their work indicate that at large distances upstream and downstream of the weir the values of V_y and V_z were small. As a result, the flow was approximately horizontal. However, V_x is maximum close to the start of the weir and minimum near the end of the weir as shown in Figure 2.15 and Figure 2.16.

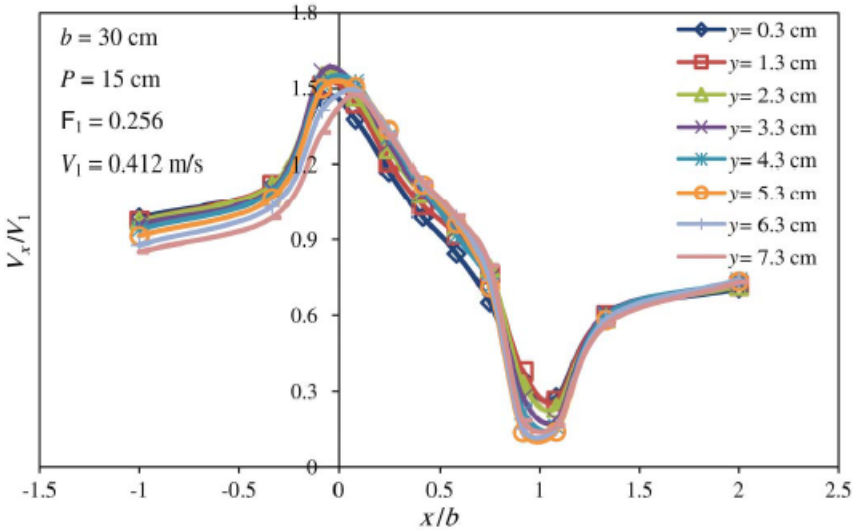

Figure 2.15 Distribution of longitudinal velocity (V_x) alongside weir (Bagheri and Heidarpour, 2011)

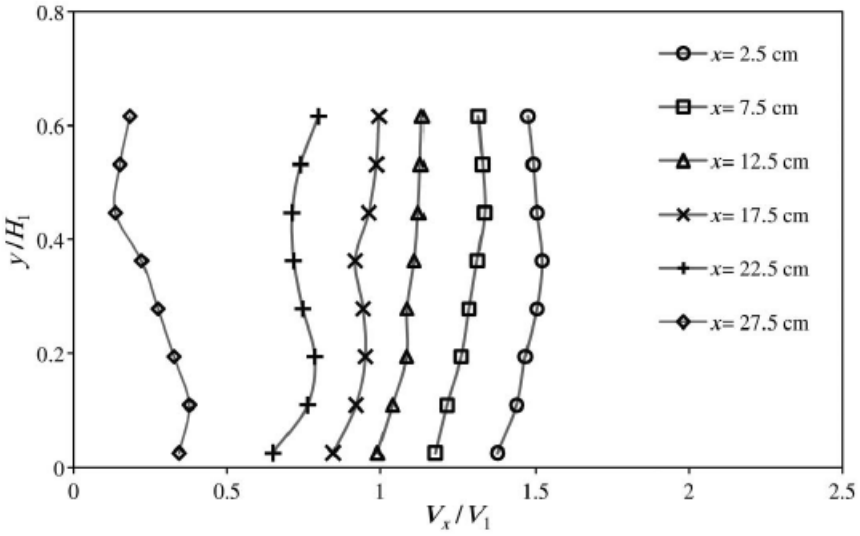

Figure 2.16 Longitudinal velocity (Vx) profiles (Bagheri and Heidarpour, 2011)

The values of V_y demonstrated an upward flow at the elevation of the weir crest. At higher elevations above the weir, V_y gradually decreased until the flow at the surface became downwards (see Figure 2.17 and Figure 2.18).

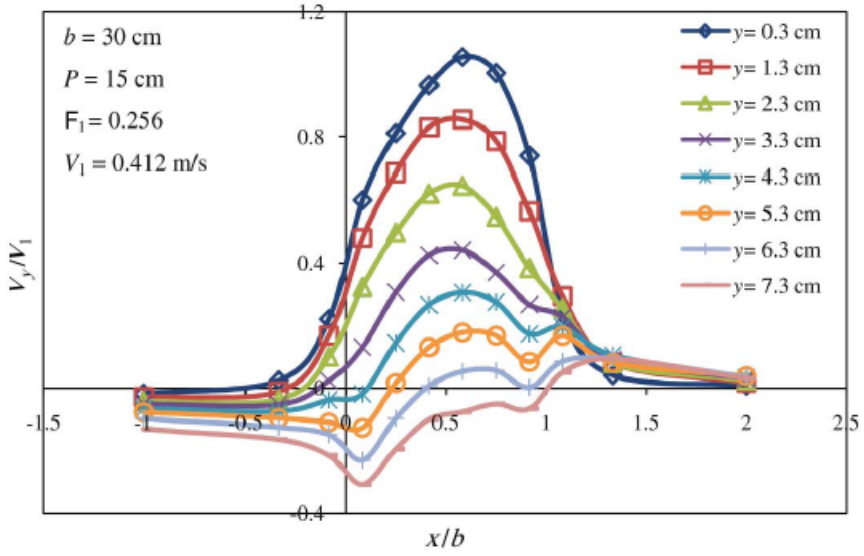

Figure 2.17 Distribution of vertical velocity (Vy) alongside weir (Bagheri and Heidarpour, 2011)

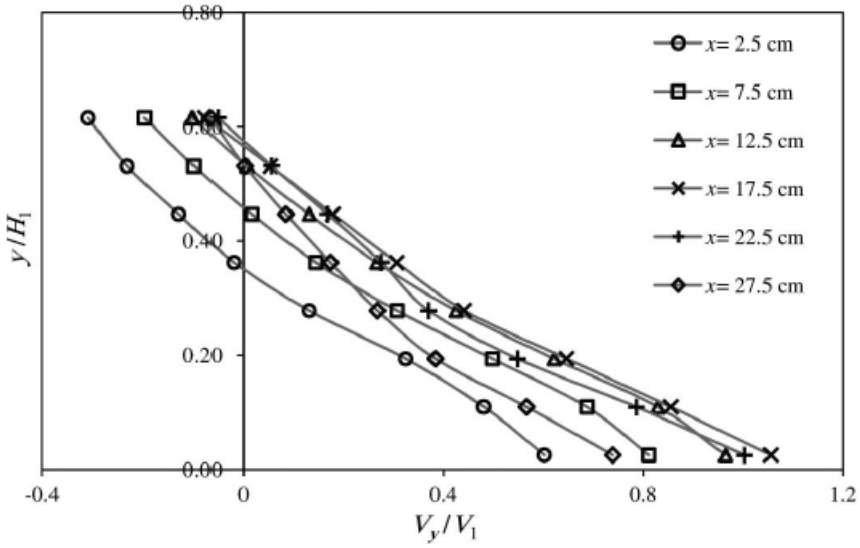

Figure 2.18 Vertical velocity (Vy) profiles (Bagheri and Heidarpour, 2011)

On the other hand, the values of V_z implied an increase in velocity of the over flow along the crest of the side weir from the beginning to the end of the weir (see Figure 2.19 and Figure 2.20).

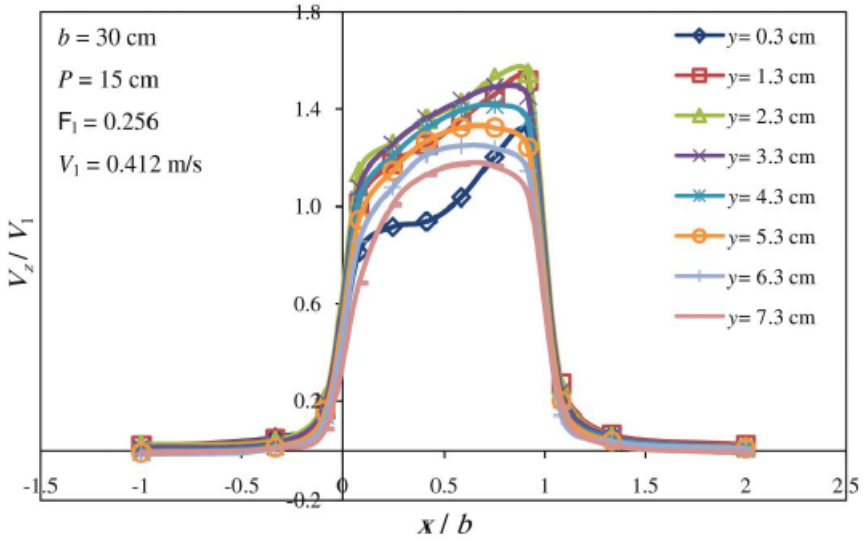

Figure 2.19 Distribution of lateral velocity (Vz) alongside weir (Bagheri and Heidarpour, 2011)

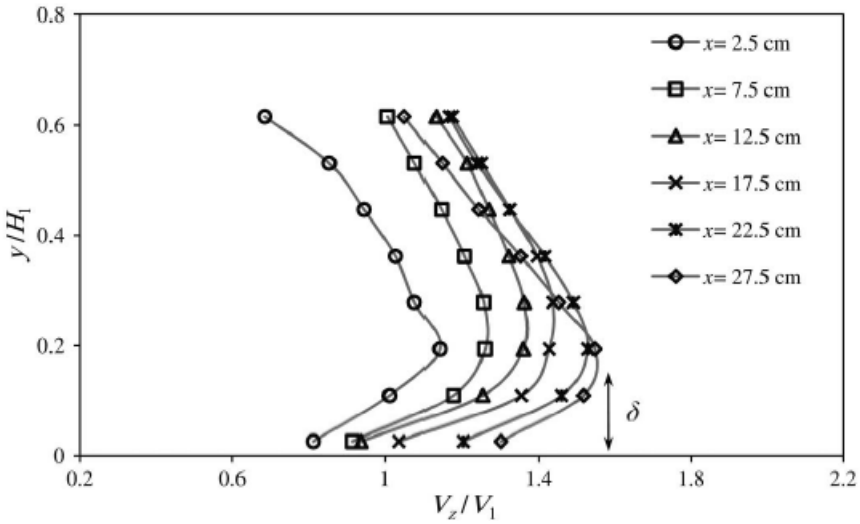

Figure 2.20 Lateral velocity (V_z) profiles (Bagheri and Heidarpour, 2011)

They explained that the lateral velocity V_z increases with increasing elevation above the weir crest up to the maximum value of V_z which occurs at a depth of δ above the weir crest as indicated in Figure 2.20. This region is called the boundary layer, and the

maximum value of δ occurs near the center of the weir. The average thickness of the boundary layer is $0.27H_t$. In addition to studying the three-dimensional velocity over a rectangular sharp crested side weir, Bagheri and Heidarpour (2011) used the velocity profiles to estimate the variation of local discharge along the crest of the side weirs for different Froude number flows, and the result is shown in Figure 2.21, where Q_{si} is the local discharge passing through a 5.0 cm elementary strip. This figure shows that Q_{si} increases along the weir crest, Bagheri and Heidarpour (2011) presented the following explanation for this observation;

1. V_z increases as flow nears the end of the side weir thereby increasing the outflow transmission.
2. V_x decreases near the end of the side weir. As a result, the flow energy along the main channel direction decreases, thereby increasing outflow transmission.
3. Towards the end of the side weir, the local angle of the spilling jet with the normal to the plane of the weir decreases. As a result, the weir behaves similar to a normal weir, allowing more flow to pass through it.

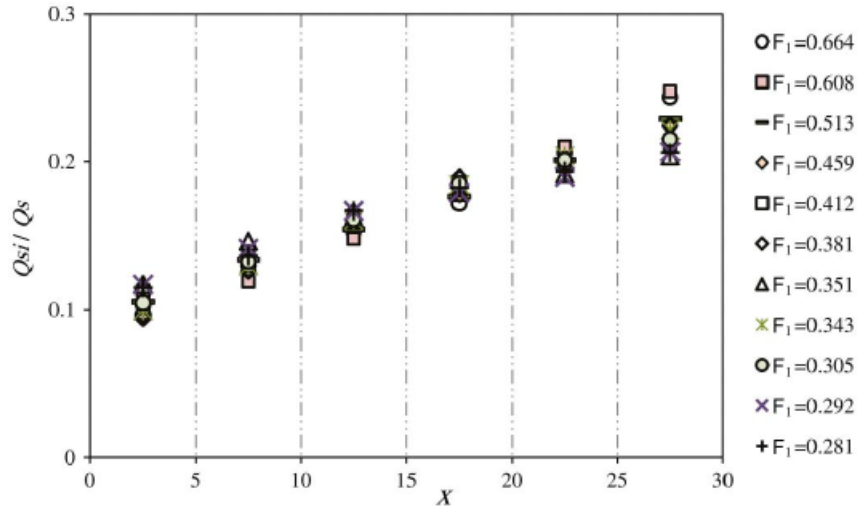

Figure 2.21 Variation of dimensionless local discharge along the crest of side weir (Bagheri and Heidarpour, 2011)

They went on further to explain that the above three reasons indicate that a zone of stagnation occurs close to the end of the weir, thus making it easier for water to flow over the weir.

2.12 Particle Tracking Velocimetry

2.12.1 History

Image velocimetry is an optical method to quantify the velocity field in fluid flows. The concept of image velocimetry dates back to the 13th century when Leonardo Da Vinci sketched flow field patterns formed by differing objects in a stream flow. According to Adrian (2005), the simplest form of image velocimetry could be the first time a person watched floating debris or algae in a stream flow with the notion of velocity. He mentioned that:

"*It is almost inconceivable that a great intellect like Isaac Newton would not have observed the moving patterns and seen the potential for*

visualizing and even measuring the surface velocity from the displacements of the particles of algae".

However, although much research has been conducted in this area, it was not until 1981 that the concept of Particle Image Velocimetry (PIV) was first clearly defined and used. Since then Particle Image Velocimetry has attracted many researchers (Adrian 1981). The advent of modern day lasers, high-speed cameras and computers has made great improvements to PIV and PTV techniques possible.

2.12.2 Image Velocimetry

Velocimetry is the measurement of fluid velocity. There are two main velocimetry techniques: Particle Image Velocimetry (PIV) and Particle Tracking Velocimetry (PTV). PIV measures Eulerian velocities and PTV measures Lagrangian velocities. Image velocimetry is a non-intrusive optical technique used to measure instantaneous whole flow field velocity by measuring the displacement of seeded tracer particles over a known period of time. It is assumed that the particles truly flow with the local fluid velocity. It has the advantage of being capable of measuring complex flow fields and is very useful in the study of turbulence and multiphase flows (Liu and Tao 2007).

Acoustic Doppler Velocimetry (ADV) and Laser Doppler Anemometry (LDA) are additional tools that have been widely used to measure flow fields. The ADV and LDA are fundamentally single point velocity measurement instruments. Both of these instruments are suitable for laboratory measurements. However, while there are more robust versions of ADVs that are suitable for field measurements, Sokoray-Varga and Jorza (2008) and Lloyd (1995) mentioned that both ADVs and LDAs can only provide flow field data by performing phase-averaging operations. Image velocimetry techniques

provide velocity measurement for a whole field simultaneously and at better spatial and temporal resolutions than ADV and LDA.

For Image Velocimetry, the particles are recorded by a digital video camera or photographic film as they follow the flow patterns across an area of interest. Image velocimetry can provide two- and three-dimensional flow velocity measurements if a single or multiple cameras is/are used, respectively. It is sometimes necessary to illuminate the tracer particles for better temporal resolution, and the recordings are then separated into image frames using an appropriate frame grabber. The resulting images are analyzed to measure particle displacements and the method used to analyze displacements is often selected based on the tracer density. If the tracer particle density is low, the displacement of individual particles between successive frames can be directly measured, and the velocity is calculated by dividing the particle displacement by the time difference between the two successive frames. This process is referred to as PTV or Low Density PIV. For high-densities of tracer particles, it is difficult to measure individual particle displacements. Instead, the movement of small groups of particles or flow forming patterns is calculated; this process is referred to as PIV. PIV calculates an average (not a mean, but a representative value) velocity for the particles within a user defined sub-region of the imaged region, the sub-region is called an interrogation window or area. The quality or accuracy of the result is dependent on the size of the interrogation window relative to the displacements of particles between successive images. If the interrogation window is small and displacements are large, many particles that are within the interrogation window for the first image will not be in the interrogation window in the second image, leading to incorrect displacement estimates. On the other hand, if the

displacements within the interrogation window are small between successive images, velocity estimates will have large uncertainties. In addition, PIV is based on the assumption that the displacements of tracers within the interrogation window are relatively uniform, and large displacement gradients can result in a velocity estimate that is not representative of all of the velocities within the interrogation area. These problems can be resolved by adjusting the interrogation window size, the tracer particle density, and the temporal resolution of successive images. In general, PTV can provide higher spatial resolutions than PIV since the particle scale is smaller than the interrogation window scale.

One important factor in image velocimetry is the choice of tracer particles for the following reasons: (1) when the density of the fluid and the tracers do not match, gravity influences the accuracy of velocity measurement, (2) the tracer size and shape can influence how the tracer is influenced by the flow field, (3) turbulence is random and occurs at high Reynolds numbers, and tracer particles must be small enough to follow the actual flow, and (4) the light scattering ability of a tracer determines its detection during processing. Cowen and Monismith (1997) investigated the effect of particle size on error by generating images with average seeding densities of 12 particles per 32x32 pixel sub-window. By applying a linear displacement gradient of 3% (0.03pixel/pixel) they found that the minimum error was reached at particle sizes closer to 3.0 pixels. As a result they suggested that the optimum particle size for minimum error was between 2.0 and 4.0 pixels. However they went on further to explain that for a more robust correlation algorithm it is better to use larger sized particles.

2.12.3 Particle Image Velocimetry

A simple criterion used to differentiate PIV from PTV is the source density (image density); this is defined as the mean number of particles in a resolution volume denoted as N_I. Adrian (1981)defined the source density by the following mathematical equation;

$$N_I = C\Delta z_o \pi {d_i^2}/{4M^2} \tag{2.21}$$

where C is the mean number of particles per unit volume; d_i is the image distance; z_o is the distance away from object plane; M is the magnification and is defined as

$$M(z) = \frac{d_i}{d_o - d_i} \tag{2.22}$$

and d_o is the object distance. In addition, $\Delta z_o \pi {d_i^2}/{4M^2}$ is the volume of the interrogation window. If $N_I << 1$, the probability of the existence of more than one particle in an interrogation cell is smaller than the probability of finding one particle in a cell; this corresponds to the low image density limit and in this case, PTV methods are preferred. If $N_I >> 1$, it is always likely that there will be many particles in the interrogation window; this corresponds to high image density limit and PIV methods are preferred.

As stated previously, in PIV, the image is divided into sub-sections called interrogation windows, and all of the particles in each interrogation window are assumed to move as a unit between two image frames. The displacement of the interrogation windows between the first and the corresponding window in the second frame is determined. Sokoray-Varga and Jorza (2008) explain that this means that PIV provides only one vector per interrogation window, which makes processing and filtering much

easier. Additionally, for better neighborhood-correlation, the number of tracer particles must be sufficient and they must be homogenously distributed. Finally, particle displacements must be smaller than the interrogation window for correct correlation.

2.12.4 Particle Tracking Velocimetry

In contrast with PIV, PTV recognizes each individual particle separately in the first frame and locates a corresponding match in the second frame. Then it locates the centroids of each particle in both frames and calculates the displacement of the centroids of each individual particle from the first to the second image frame using the neighborhood information. Therefore, PTV provides a vector for each tracer particle. According to Sokoray-Varga, vectors obtained by PTV are irregularly placed making it difficult to remove erroneous vectors. For PTV, the particles need not be homogeneously distributed.

The rudimentary form of PTV calculation is based on one of two techniques: (1) the cross correlation technique using two image frames, or (2) the nearest neighbor technique using two or more consecutive image frames. The nearest neighbor algorithm was used in this research. Recent PTV approaches include techniques such as: relaxation methods that analyze the probability of matching particles, and variational approaches which function not by estimating individual displacement vectors but by estimating functional distributions of multiple vectors. Adrian (1981), presented the basic principles of PTV. He explained that when applying PTV the following implication must be considered. The number of particle images per unit volume is small and therefore it is easier to computationally process each individual image separately. With low image density, the probability of particle images overlapping in the same interrogation window

is low. The probability of finding one particle in the interrogation volume is $N_I e^{-N_I} \sim N_I$. Finally, the velocity measurement and the particles are randomly located and the mean spacing between nearest neighbor particles is equal to $0.55C^{-1/3}$. The images are processed to improve the signal-to-noise ratio (SNR) with respect to the image background and to locate individual particles.

The particles are differentiated from background noise by amplifying the pixel brightness of the particles to full-scale value. By setting the threshold level appropriately, the edges of individual particles can be located using maximum grey level gradient criterion. Then by setting the pixels whose grey level exceeds a defined threshold to one and setting the remainder to zero, noisy pixels are filtered. The next step is to locate the centroids of each particle in the reference window and to match each particle of the first image to one in the second image (Adrian 1981).

Nearest neighbor is a common algorithm used for image matching; it was the algorithm used in the current research. It identifies the centroids of all tracer particles in two image frames and matches the particles in the second frame to particles in the first frame one particle at a time. Adrian (1981) mentioned that the probability that the correct match of a particle has been found in the second image is equal to the probability that the particle remains in the interrogation frame at the time of the second exposure $F_o(w\Delta t)$ multiplied by the probability of not finding any other possible match within an interrogation cylinder of height $\Delta z_o$and radius $\sqrt{u^2 + v^2}\,\Delta t$ at time t and time t+Δt. He went further to say that assuming a Poisson distribution that probability is given by:

$$Pr(cm) = F_o(w\Delta t)\exp\left[-(2 - 0.53F_o)C\Delta z_o \pi(u^2 + v^2)\Delta t^2\right. \qquad (2.23)$$

where *Pr(cm)* is the probability that a correct match has been found for a particle. This equation is averaged over the entire flow field and the rate of detection per unit area is the number of image particles per particles per unit area times the probability calculated using Equation 2.18 above.

The basis of the matching is that the particle displacement cannot exceed the dimensions of the interrogation region (when well seeded), and that no other particle is within the vicinity of the matched particle. The method also requires that the change in particle velocity be small between two image frames. Once all of the particles have been matched, the PTV algorithm then estimates the displacement of the centroids of each matching pair. The velocity is then calculated by dividing the displacement by the time between successive images. However, it must be noted that particle matching is not always successful especially with increased particle density. It is possible that a particle in the first image frame will move out of the interrogation frame in the second image or due to non-uniform lighting will be below the threshold detection level in the second image and will not be visible (Ruhnau et al. 2005). Incorrect particle matching will result in erroneous velocity vectors as illustrated in Figure 2.22.

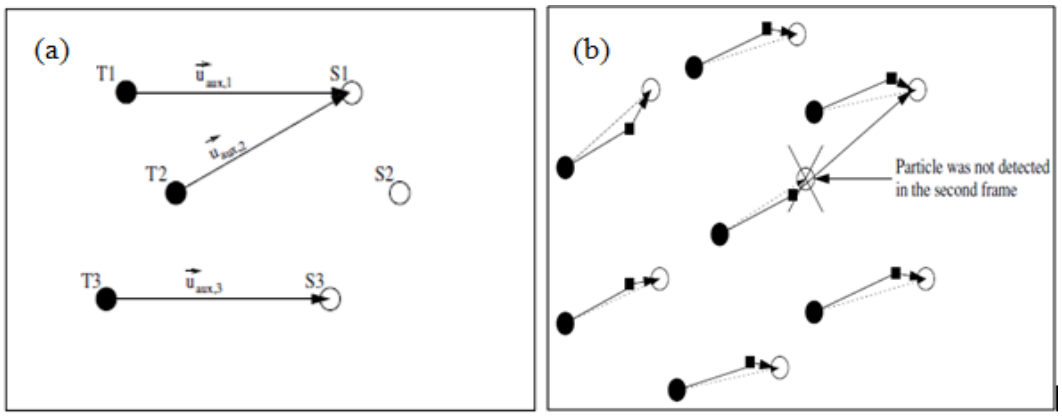

Figure 2.22 (a) Shows a simple nearest neighbor mismatch. (b) Shows a particle that has not been detected in the second frame. Full and open circles represent particles in the first and second frames respectively, whereas the full rectangles denote the current estimate (Ruhnau et al., 2005)

These problems can be curtailed by selecting appropriate image filter thresholds and by carefully selecting image exposure times. Another source of erroneous vectors is the discrepancy between flow velocity and particle velocity, which is influenced by external sources such as gravitational forces, viscosity, fluid inertia, pressure gradients and Brownian motion. The PIV/PTV software used in this research was custom made, it contains a wide range of image and velocity filtering tools to help identify and eliminate erroneous vectors.

Many researchers in both laboratory and large-scale field studies have used PTV in their studies for tracking the motion of large floating particles. Such particles are typically much larger than tracers used for traditional PIV and PTV. This form of PTV, known as Large-scale PTV (or LPTV) can provide a good estimate of mean surface velocities and large-scale turbulence motions, but is unable to capture higher frequency turbulence motions. Sokoray-Varga and Jorza (2008) and Lloyd (1995) used LPTV to study surface velocities in an unsteady velocity field; Sokoray-Varga and Jorza (2008) used it to measure surface velocity distributions to characterize large vortices and

turbulence in laboratory scale models, and Jesuthasan et al. (2006), used it for measurement of granular flow in laboratory scale models. Meselhe et al.(1999), on the other hand used PTV to measure low flow discharges in a real stream.

2.12.5 Effects of Wind-Induced Water Currents on Surface Velocity

Wind actions acting on water surfaces cause drift and countercurrents depending on the direction of the wind. Wind is the main source of energy causing turbulent mixing in lakes and other open water bodies. Wind may have a two-fold effect on the field experiments done at the G304 test site. First, local winds affect the surface velocity of the water and thus the velocity profile in the water column. Since LPTV measurements are only made at the water surface, variations of the velocity profile from theoretical profiles will have a significant impact on the accuracy of discharge calculations. Second, average winds may cause setup of the water surface in the channel. Wind setup may vary from location to location and the effective head at the inlet to the G304 structure may vary somewhat from the head measured at the canal gage. According to Tsanis (1989), laboratory experiments and numerical models showed that wind acting on water surfaces can cause drift currents in the direction of the wind and a bottom countercurrent. The wind induced drift at the surface and the resulting countercurrent in an open water body is depicted in Figure 2.23.

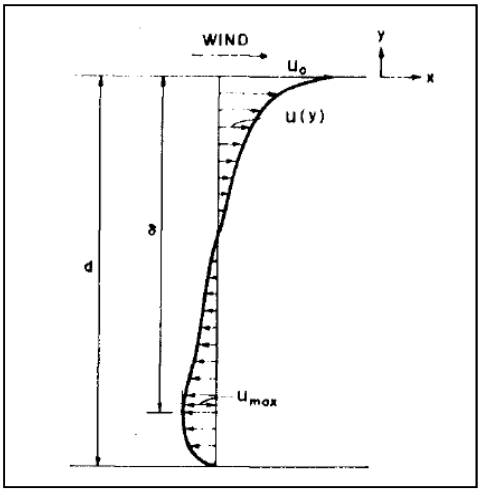

Figure 2.23 Effect of wind-induced current on water surfaces (Tang el al.1978)

Associated with the induced velocity shown in Figure 2.23, there is a windward lowering of the water level and a leeward rise called wind setup. Tsanis (1989) describes that at low wind velocities the viscous drag and the form drag of the capillary waves maintains the wind stress, however the wind drives the surface current directly or by micro-breaking. Alternatively, at high wind speeds the gravity waves are broken down resulting in considerable energy dissipation, which will consequently result in the mixing of water surfaces. Several researchers used laboratory studies to measure the surface drift velocity u_{sw}. Baines and Knapp (1965), Keulegan (1951), Masch (1963), Wu (1975), Tsuruya et al. (1985) and others (mentioned by Tsanis (1989)) measured drift velocities as a fraction of mean air speed. Their results varied from 0.033 reported by Kuelegan (1951), to 0.032 and 0.038 reported by Lin and Gad-el Hak (1984) respectively. Tang et al (1978) provided a table (Table 2.4) of drift velocities associated with wind driven currents.

Table 2.4 Ratio of drift velocities to mean speed velocities reported by several researchers (Tang et al 1978)

Author	Method	u_o/U_o (%)
Keulegan	Paraffin particle	3.3
Tickner	Dye	3.0
Plate et. al.*	Paper disc	2.60
Shemdin *	Paper disc	2.89
Kato et. al. *	Hydrogen bubble	2.80
Wu	Floats	3.95
Present data	Paper	3.11

*Wind velocity is referred to as free stream wind velocity

Tang et.al (1978) plotted the ratio of drift velocity to mean wind velocity against mean wind velocity and from their plot they showed that the value of the velocity ratio is approximately constant for a range of wind speeds as shown in Figure 2.24.

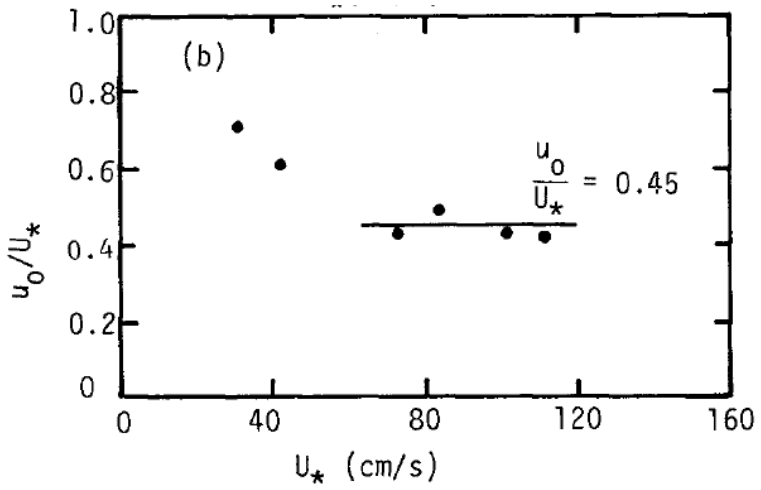

Figure 2.24 Plot of ratio of drift velocities to mean wind speed against mean wind speed (after Tang et.al, 1978)

A value of 0.030 (3%) is commonly accepted for the ratio of water surface velocity to wind velocity (Tsanis 1989).

2.13 Summary

The materials presented in Section 2.2 of this chapter discuss weir structures and the distribution of velocity over weir structures. The layout and complexity of the flow over the prototype structure is such that it is difficult to exactly relate the prototype to any of the weir structures discussed in the literature. Although the crest of the prototype weir is broad in the direction of the flow, depending on the head in the canal it may operate either as a sharp-crested, short-crested or broad-crested weir. For the data collected in this research the weir operates like a short crested weir. In addition, the prototype structure is similar to a side weir; however, the end contractions of the prototype are re-entrant, and as a result create complex flow condition as compared to a typical side weir. Furthermore, standard weir discharge measurement equations should be cautiously applied to the prototype structure because of the complexity of the flow over the weir structure. The presence of the gate just downstream of the weir is an addition reason why standard discharge equations must be cautiously applied.

Particle tracking velocity provides a non-intrusive technique to estimate the approach surface velocity over the prototype weir. The above literature discussed the basic concepts of PTV and LPTV. LPTV has been widely used in many laboratory and field research examples; however, it is important to note that the results of LPTV in field research can be influenced by external environmental conditions such as wind speed and direction. Thus, understanding the effects of wind on the measured surface velocities was very important to understanding the results of the LPTV measurements.

Chapter 3. **Instruments and Tools**

3.1 Introduction

The main purpose of the experiments presented in this thesis is to determine the approach velocity and discharge over the G304 weir at various heads for both a model and a prototype structure. Instruments and tools used in this research include a Sony HDR-HC9, a Canon Vixia HF200 camcorder, a weigh tank, a timer, an ADFM Pro-20 Velocity Profiler, six SonTek 16 MHz ADVs, and Flow Field Captor MD (PIV/PTV software). Each of these instruments and tools are described in detail in this chapter.

3.2 High Definition Digital Camcorders

A Sony HDR-HC9 and a Canon Vixia HF200 HD digital camcorder were used for field and laboratory tests, respectively. These camcorders record high quality HD video directly to a removable SDHC memory card. The camcorders feature high definition image sensors that can capture video at 1920x1080 pixel resolution with a 10X optical zoom and 15X optical zoom for the Sony and Canon camcorders, respectively. The battery life of these camcorders can support about one and a half hours of continuous high quality video recording, though a power saving mode allows for longer use. In addition, the Canon camcorder supports external screens and can be controlled remotely by use of an infrared remote controller. This feature made installation and adjustment of the camcorder settings much easier.

The following characteristics of the camcorders are important for this research: (1) the pixel frame rate, (2) the shutter-priority and (3) the acquisition mode. The pixel frame rate defines the number of image frames in each second of video recording. For this research 30 frames per second was used for both cameras. The shutter-priority

defines the time of exposure, which is the length of time the shutter remains open. As the tracer particles move over the weir, they go from a subcritical flow regime to a critical flow regime, which results in acceleration of the particles. A short exposure time may fail to capture images of the tracers that are sufficiently bright, while a long exposure time will capture the particles at different positions in the same frame; hence, the particles appear to be elongated. Elongated particles are not optimal for analysis, as the imaged geometry of the particle will differ from the true geometry of the particle. For the field research, there was plenty of sunlight, and the exposure time was adjusted to reduce glare from reflections. The shutter speed was adjusted to compensate for changes in lighting, but was always relatively fast. For the laboratory research, a shutter speed of 1/100 was found to be the most appropriate. For both the field and laboratory measurements, the highest image resolution quality mode was selected.

3.3 Weigh tank

Discharge measurements in the laboratory were done using a galvanized steel storage tank with about 10 cubic feet capacity mounted on a Toledo scale (see Figure 3.1). The scale is a spring free dual pendulum movement scale that can support up to 1000 lbs. The weigh tank setup was able to measure a maximum flow of 1.8 cfs with an estimated relative uncertainty of ± 2%.

Figure 3.1 Weigh tank mounted on a Toledo scale

A diversion tank at the outlet of the tail tank was used to divert water into the weigh tank and the following equation was used to calculate the discharge:

$$Q = \frac{W}{\gamma t} \tag{3.1}$$

where Q is the volume flow rate of water through the model, W is the weight of the water collected in the weigh tank during the time t, and γ is the unit weight of the water. The time it takes for the water to flow into the weigh tank was measured using a stopwatch.

3.4 Acoustic Doppler Flow Meter (ADFM) - Pro 20 Velocity Profiler

The ADFM Pro-20 depicted in Figure 3.2 is a flow-profiling device suitable for measuring velocities and discharges in pipes and open channels with an accuracy of up to 2% of actual value, within a flow depth of 20ft (6m). It contains four piezo-electric transducers that emit short acoustic pulses as narrow beams pointing in different directions to measure four independent velocity components; a fifth sensor that points

vertically measures depth. The information presented in this section about the ADFM Pro-20 was obtained from Teledyne Isco (2009).

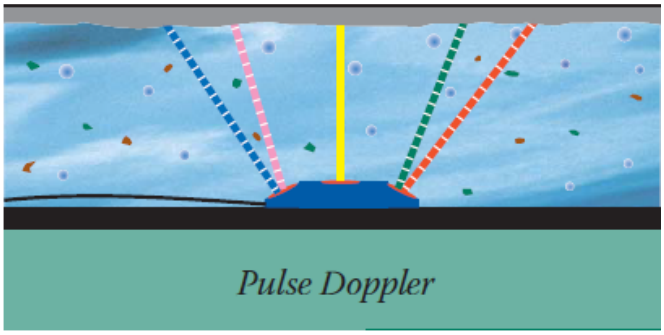

Figure 3.2 Pulse Doppler velocity profiling (Teledyne Isco 2009)

According to Teledyne Isco (2009), the device functions by using the Doppler shifted frequencies of echoes of the pulses backscattered by particles or bubbles in the flow to measure velocity. Each of the four velocity sensors measures one component of velocity, and assuming that the flow is homogeneous in horizontal planes, the four components can be combined to calculate a three-dimensional form of the velocity and an error estimate. ADFMs are often installed on the invert of a pipe flow or the bottom of an open channel flow as shown in Figure 3.2.

The ADFM is capable of measuring velocity at multiple points (or bins) in the water with a precision of 0.01ft/s. Measured velocity distributions are used to determine flow rates for the entire flow cross-section. The ADFM is not typically calibrated in situ, but relies on built-in algorithms to convert measured velocity profiles and geometric information into flow rates. An ADFM was used for discharge measurements in the culvert of the prototype G304 structure.

3.5 SonTek 16-MHz Acoustic Doppler Velocimeter (ADV)

ADVs are high-precision devices used for 3D velocity profiling in different flow environments. They have three basic components: a probe, a signal-conditioning module and a processor. The probe contains acoustic elements that function based on acoustic Doppler technology. It measures the flow in a small sampling volume located at a fixed distance of 5 or 10cm from the probe. The ADVs used in the experiments reported herein had measuring volumes that were 5 cm from the sensor. The probe is attached to the signal-conditioning module, and the two are connected to the processor. According to SonTek (2001), the ADV functions by transmitting acoustic waves from a central piezo-transducer. Suspended particles or bubbles in the flow backscatter the waves. Three directional receiving transducers measure the Doppler shifts of acoustic waves that are reflected by suspended tracers within the sampling volume. The three components of velocity are used to calculate a three-dimensional velocity vector at the location of the sampling volume (SonTek 2001). A diagram of an ADV probe tip is shown in Figure 3.3.

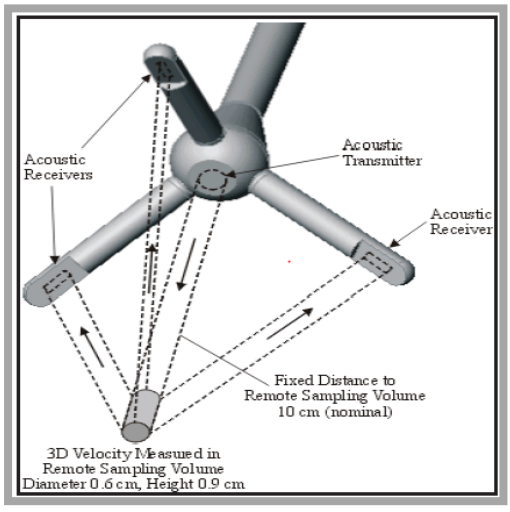

Figure 3.3 ADV transmitting and receiving probes

A tree of six ADVs was used for velocity and discharge measurement at the outlet of the culvert of the prototype G304 structure.

3.6 Additional Tools

Other basic instruments used in data collection include a stopwatch; thermometer, point gauge and a calibration mesh (for calibrating PTV measurements in the laboratory). A thermometer was used to measure the water temperature both in the field and in the laboratory. A point gauge was used in the laboratory to measure the height of water above the weir for each experiment. The calibration mesh was made of square metal pipes welded together to form a 70cm x 113cm (internal) rectangular frame. Fishing line and beads were then tied across the rectangular frame to make a rectangular grid of 20 cm by 20 cm squares. The purpose of the mesh was to make it possible to calculate the pixel-to-distance ratio for laboratory PTV measurements.

3.7 Flow Field Captor Multi-Dimensional PIV/PTV Analysis Program

The Flow Field Captor Multi-Dimensional (FFCMD) PIV/PTV Analysis Program was written by Dr. David Admiraal of the University of Nebraska Civil Engineering Department to do Particle Image Velocimetry and/or Particle Tracking Velocimetry on a set of image files to extract velocity data. The FFCMD program incorporates four primary functions: (1) preprocessing images, (2) image interrogation, (3) error identification, and (4) tabular, contour or graphical output of results. There are additional functions embedded within each of these four primary functions that were very useful to this research. These tools allow the following actions to be performed: (1) batch processing of large sets of image files, (2) extensive image filtering procedures, (3) editing background images and masking poorly lighted areas or unwanted solid objects,

and (4) deletion of spurious velocity vectors. Flow Field Captor MD also embodies a number of basic processing parameters that need to be set by the user prior to performing tasks related to the above mentioned primary functions. These basic functions, together with the afore-mentioned primary functions of the FFCMD, are discussed in detail in the following sections.

3.7.1 Preprocessing Image Filters in FFCMD

FFCMD includes several types of image filters that were developed for use in this project. For PTV, important image filters include the single point filter and the pixel intensity filter. The single point filter removes all PTV points that are composed of only one pixel; this is useful since multiple pixels are necessary to locate the centroids of a particle with sub pixel accuracy (Admiraal 2012). Image filters allow the user to define a pixel intensity cut-off value; the program then discards (by setting to zero) any pixel intensity below the set cut-off value. For PTV, two significant image filters are the pixel intensity probability density (PIPD) filter and the tracer geometry filter. The PIPD filter allows the user to specify a search radius, pixel quantity cut-off and pixel elimination range. The program searches within a box that has a height and width defined by the search radius and discards all pixels with intensities that occur with greater frequency than the user-defined cut-off value. The elimination range setting causes pixels with intensities that are close to the intensities of pixels that have been discarded to also be discarded. The concept behind this filter is that tracer particles have disparate intensities, whereas local background intensities are similar for the majority of pixels. Thus, pixels that have intensities with a locally high frequency of occurrence are unlikely to be tracers and are more likely to be background pixels. Setting such pixels to zero makes it easier

to identify tracers, especially in locations with multiple background intensities (e.g., the interface between shaded and un-shaded regions of the flow).

A sub-window available in the image filter dialog of FFCMD allows the user to click anywhere on an image to see a probability density function of pixel intensity frequency for the selected location and search radius. This tool makes it easier for the user to select an optimal pixel quantity cut-off and elimination range. A sample image is given in Figure 3.4, and the image filter sub-window is shown in the upper right corner of the image. The y-axis of the sub-window is pixel intensity, and the x-axis shows the number of pixels within the search radius that have a given intensity. The filter discards pixel intensities with frequencies that cross the red cut-off line shown in the sub-window. All pixels with intensities that are within the specified elimination range of a discarded pixel are also discarded.

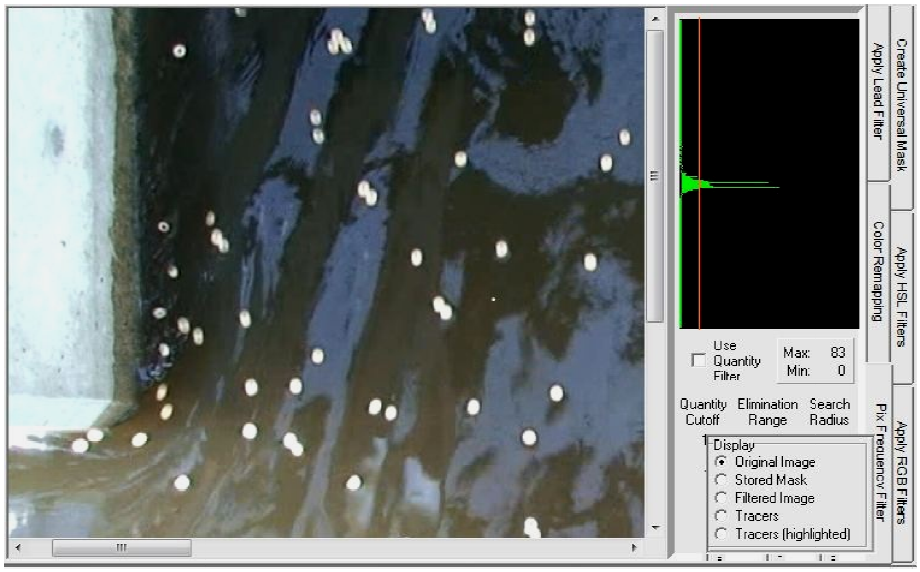

Figure 3.4 Image filter window

A tracer geometry filter can be used to reject pixels based on defined geometric parameters such as particle size and roundness. Settings for this filter are selected based

on the point rejection criteria shown in Figure 3.5 and applied in the image filtering window. When the "use tracer range filter" checkbox in the color ramping dialog window is selected, the program filters images based on geometric rejection criteria. This process can be performed simultaneously with the pixel frequency filter. The tracer geometry filter discards groups of pixels that do not match limiting physical characteristics of tracer particles specified by the user. Adjustable parameters include the acceptable minimum and maximum number of pixels belonging to a particle tracer group, the minimum size of the minor axis (in pixels), the maximum size of the major axis (in pixels), the maximum ratio of the major and minor axes, and the roundness of the tracer.

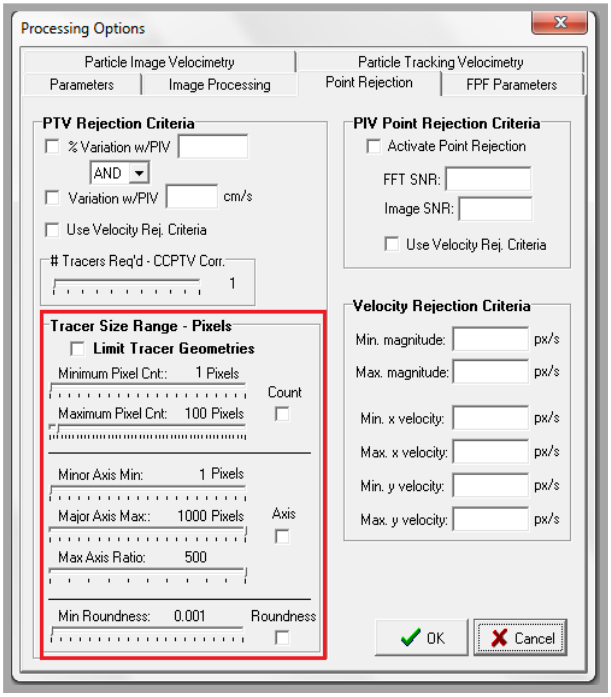

Figure 3.5 Point rejection window

3.7.2 FFCMD Image Processing

3.7.2.1 Image separation time dT(s)

Image separation time is a primary input function required by the FFCMD program for velocity calculation. This is the time, in seconds, between corresponding images. Videos were collected at 30 frames per second (fps); which means that the image separation time between successive image frames was 1/30th of a second. In some cases, in regions with low velocities, images that were not consecutive were selected for analysis to improve tracer displacement measurement accuracy. In these cases, the separation time was increased by the appropriate amount. The image separation time is specified in the dialog shown in Figure 3.6.

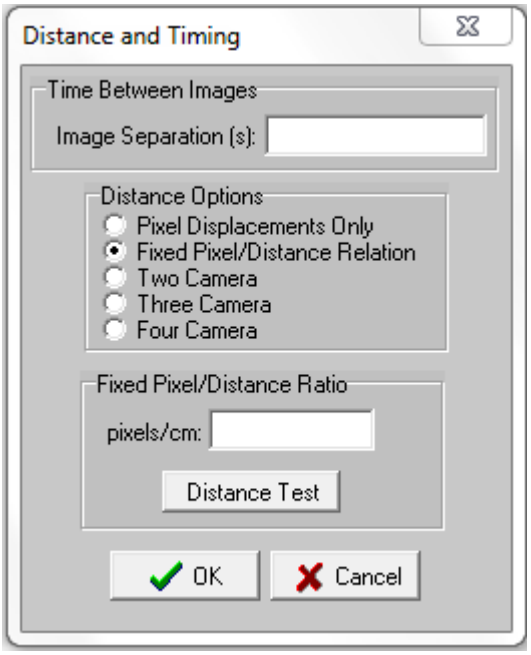

Figure 3.6 Fixed pixel/distance ratio calculator

3.7.2.2 Pixel-To-Distance Ratios

FFCMD applies the pixel-to-distance ratio entered by the user to convert pixel displacement measurements to distances and velocities with metric units. The ratio can

be obtained by placing an object of known length in the recording area and comparing its length to its length in pixels. An image of a mesh of known size or a measuring tape is commonly used to determine the pixel to distance ratio. A distance measurement tool embedded in FFCMD can be used to obtain the pixel-to-distance ratio from the image of a grid or tape. The pixel-to-distance ratio is specified in the same dialog as the image separation time.

3.7.2.3 Thresholding

The threshold intensity is the pixel intensity below which a pixel is assumed to not belong to a tracer and thus discarded. In FFCMD, either a user-selected fixed pixel cut-off value is applied or an automatic threshold is applied that sets the threshold intensity to a user-defined percentage of the highest pixel intensity observed within the interrogation window. Pixel intensity values below the cut-off value (whether constant or automatic) are considered to have zero pixel intensity and are discarded. Admiraal (2012) reported that auto-thresholding is most useful for images with spatially varied background intensities, for instance, if the images appear in both shade and sunlight. However, in this research, pixel frequency filters were more effective than automatic thresholds for discriminating tracer particles from the background.

3.7.2.4 Image Interrogation Techniques

Flow Field Captor MD utilizes several image interrogation techniques including PIV and PTV. The interrogative technique used for the purposes of this research is PTV. Flow Field Captor MD includes two particle-tracking algorithms, Nearest Neighbor Particle Tracking Velocimetry (NNPTV), and Cross Correlation Particle Tracking

Velocimetry (CCPTV). Both NNPTV and CCPTV can be performed either manually or as a batch process.

Nearest Neighbor PTV identifies particles in a second image, based on their proximity to a matching particle in the first image. According to Admiraal (2012), this routine works best for low densities of tracer particles. The program first locates the centroids of the tracer particles within the first and second images and then tries to identify matching particles in the second image for each particle in the first image, one particle at a time. To achieve this: the program first identifies all particles in the second image that are within a specified search radius of the particle in the first image, the particles in closest proximity to each other are then identified as a match. Of course, it is possible that the wrong pair of particles can be deemed a match if particle concentrations are high. The NNPTV process is illustrated using sample images from Admiraal (2012); Figure 3.7 shows particles for the same interrogation point in two consecutive image frames. The image on the left of Figure 3.7 is centered on the tracer for which a match is sought.

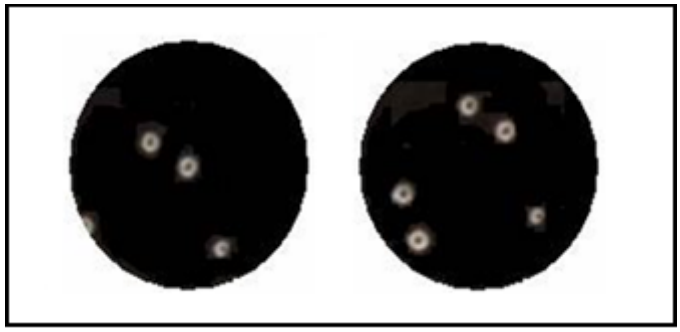

Figure 3.7 Particles in first and second image frames

Figure 3.8 shows the superposition of the one tracer from the first image for which a match is sought (the one found at the center of the search area in the first image)

and all of the tracers from the second image in Figure 3.7 (all of the possible tracer matches).

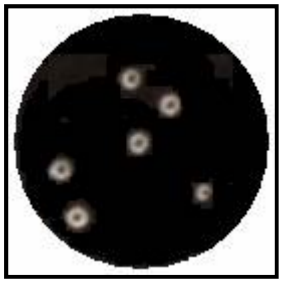

Figure 3.8 Superimposed first and second image

In Figure 3.9, the tracer at the center of first image is highlighted by a green circle; the best match from the second image is highlighted with a yellow circle and the second best match by an orange circle. The red circles identify other possible matches.

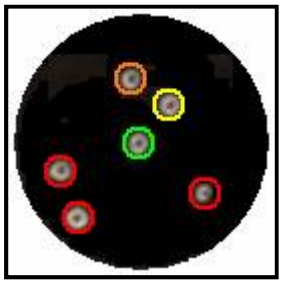

Figure 3.9 Possible particle matches

The NNPTV algorithm does not always find the correct match; success depends on the density of tracers in the vicinity of the search area. However, the program can conduct a preliminary PIV algorithm to improve the NNPTV search. In this case, PIV is first applied to get an initial estimate of local tracer displacement. The PIV displacement estimate is then used as an offset for the second image so that NNPTV can be applied with greater accuracy. The program can also be instructed to discard a match if a second possible match is identified within a close vicinity of the first match. Once all of the

particles in the first image have been analyzed for possible matches in the second image, the routine is complete.

3.7.2.5 Rejection Criteria

Vector rejection criteria can be applied during PTV analysis. Available rejection criteria in FFCMD are shown in Figure 3.5, above. They include PTV rejection criteria, PIV point rejection criteria, tracer size range criteria and velocity rejection criteria. For the purposes of this research, the important rejection criteria are the tracer size range (tracer geometry) and the velocity rejection criteria. Tracer size range criteria were utilized prior to PTV analysis and velocity rejection criteria were applied after the PTV analysis. No filters were applied during the analysis procedure itself.

3.7.3 Post processing Filters in FFCMD

For PTV, the program also has routines to identify erroneous velocity vectors. Erroneous velocity vectors may be the result of tracer mismatches or missing tracers due to lighting imperfections. The errors can exist in both magnitude and direction and it is very important that these erroneous velocities be deleted. The velocity filtering tools in FFCMD are embodied in the Vector Plotting Table and include universal filters, local filters, and manual removal (vector marking) as shown in Figure 3.10. The universal filter rejects velocities based on magnitude (minimum and maximum) and magnitudes of x and y components (minimum and maximum). Universal filters are applied to all vectors in the imaged area.

Local filters, on the other hand, are based on locally defined quantities. The user must first define: (a) a search radius, (b) minimum number of vectors, and (c) a percentage cut-off. The local filtering routine steps through all of the identified vectors.

For each vector, all of the vectors within the specified search radius are identified. The local filter is only applied if the number of vectors within the search radius is above the user-specified minimum number. If a sufficient number of vectors are available for comparison with the current vector, the vector is compared to all of the vectors within the search radius. The magnitude of the vector and the direction of the vector can be compared to the magnitude and direction of the surrounding vectors. If the percentage of the surrounding vectors that have magnitudes and/or directions that are in agreement with the current vector is higher than the percent cutoff, the vector is considered to be valid, otherwise it is discarded; the higher the percent cutoff, the more restrictive this criterion is (Admiraal 2012). The three comparisons that can be made with this filter are the percentage magnitude variation, the magnitude difference, and the vector direction.

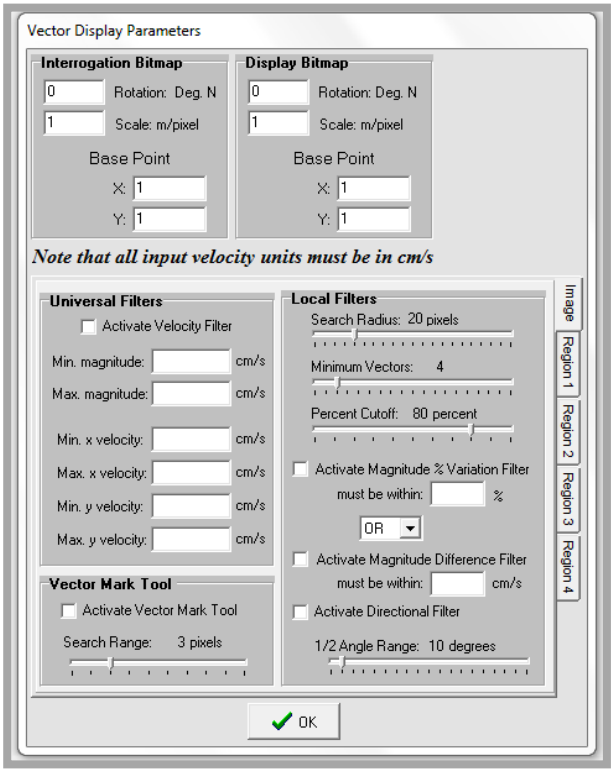

Figure 3.10 Velocity filter dialog window

The program can reject vectors that differ by a specified percentage of their magnitude from other vectors in their vicinity and vectors that differ in magnitude by a specified amount from other vectors in their vicinity. The directional filter rejects all vectors with directions outside the specified half angle range of the average direction of all local vectors.

FFCMD also has a regionalized velocity filter option that allows the user to apply a filter similar to the universal velocity filter but to smaller regions of the flow field. This tool is handy for rejecting spurious vectors in regions of an image where all of the correct vectors have the same general direction. The regionalized velocity filter is useful when there is significant variation in vector magnitude and direction across the imaged flow field, but there are also large regions where velocity variation is more limited.

Finally, FFCMD has a manual rejection tool that allows the user to identify spurious vectors manually in cases where none of the automated vector rejection tools work correctly.

3.7.4 Ancillary Functions of FFCMD

3.7.4.1 Batch Processing

Batch processing was used to efficiently apply filters and PTV processes to multiple pairs of images. Many of the processing tools described in the previous sections can be applied as batch processes. The two most important batch operations for this research are image velocimetry and special analysis tools. Figure 3.11 and Figure 3.12 show the batch operation windows for image velocimetry and special analysis tools. The image velocimetry tab is highlighted by the purple box in Figure 3.11. The buttons highlighted by the red-box in the figure include PIV and PTV options. Figure 3.12

shows the special analysis batch processing window. It contains the *Apply Filter* tool, shown by the green box, which allows the user to perform a set of image filtering functions on a batch of images. Also identified is the *Merge Vector* tool, shown by the blue box, which allows multiple batches of vector files to be merged into one comma delimited file (csv).

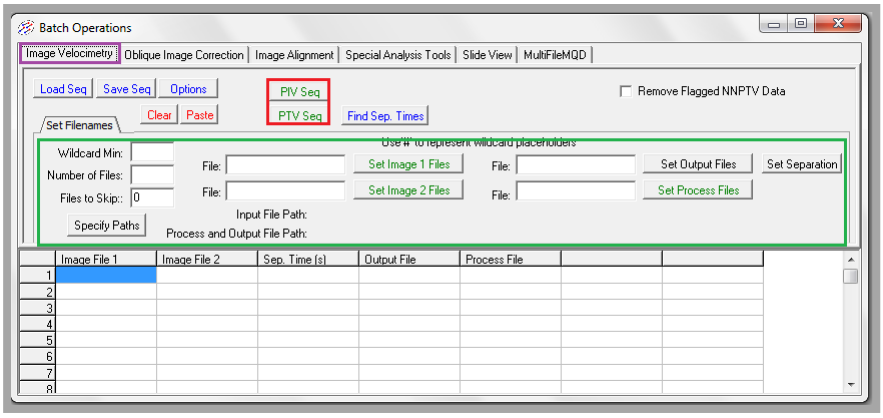

Figure 3.11 Image velocimetry batch operations

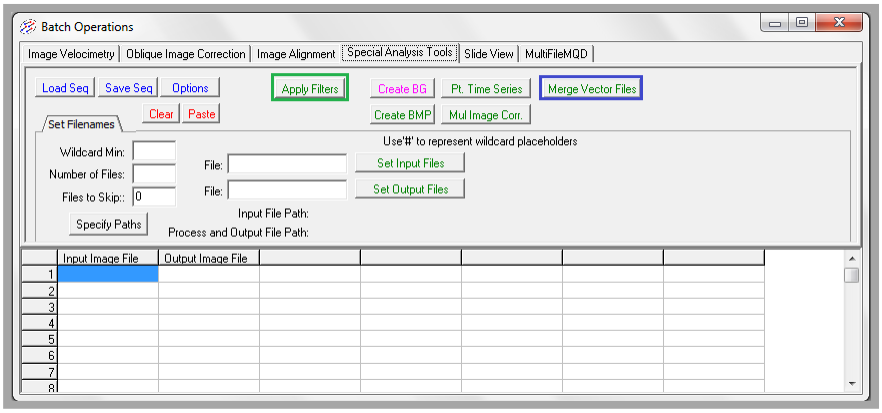

Figure 3.12 Special analysis tools batch operations

3.7.5 Vector Plotting

The vector plotting table in FFCMD allows the user to customize vectors, filter vectors, and display results. When filtering options described in section 3.7.3 are enabled, the vector plotting table allows the user to preview which vectors will be deleted prior to deleting them, enabling the selection of velocity filters to be optimized.

3.7.6 Contour and Program Settings

The Contour and Program settings panel contains two important components: contour interpolation settings, and display colors and settings. Contour interpolation settings include three functions: (a) setting the contour interpolation grid, (b) choosing a plot parameter, and (c) selecting grid interpolation options as shown in Figure 3.13. The contour interpolation grid allows the user to define grid geometry so that the program can search through velocity data in the Vector Plotting Table and assign individual vectors to the nearest grid points. The vectors assigned to each grid point can then be averaged and used for discharge calculations or contour plots. To plot contours, appropriate parameters and grid interpolation options must be set.

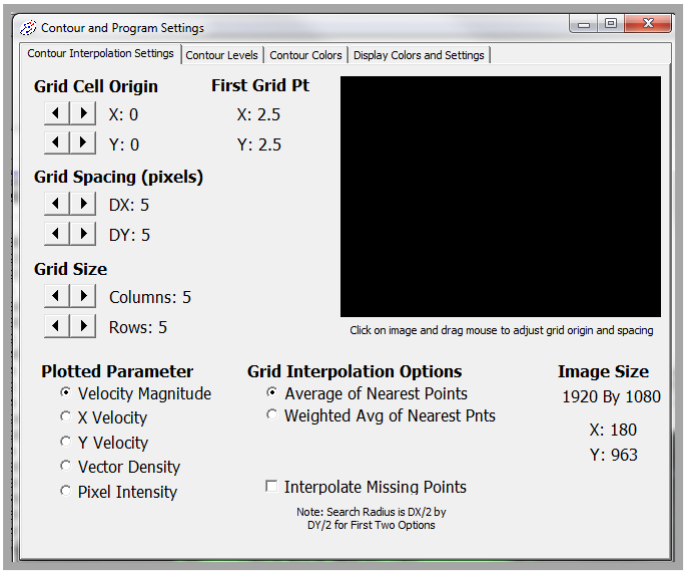

Figure 3.13 Contour interpolation settings window

Chapter 4. **Prototype and Laboratory Experiments**

4.1 Introduction

Experimental data were collected in both a prototype G304 structure and in a physical model G304 structure. Prototype data and initial processing will be discussed first, followed by some of the model measurements that were collected.

4.2 Prototype Measurements

Data were collected in the field for a G304 prototype (G304-I) on 02/10/2009 and 02/12/2009. These data are referred to as low head and high head tests for each day of testing, respectively. On each day, six tests were done, each with a different gate setting. During each test, LPTV data, ADFM data and ADV data were collected. David Admiraal of the University of Nebraska; and Juan Gonzalez and others from the SFWMD collected the data. Data and information presented in this section were obtained from the field notes and study report. The following data were collected for each test:

a. Large-scale PTV (LPTV) data were collected in the vicinity of the weir, upstream of the G304 inlet box. For each of the tests, two sets of data were collected: one each for the north (right abutment face) and south (left abutment face) side of the weir.
b. ADFM velocities and discharges were continuously collected inside the culvert.
c. ADV profiles were collected at the outlet of the G304 culvert.
d. Headwater and tail water stages: headwater and tail water elevations were collected before and after each test.

e. Finally, water surface profiles above the weir were also taken before each test.

4.2.1 Stage Measurements

Headwater and tail water elevations were collected at the start and end of each test for different gate openings, and the results are presented in Tables 4.1 and 4.2. Three types of stage data are presented in Tables 4.1 and 4.2. The types of data include DTW data, Control Room data, and Data Collection/Validation Pre-Processing (DCVP) data. DTW data are Distance-To-Water measurements that were manually collected on-site at the time of the tests. Control Room data are stage measurements that were reported by the SFWMD Control Room for the test times given (these are remotely collected stage data). Data Collection/Validation Pre-Processing consists of instantaneous pre-processed stage measurements that have not been converted to daily values or other processed forms of stage. All of the available stage data are in close agreement (within 0.01 to 0.02ft) but the DCVP data appear to be the most complete and most reliable because they are the ones directly reported by SFWMD as the correct values.

Table 4.1 Stage and discharge data summary for February 10, 2009

Test	Gate Opening (ft)	Start Time	End Time	Time	DTW		Control Room		DCVP		ADFM Results				
					Head W (ft-msl)	TW (ft-msl)	HW (ft-msl)	TW (ft-msl)	HW (ft-msl)	TW (ft-msl)	Avg Q (ft^3/s)	σ_Q (ft^3/s)	COV_Q	N	Avg T (F)
A2	0.5	13:40	14:15	13:38	12.16	10.96	12.14	10.95	12.14	10.95	9.00	1.14	12.7%	31	64.4
				13:50	12.14	10.96	-	-	12.14	10.95					
				14:13	12.13	10.96	12.12	10.95	12.13	10.95					
A3	1.0	14:36	15:05	14:35	12.12	10.95	12.11	10.95	12.11	10.95	22.7	0.72	3.2%	25	65.2
				14:53	12.11	10.96	-	-	12.09	10.95					
				15:03	-	-	-	-	12.09	10.95					
A4	2.0	15:15	15:46	15:15	12.11	10.95	-	-	12.07	10.95	22.5	0.52	2.3%	26	65.6
				15:32	12.08	10.96	-	-	12.07	10.95					
				15:45	-	-	-	-	12.05	10.95					
A5	4.0	15:47	16:28	15:48	12.06	10.95	12.07	10.95	12.05	10.95	21.2	0.81	3.8%	34	65.8
				16:12	12.04	10.95	-	-	12.03	10.94					
				16:28	-	-	-	-	12.02	10.94					
A6	0.76	16:35	17:23	16:43	12.03	10.95	12.01	10.95	12.02	10.95	16.9	0.81	4.8%	40	66.1
				17:10	12.00	10.95	11.98	10.95	11.99	10.95					
				17:25	-	-	-	-	11.98	10.95					

HW = Head water stage
TW = Tail water stage
Avg Q = Average Discharge measured with the ADFM
Avg T = Average Temperature measured with the ADFM

Table 4.2 Stage and discharge data summary for February 12, 2009

Test	Gate Opening (ft)	Start Time	End Time	Time	DTW HW (ft-msl)	DTW TW (ft-msl)	Control Room HW (ft-msl)	Control Room TW (ft-msl)	DCVP HW (ft-msl)	DCVP TW (ft-msl)	ADFM Results Avg Q (ft^3/s)	σ_Q (ft^3/s)	COV_Q	N	Avg T (F)
B2	0.49	14:14	14:56	14:15	12.90	11.00	12.90	11.00	12.90	11.00	13.3	0.86	6.5%	36	65.9
				14:32	-	-	-	-	12.90	11.00					
				14:57	12.91	11.00	-	-	12.88	11.00					
B3	1.0	15:04	15:44	15:04	12.88	11.02	12.88	11.02	12.88	11.01	31.7	0.80	2.5%	33	65.7
				15:27	12.86	11.01			12.86	11.00					
				15:45	12.85	11.00	12.83	11.00	12.83	11.00					
B4	2.0	15:53	16:37	15:54	12.85	11.02	12.84	11.00	12.84	11.00	56.5	1.41	2.5%	36	65.4
				16:14	12.81	11.00	-	-	12.78	11.00					
				16:36	12.78	11.00	12.77	11.00	12.77	11.00					
B5	4.0	16:43	17:32	16:43	12.75	11.01	12.74	11.00	12.74	11.00	56.1	1.70	3.0%	40	65.0
				17:10	12.73	11.00	-	-	12.70	11.00					
				17:32	12.65	11.01	12.67	11.00	12.67	11.00					
B6	1.5	17:39	18:15	17:40	12.63	11.01	12.64	11.01	12.64	11.01	45.3	0.84	1.8%	30	65.2
				17:59	12.61	11.00	-	-	12.62	11.01					
				18:18	12.59	11.00	12.60	11.01	12.62	11.01					

4.2.2 ADFM Measurements

ADFM measurements were collected near the outlet of the culvert for each test. Figure 4.1 depicts an ADFM in a pipe flow. The ADFM was installed on the invert of the culvert approximately one culvert diameter upstream of the culvert outlet and it was set to take velocity profile readings every 10 seconds. The data collected with the ADFM were extracted using an ADFM file reader and converted to velocity profiles and discharges. Average discharges associated with the field test ADFM measurements are provided in Tables 4.1 and 4.2. The average discharges are calculated from the N discharges specified in the tables. In addition, the standard deviation and coefficient of variation of discharge for each test is also provided. The ADFM also records water temperature, and the average water temperature for each test run is provided in the table.

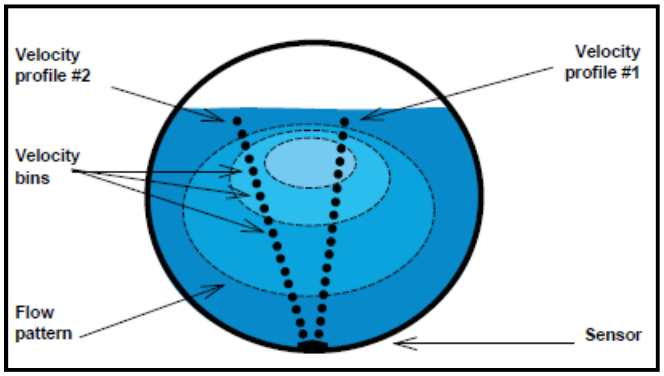

Figure 4.1 Depiction of an ADFM installation and operation in a pipe flow (Teledyne Isco 2009)

4.2.3 ADV Measurements

Additional velocity measurements were collected at the outlet of the culvert in the form of ADV velocity profiles. The velocity profiles were collected with six ADVs mounted on a vertical pole. The pole was moved between three positions: a south profile, a center profile, and a north profile, denoted by the suffixes s, c, and n, respectively, as shown in

Figure 4.2. The three vertical profiles were 1.5 feet apart with the center profile on the axis of the culvert. The ADVs mounted on the pole had a vertical spacing of 1.0 ft. The culvert was not always completely submerged, and so the depth H was also recorded for most tests. Occasionally, a measurement was invalid because the probe measurement volume was outside of the radius of the pipe; such measurements were discarded.

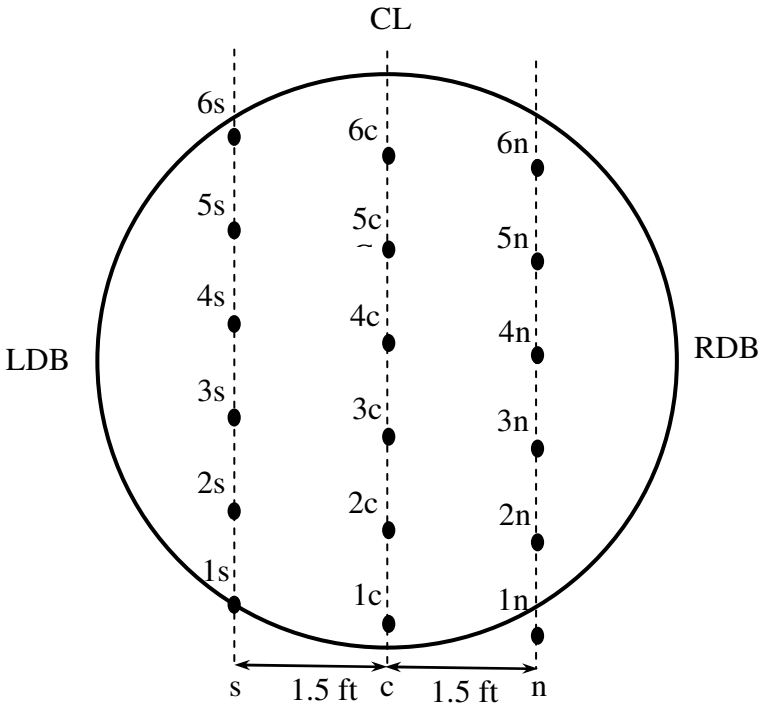

Figure 4.2 End view of G304 outlet depicting transect along which velocity measurement was taken

In order to calculate the discharge in the culvert from the ADV measurements, the ADV measurements were averaged in time and integrated across the culvert outlet. To do this, several steps were followed:

1. All ADV data were first filtered to remove bad data. Only data with a minimum acoustic correlation of 70%, a minimum Signal to Noise Ratio (SNR) of 15, and a maximum SNR of 50 were used. The maximum SNR was used because higher values were clearly associated with a number of data spikes – probably because of

large objects (e.g., fish) in the flow. The data removed by the filters were typically less than 0.5% of the total data. Filtered and unfiltered average velocity data were compared and in most cases were identical.

2. The X, Y, and Z components of each velocity signal were individually averaged for each ADV measurement.
3. The exact axis of the G304 culvert was unknown and although the ADV mount was placed as close to perpendicular to the culvert as possible by eye, there was still misalignment with the flow direction. The angle of misalignment was calculated using the averages of the X, Y, and Z ADV velocity components from all of the valid probes and all of the tests. Rotation misalignment of the ADV probes about the horizontal axis was found to be negligible (less than 1 degree), but rotation misalignment of the probes about the vertical axis was found to be 9.7 degrees. The coordinate system of the ADV probe outputs was rotated by 9.7 degrees so that the mean velocity of the flow did not have any non-zero components in the directions perpendicular to the stream-wise axis.
4. Filtered/Averaged/Rotated ADV data were used to compute discharges by integrating across the outlet of the G304 culvert. Several methods of integrating the ADV velocities were investigated, all of which fit a theoretical velocity distribution to the velocity data and then integrated the velocity distribution from the center of the culvert to the outside radius. The velocity defect law was chosen as the most appropriate theoretical velocity distribution and was used to compute the discharges presented in this thesis, though all of the velocity distributions produced similar results.

4.2.4 Large-Scale Particle Tracking Velocimetry Measurements

For each test, large-scale particle tracking was conducted to measure the surface velocity distributions over the G304 weir flow area. It was impossible to install the camera to capture the entire flow area above the weir due to the width of the G304 structure. Therefore, the camera was mounted to view the left and right half of the area of interest alternately as depicted in Figure 4.3. As shown in Figure 4.3, there was some overlap between the imaged areas of the two sides of the weir.

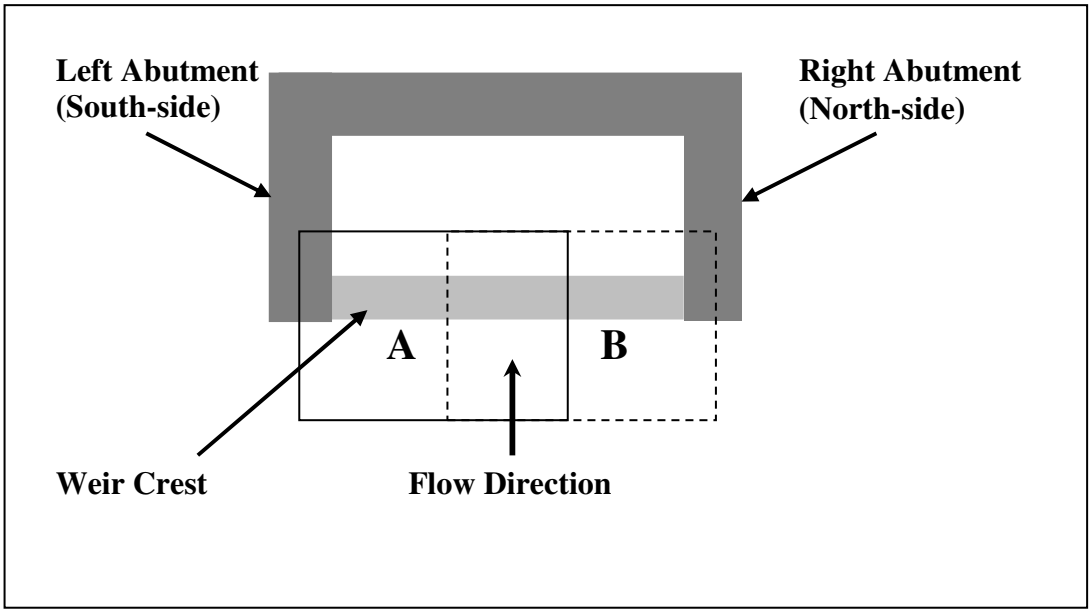

Figure 4.3 Camera plane view of the G304 structure

The camera was first mounted above area A and then above area B. LPTV data that were collected for the two areas were processed separately and then combined to get the velocity distribution over the entire length of the weir. The camera positioning sequence was repeated for all tests. The flow was seeded with Cheerios as tracers and a video recording was taken for approximately two to three minutes for each test in Table 4.1 and 4.2 and for each sub-area shown in Figure 4.3. The camera recorded images at 30 frames per second. Each video recording was transferred to an external hard drive to be

processed later. The video recordings were later converted into 24-bit bitmaps for use in FFCMD.

4.2.5 Pre-filtering LPTV Images with FFCMD

The most important objective in image pre-filtering was to eliminate as much background noise and as many misidentified tracers as possible while retaining the majority of true tracer particles. LPTV Images were preprocessed with three relatively powerful filters: (1) a pixel intensity probability density filter that improved particle identification in images with non-uniform background lighting, (2) a threshold that discarded pixels with intensities that were below those that were expected of tracer particles, and (3) a tracer range filter, which rejected all identified tracer particles that did not match the expected size and shape of seeded flow tracers (e.g., if an object identified in the image was much larger than what a typical particle should be, it was rejected). To apply image filters in FFCMD, the individual 24-bit bitmaps were opened in the masking and filtering dialog.

For the pixel intensity probability density filter (PIPD filter), three processing parameters were specified: the quantity cut-off, the elimination range, and the search radius. The PIPD filter compared the intensities of all of the pixels within the distance specified by the search radius. Since the PIPD filter was applied only to local pixels (those within a specified search radius), it was an excellent tool for identifying tracer particles in the images with non-uniform illumination such as those collected in the prototype.

The threshold filter simply scanned through all of the pixels in each image and discarded the pixels with intensities that were below the threshold. These were intensities

that were so low that they are not likely to be part of a tracer particle. PTV must always have a threshold intensity set so that the particles can be differentiated from the flow background.

The tracer range filter allowed noise to be removed by rejecting parts of the image that were identified as particles but did not have expected tracer particle geometries. The particle geometric characteristics that could be used to determine if an identified particle should be rejected included: tracer size (number of pixels that make up the tracer), Major axis of the tracer (pixels), minor axis of the tracer (pixels), ratio of the major and minor axis, and roundness (a comparison of the number of pixels to the length of the perimeter). The tracer range filter was helpful for eliminating apparent particles that were actually reflections from the sun or other light sources.

Of the filters, the PDIP filter was the most useful and was extensively used for filtering field measurements because of their high degree of non-uniform lighting illumination. The PDIP filter was not as important for laboratory measurements, where lighting was less difficult to control. The filters and filter settings were optimized to achieve the best results for identifying particles and eliminating noise. A typical example of an original image file before and after image filtering is shown Figure 4.4 and Figure 4.5, respectively.

Figure 4.4 Prototype G304 LPTV image prior to filtering

Figure 4.5 Prototype G304 LPTV image after it has been filtered

Once suitable filter criteria were identified, the filters were applied to all of the images from the prototype runs using a batch process.

After the G304 prototype images were pre-filtered to eliminate background noise, FFCMD was used to identify tracer centroid displacements between images. The tracer displacements and the times between images were used to determine velocity vector fields. The camera recording speed was 30 frames per second, so the usual separation time between LPTV images was $1/30^{th}$ of a second. The separation time was occasionally increased to increase particle displacements by skipping LPTV images, but this was unnecessary in most cases because particle displacements were sufficiently large using sequential images.

For the present research, we chose to apply an offset-based Nearest Neighbor PTV (NNPTV) algorithm because tracer densities were very low. The nearest neighbor PTV algorithm was applied with a PIV Offset enabled. The program first identified the centroids of all of the particles in a first and second interrogation image. Then, at the location of each centroid identified in the first image, a Fast Fourier Transform-based PIV algorithm was applied to find the most probable displacement of the group of particles in the near vicinity of the centroid. The PIV-based displacement was used as a preliminary estimate of the displacement of each individual particle, and the particle from the second image that had a position that was closest to the position predicted by the PIV-based displacement was chosen as the PTV match. Finally, the difference between the centroids of the PTV match was calculated to yield the displacement of the particle from image 1 to image 2. Dividing the displacement by the separation time between the two images yielded the particle velocity. This process was repeated for every tracer particle identified in image 1.

The program identified numerous tracer match errors when the offset-based NNPTV algorithm was applied. Errors that led to erroneous particle matches included: (1) erroneous PIV offset calculations, (2) when two tracer particles in the first image had the same endpoint tracer in the second image, (3) when alternate tracers were not within the search range, (4) when rejection criteria were not met, and (5) when a valid match was not found. The program flagged the errors, and erroneous tracer matches were automatically deleted.

4.2.6 Calculation of the Pixel-to-Distance Ratio

In order to calculate velocity in real units, a pixel-to-distance ratio was entered into the program as discussed in Section 3.7.2.2. For the prototype measurements, the pixel-to-distance ratio was determined by placing a surveying rod on the water surface when there was no flow over the weir. The true distances between marks on the surveying rod were then compared to the numbers of pixels between the marks in the images to get the pixel-to-distance ratio. The surveying rod was placed parallel to the leading edge of the weir in imaging areas A and B for both the low and high stage tests described in Tables 4.1 and 4.2.

Sample calibration images are shown in Figures 4.6 and 4.7 for the south and north low head tests, respectively. For the low head tests, the pixel to distance ratios were determined to be 10.45 and 10.42 pix/cm for the south and north sides, respectively, and for the high head tests, they were 7.73 and 7.65 pix/cm, respectively. Based on the survey rod measurements, average fixed pixel-to-distance ratios of 7.69 pixel/cm, and 10.44 pixel/cm were used for the February 10 and February 12 tests, respectively.

Obviously, the accuracy of the final velocity measurement was dependent on a good estimate of the pixel to distance ratio. The size of an image formed by a camera lens is dependent on the size of the object, the camera lens focal length and the distance of the object from the camera lens. Thus, the closer an object is to the camera, the larger the resulting image size and consequently the larger the pixel-to-distance ratio. For the duration of the prototype tests the camera was installed at a fixed distance above the water and the camera zoom was kept constant, but as the gate opening was changed for each test, there was also a slight change in the distance of the water surface from the camera. This change in the distance between the water surface and the camera is a source of error in the velocity measurement. For the prototype tests it leads to a small underestimation of the water surface velocities since the pixel-to-distance ratio is overestimated by the calibration measurements.

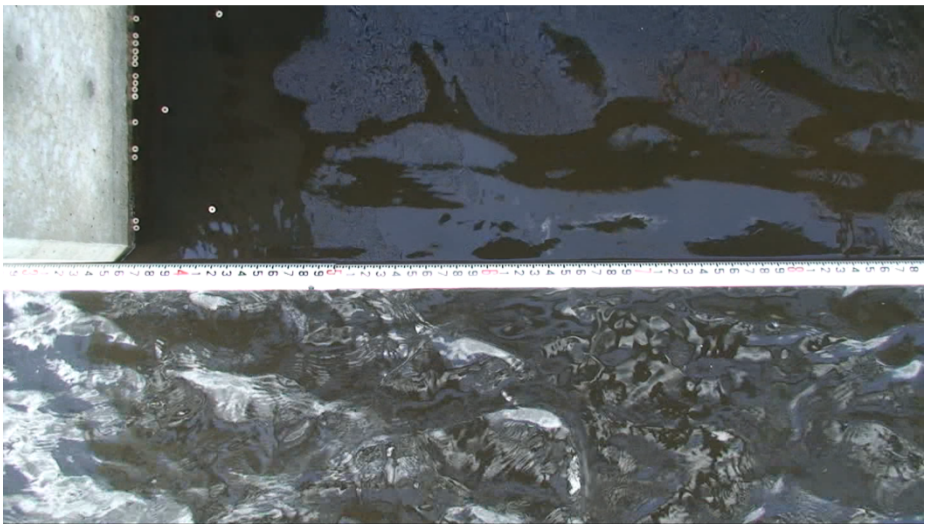

Figure 4.6 Survey rod used for pixel/distance estimation (low head tests, left abutment)

Figure 4.7 Survey rod used for pixel/distance estimation (low head tests, right abutment)

4.2.7 Vector Output Files

Following preliminary image filtering, the NNPTV algorithms were applied to each pair of image files in the LPTV dataset using a batch sequence. Results from analysis of each pair were output to a comma delimited vector output file. To obtain a complete vector velocity distribution of all of the particles as they flowed over the weir, these individual vector files were merged into one file using a merge function in FFCMD. Having the vectors in one file allowed the vectors to all be displayed on one image, and also allowed several special post-processing filters to be applied to the vectors simultaneously.

4.2.8 Application of Velocity Filters during Post-Processing

Even after pre-processing of the LPTV images, a large number of spurious vectors must still be removed from the results by applying velocity vector filters. Figure 4.8 shows the vectors determined during LPTV analysis of one of the flows over the prototype G304 weir. As discussed in Chapter 3, FFCMD has a number of filtering

options embedded in the post-processing functions that can be used to remove the erroneous vectors.

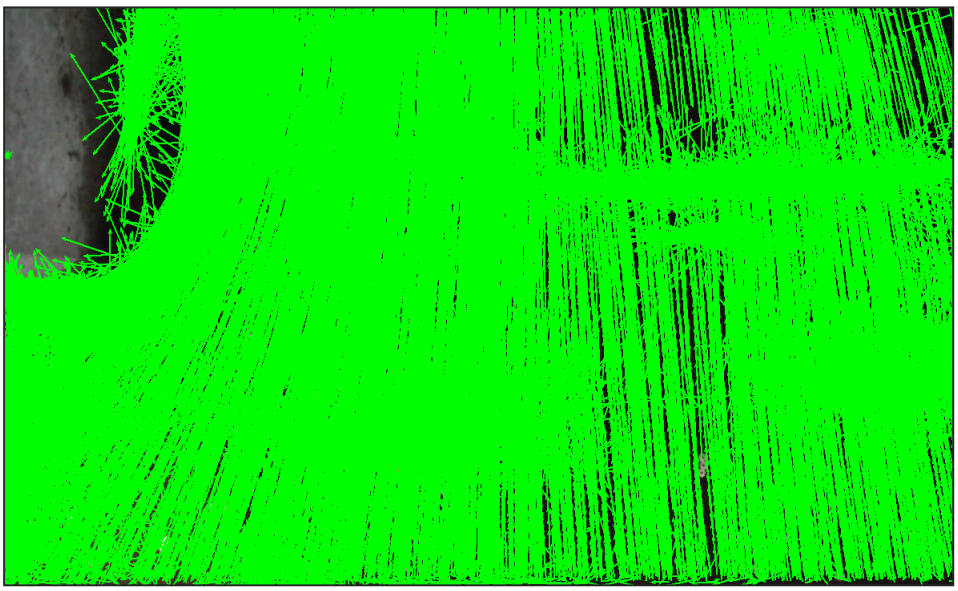

Figure 4.8 Vectors plotted for prototype Test B5 before applying vector filters

From vector plots like the one shown in Figure 4.8 there were many spurious vectors that did not represent the actual flow conditions. It was obvious that either these spurious vectors did not agree with the flow direction or the magnitude of the vectors did not agree with other vectors in the vicinity. These spurious vectors resulted from: (1) reflections of sunlight; these reflections can be mistakenly identified as particles or can cause some particles to be removed during the image filtering process, (2) too many particles, making particle identification by NNPTV difficult, and (3) air bubbles near the abutments which can be mistaken for tracer particles. In addition particles can become trapped near the abutments in regions with recirculating flow. It was essential that these bad vectors be identified and removed.

There were two post-processing filter options in FFCMD that were used extensively: universal and local filters. As mentioned earlier, the universal filters were

applied either to the entire flow field or to large regions of the flow field. On the other hand the local filters were applied to small regions of the image. The local filters were most useful. They analyzed vectors one at a time and compared them with vectors in their immediate vicinity. Such comparisons were time-consuming for large datasets (merged PTV files for both the prototype and model were typically composed of 100,000 to 200,000 vectors), but produced very good results. The most practical approach was to apply universal filters first, eliminating as many bad vectors as possible, and then running the more time-consuming local filters on the smaller vector field, thus saving computational time. The criteria used for the vector filtering process were obtained by trial and error and were consistently applied for all datasets. Results obtained after running each filter were closely observed to confirm that only the spurious vectors were marked for deletion. The vector field was divided into several regions based on the prevalent magnitude and direction of local vectors. This made it easier to apply selected filters to isolated areas of the vector field, minimized processing time and improved the results of the filtering process.

4.2.8.1 Universal Filters

Universal filters included filters that were applied to the entire flow area or to specific regions of the flow area. For example, for the tests in the prototype, the maximum velocity magnitude was set to 170 cm/s, and the minimum velocity perpendicular to the weir face was set to zero. These values were determined by observing the vectors in the analyzed images and determining which vectors were obviously spurious vectors based on other vectors calculated in the same region. The program that was used contained a tool that allowed the user to scroll through the vectors

and to display only a fraction of the total number of vectors at a time. That made it easier to verify that all the vectors marked for deletion were indeed spurious vectors. When it was clear that spurious vectors were not being correctly identified, the filtering criteria were refined. Regional filters were also applied. For instance in some regions of the flow, correct velocities were clearly in one direction (e.g., from right to left in the image). In such cases, a regional filter was applied to reject spurious vectors that were not in the known direction of flow. The difference between universal and regional filters was that regional filters were applied only to a sub region of the imaged flow area, whereas universal filters were applied to the entire flow region. As an example, marked vectors that were filtered using regional and universal filters are shown in red in Figure 4..

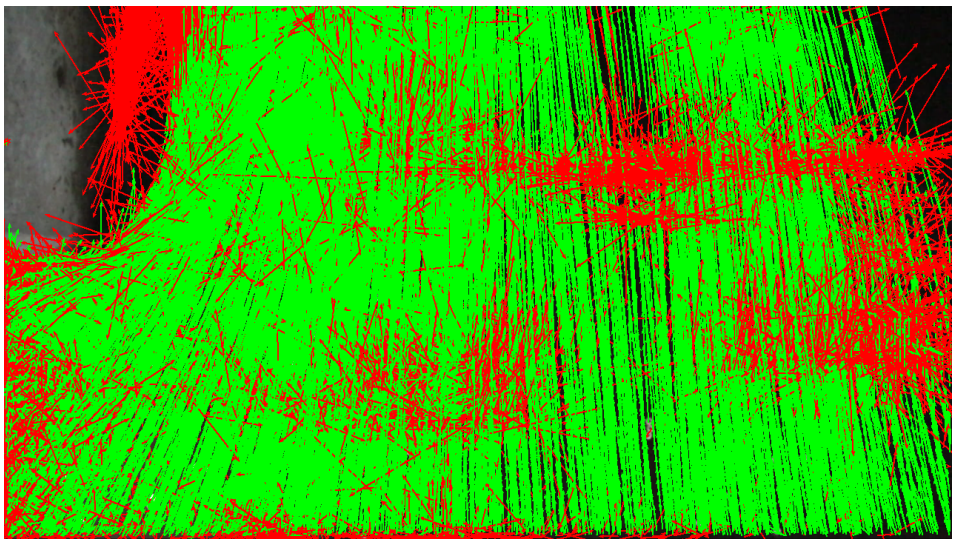

Figure 4.9 Vectors marked red for deletion after applying universal and regional filters (Test B5)

The vector field that remained after applying universal and regional filters is shown in Figure 4.10.

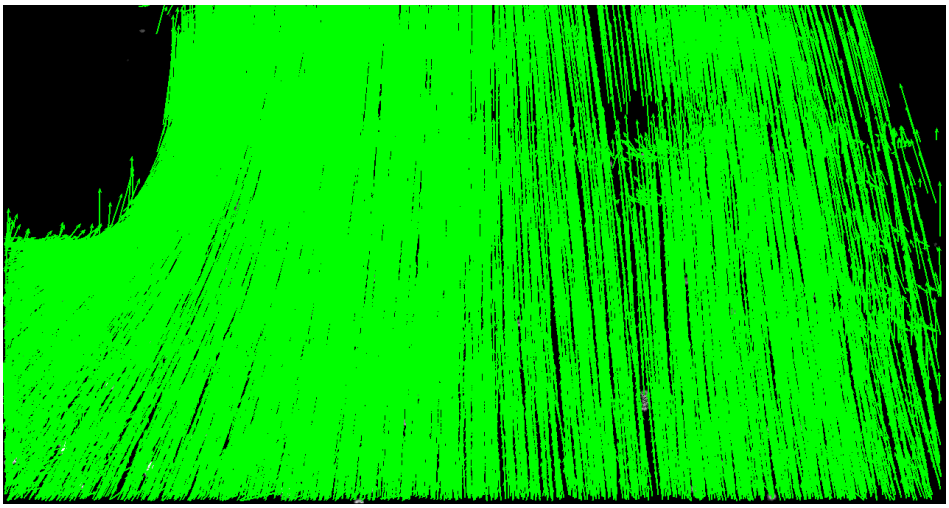

Figure 4.10 Vector plot after applying universal and regional filters(Test B5)

4.2.8.2 Local Filters

As seen in Figure 4.10, although the universal filter was a very effective tool for removing spurious vectors, a number of bad vectors remained, and local filters were applied to remove additional spurious vectors. For detailed explanation of local filters, see Section 3.7.2.4. The search radius was set to 20 pixels, the minimum vectors to 10, the percentage cut-off to 70%, the magnitude percentage variation was required to be within 25% and the directional filter half angle was set to 18 degrees. Essentially, the program searched through all of the vectors that remained after universal filters had been applied and: (1) found the number of vectors within 20 pixels of the present vector, (2) determined if there were more than 9 vectors within that search radius. If the minimum number of vectors criterion was met, the program (3) found the average magnitude and direction of the vectors within the search radius, (4) compared the magnitude and direction of the present vector to the average magnitude and direction of the surrounding vectors, and (5) marked the present vector for deletion if its magnitude or direction were

not in agreement with at least 70% of the magnitudes and directions of the surrounding vectors. All other filters were deactivated, and the filter process was initiated.

Following application of local filters, there were still a few remaining vectors that were obviously bad and were removed by hand. Figure 4.11 shows an example of a final velocity distribution plot adjacent to the left abutment of the prototype weir for test B5. The filter procedure with appropriate filter criteria was applied to all the PTV tests conducted in the prototype. The prototype LPTV tests were conducted for overlapping sections of the north and south sides of the G304 weir separately as discussed in section 4.2.2. Similar to Figure 4..11, Figure 4.12 shows the final filtered vector distribution plot over the right abutment end of the weir for Test B5. Note that in both images there were parts of the flow where there were fewer vectors. The lower density of vectors was caused either by a lack of tracer particles reaching those parts of the flow or by light reflections that interfered with particle identification in those regions.

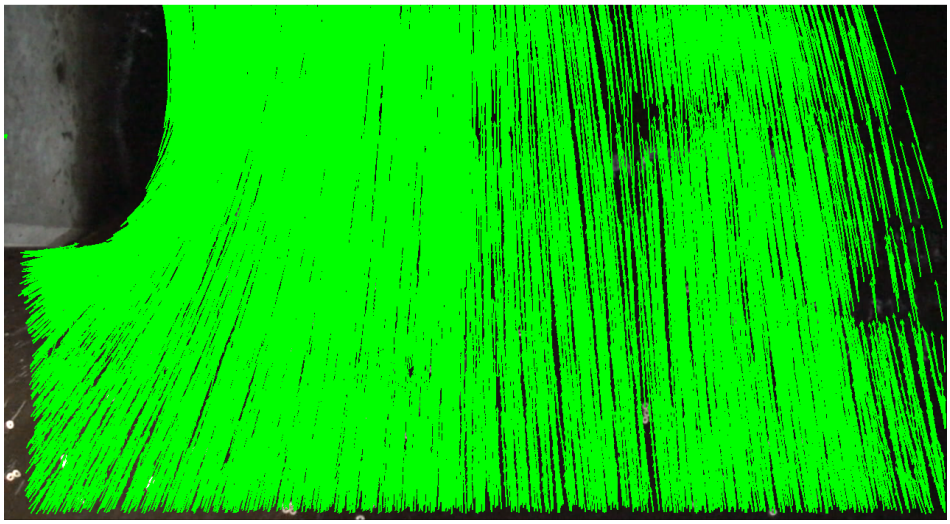

Figure 4.11 Final filtered Test B5 (4.0 ft gate opening - south side)

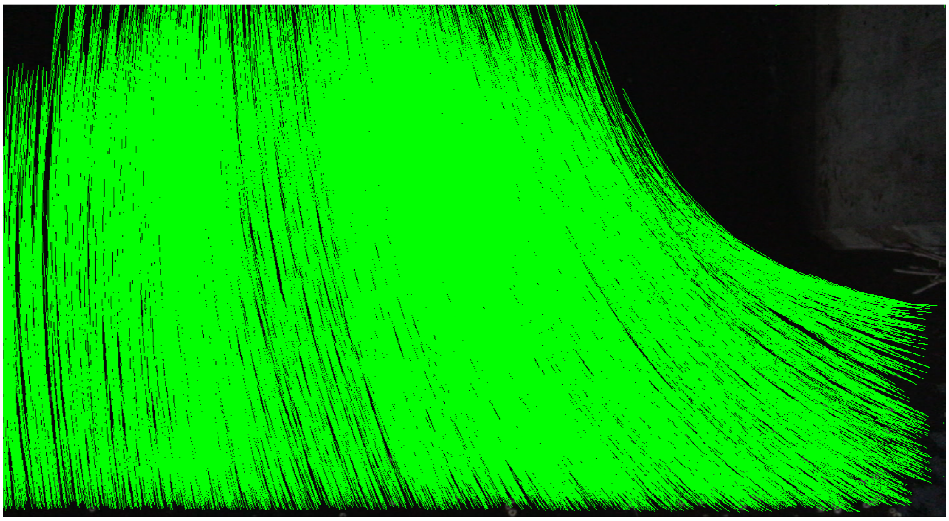

Figure 4.12 Final filtered Test B5 (4.0 ft gate opening - north side)

4.2.8.3 Combining LPTV image and vector data sets

As previously explained, LPTV data were collected separately for the north and south sides of the weir for each test. It was necessary to combine the complete vector data set for the prototype test into one image for each test; this was done in two phases: (1) north and south images were combined into one image that covered the full length of the weir; this was accomplished by shifting one of the images using a function built into the processing software, and (2) Excel was used to shift the x and y coordinates of the vector data set that belonged to the image that was shifted by the same amount that the image had been shifted.

First, the program was used to open both a north and a south image, simultaneously. Using the mouse, the north image (the one on the right) was dragged until the north face of the south abutment and the south face of the north abutment were aligned as shown in Figure 4.13 .

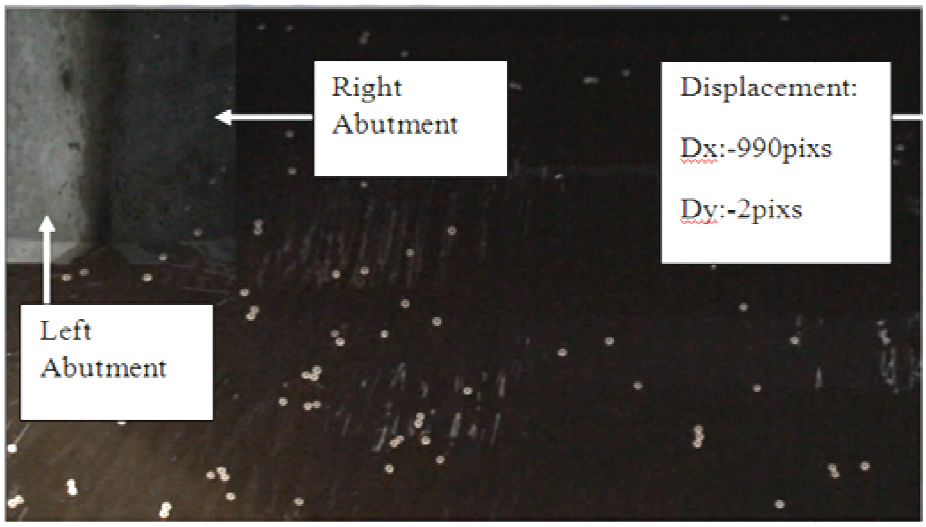

Figure 4.13 Overlapping north and south images with the abutments aligned face to face

The true length of the weir structure was known, and using the known scale of the images the equivalent length of the weir in pixels was determined for each test. The image of the north abutment was then shifted to the right so that the distance between the faces of the two abutments was exactly the same as the length of the weir (measured to be 268 cm). An example of the resulting combined image is given in Figure 4.14; this image was developed in the program and then saved for displaying vectors. The process was repeated for all of the prototype tests and the resulting combined images were saved for use with vector plots.

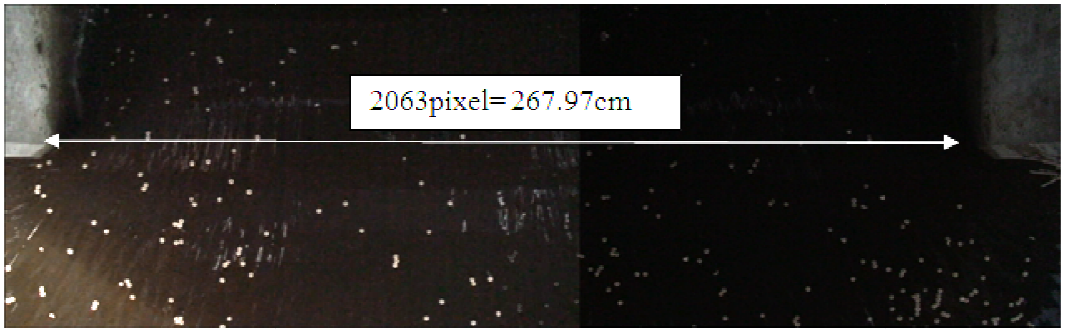

Figure 4.14 Combined images representing the entire G304 weir structure

The size of the images for all LPTV data collected on February 10 and 12 was 1280 pixels by 720 pixels, and vector data were collected across most of the image. LPTV measurements included both x and y velocity components and positions of the velocity measurements in x and y coordinates (in pixels). Prior to combining velocity data from the north and south sides of the weir, the velocity measurements associated with the north side of the weir had to be shifted by the same amount that the image of the north side of the weir had been shifted when the north and south images were merged. The vectors associated with tests by the north abutment were all shifted using Excel, and then the south and north vectors were combined into one data set.

The combined vector distribution for Test A5 is given in Figure 4.15 . Note that overlapping vectors at the center of the weir are not in complete agreement. The day on which the experimental data were collected was quite windy, and there is evidence that suggests that strong wind had an influence on surface flow patterns. Inconsistencies in the centerline velocities were likely due to changes in wind patterns between the two test sets.

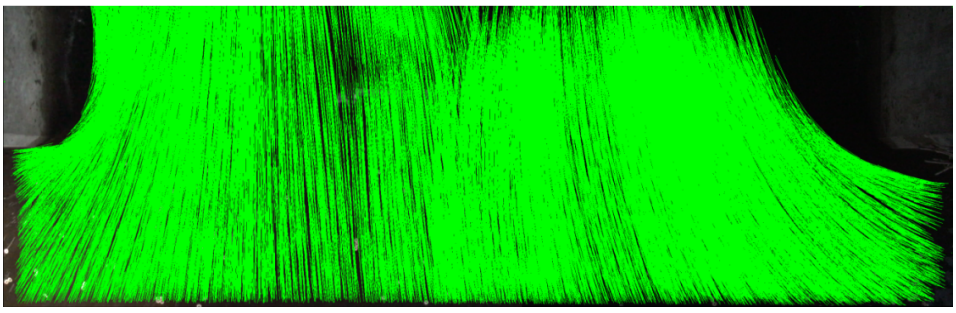

Figure 4.15 Velocity distributions over the entire G304 weir structure for Test A5

4.2.9 Water Surface Profile Measurements

Water surface profile measurements were conducted for each prototype test along a traverse parallel to and 1.57 ft from the inside of the north abutment. This was done by measuring the distance from a walkway located above the weir to the water surface using a laser distance measurement tool. The laser was installed at approximately the same elevation as the camera, and measurements were taken at the weir face and at 4 in, 8 in, and 10 in downstream of the weir face. To improve reflection of the laser from the water surface, a thin sheet of plastic was attached to a pole and the pole was held such that the plastic floated on the surface of the water without affecting the water surface elevation. The distance-to-water measurements for each test are given in Table 4.3. For some of the flows there were surface waves that made laser measurements impossible. Data collected during these conditions are not included in the table.

Table 4.3 Distance-To-Water surface measurements

		Distance to water surface from measuring device position			
Test	Gate Opening (ft)	At weir face A (ft)	4" from weir face B (ft)	8" from weir face C (ft)	10" from weir face D (ft)
A1	No Flow				
A2	0.5	6.778			
A3	1.0	6.873	6.926	6.932	7.054
A4	2.0	6.923	6.972	7.037	7.103
A5	4.0	6.932	6.995	7.087	7.152
A6	0.76	6.955	6.988	7.021	7.054
B1	No Flow	6.000	6.000	5.970	6.000
B2	0.5	6.010	6.020	6.030	6.030
B3	1.0	6.090	6.120	6.140	6.145
B4	2.0	6.265	6.340	6.430	6.505
B5	4.0	6.380	6.470	6.580	6.640
B6	1.5	6.420	6.475	6.550	6.605

Figure 4.16 shows a profile of a G304 structure. Figure 4.17 shows a plan view of the structure and its actual orientation with north. The structure was originally constructed in the canal with a flat, horizontal 20ft by 7.5ft section of bed just upstream of the weir. This section is referred to as the apron in Figure 4.17. The apron has an elevation of 9.0 ft-msl. The depths of water in the canal upstream of the weir above the apron (hu) and above the weir at A (h_A) were calculated using equations 4.1 and 4.2 and are given in Table 4.4.

$$h_u = DTW_{HW} - y_u \tag{4.1}$$

$$h_A = DTW_{HW} - y_w - \left(d_{l,A} - d_0\right) \tag{4.2}$$

DTW_{HW} is the head water elevation. y_u, and y_w are the elevations of the apron and the weir crest, which are 9.0 ft-msl and 11.17 ft-msl, respectively. The distances measured by the laser before the tests (with no flow) and during each test are given by d_0 and d_l, respectively. An appropriate subscript is added to differentiate between measurements at A and at U (see Figure 4.16). Equation 4.1 assumes that the drop in the water surface above the apron caused by flow over the weir is negligible, whereas equation 4.2 account for a drop in the surface using the laser measurements. This assumption was acceptable since appreciable drops in the water surface were only observed close to the weir face, and apron measurements were well upstream of the weir as shown in Figure 4.16. The depths given in Table 4.4 by h_u and h_A represent the vertical dimensions of the flow cross section above the apron and at A, respectively. They were used for the depth terms in Equations 4.4 and 4.5 to estimate discharge fluxes at the two cross-sections.

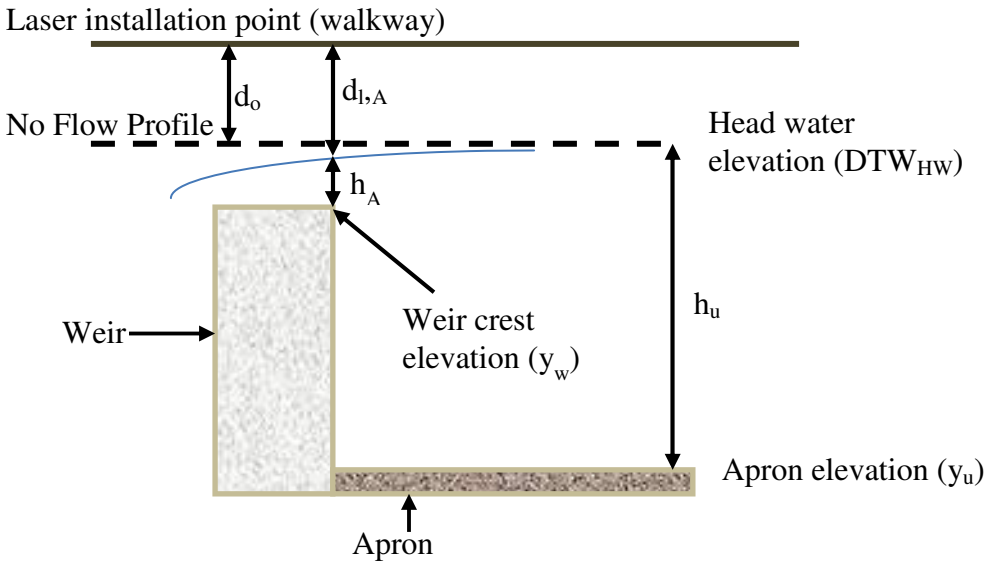

Figure 4.16 Depth of water in canal upstream of weir above apron and above weir face

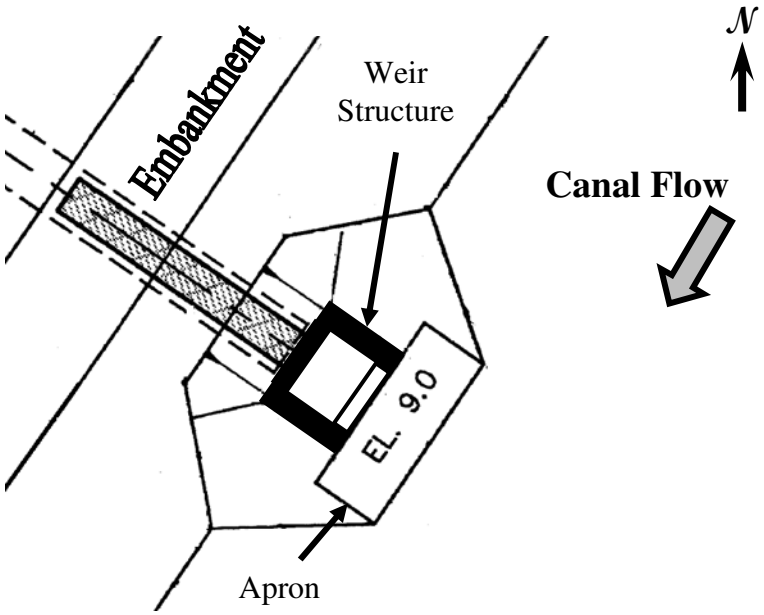

Figure 4.17 Plan view of the G304 weir structure

Table 4.4 Depth of water above the apron and above the weir at locations U and A

Test	DTW_{HW} Before Tests (ft)	DTW_{HW} During Test (ft)	Weir Head, H (ft)	d_0 (ft)	$d_{l,A}$ (ft)	h_u (ft)	h_A (ft)
A2	12.160	12.143	0.973	6.760	6.778	3.143	0.955
A3	12.160	12.115	0.945	6.760	6.873	3.115	0.832
A4	12.160	12.095	0.925	6.760	6.923	3.095	0.762
A5	12.160	12.050	0.880	6.760	6.932	3.050	0.708
A6	12.160	12.015	0.845	6.760	6.955	3.015	0.650
B2	12.900	12.910	1.740	6.000	6.010	3.910	1.730
B3	12.900	12.860	1.690	6.000	6.090	3.860	1.600
B4	12.900	12.810	1.640	6.000	6.265	3.810	1.375
B5	12.900	12.710	1.540	6.000	6.380	3.710	1.160
B6	12.900	12.610	1.440	6.000	6.420	3.610	1.020

4.3 Laboratory Measurements

4.3.1 G304 Model Construction

The laboratory model of the G304 structure was designed and constructed at the hydraulics laboratory of the University of Nebraska by Matthew Clark (graduate student) and Dr. David Admiraal. The objective of their research was to calibrate the constructed model and to characterize flow development and head loss rates in the model culvert, a helical corrugated culvert (Clark 2009). The layout of the model is depicted in Figure 4.18 and Figure 4.19. Few modifications were made to the original model for the purposes of this research, which was to verify LPTV results established in the field for a wider range of flows and in controlled conditions.

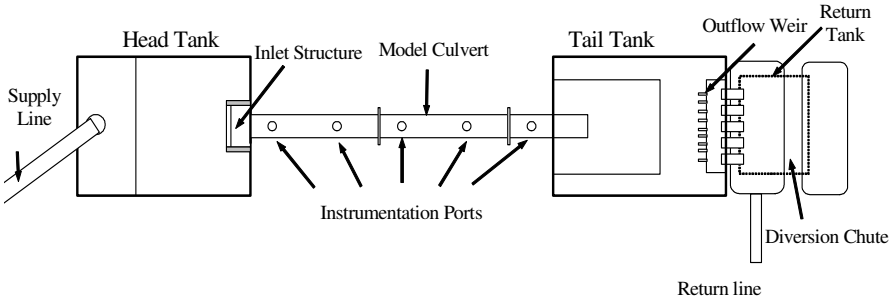

Figure 4.18 Plan view of model layout (Admiraal, D.M. 2009)

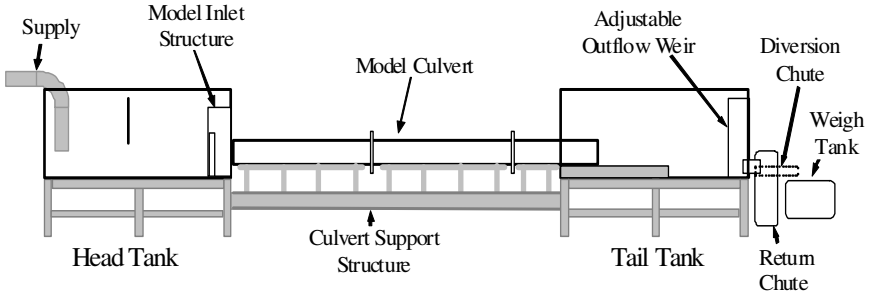

Figure 4.19 Profile view of model layout (Admiraal, D.M. 2009)

The model consisted of a supply pipeline, a head and tail tank, a culvert, a diversion tank, and a weigh tank. The laboratory pump was capable of delivering 3 cfs of flow from the laboratory sump to the head tank of the model, an adequate flow for the purposes of this experiment. A control valve was installed between the pump and the head tank, and it was used to control the discharge into the head tank. The supply pipeline was an 8 inch diameter PVC pipe that vertically entered the head tank. The outlet of the supply pipe was a Tee-shaped diffuser with one-inch holes drilled in it. A plastic panel baffle that spanned the width of the head tank was installed about 1.5 feet downstream of the supply to help break up the flow. The baffle was installed approximately 2.5 feet above the head tank floor so that water flowed under it. For this research, the original baffle was not enough to sufficiently reduce surface turbulence so that the flow patterns of tracer particles would not be influenced, especially for high discharges. To eliminate this problem, a 2 inch thick mesh supported by a PVC frame that spanned the entire width of the head tank was placed about one foot downstream of the supply diffuser. Additional mesh was wrapped around the diffuser to reduce the turbulence induced in the head tank by the diffuser. This greatly improved flow conditions and ensured that inflow turbulence had negligible effect on the state of the flow over the weir.

The model was a 1:6.26 scale model based on Froude number similarity (Clark, 2009). The model G304 inlet structure, consisting of a weir and sluice gate, was installed at the downstream end of the head tank as shown in Figure 4.20. The model sluice gate discharged to the model culvert, which was outside of the head tank (see Figure 4.21).

Figure 4.20 Model inlet weir box

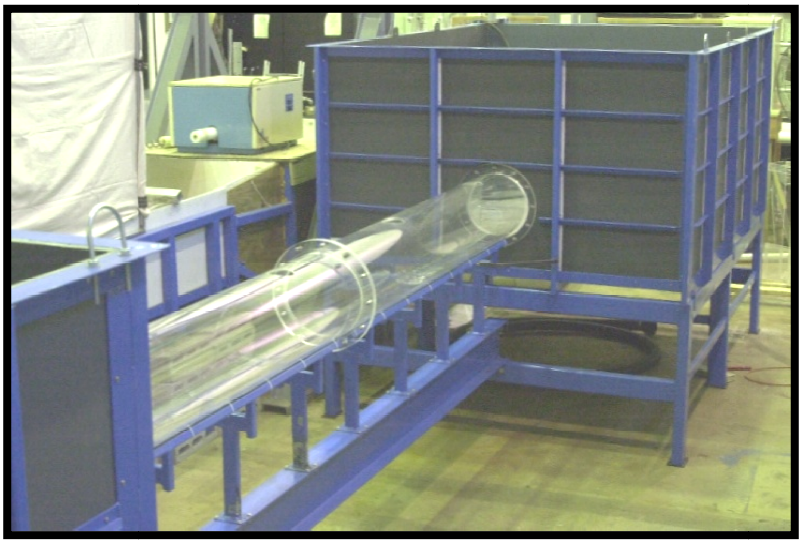

Figure 4.21 Head tank and model culvert

A welded steel frame supported the main structure of the model, and the inside of the head, tail and diversion tanks were lined with plastic panels and sealed for leakage with silicone. The model culvert was approximately 15.5 feet long and had an internal diameter of 11.5 inches. The culvert was constructed of Plexiglas and was supported by an I-beam that spanned the gap between the head tank and the tail tank. The model weir and sluice gate were also made of Plexiglas; the sluice gate could be raised or lowered by rotating a positioning lead screw. For the tests described herein, the gate was always completely open.

A camcorder was installed directly above the model weir on a fully adjustable aluminum frame. The angle and position of the camera could be easily adjusted, and the entire assembly could be repositioned, facilitating easy camcorder installation and removal. The system was designed so that the camcorder could record flow over the top of the weir from directly above it. The vertical orientation of the camera eliminated the need to correct the images for obliqueness.

The model culvert emptied into the tail tank, and at the downstream end of the tail tank was the outlet into a diversion tank. A diversion chute was connected to the diversion tank and was used to divert water into the weigh tank for discharge measurement. The diversion tank and the weigh tank were connected to the laboratory return channel. The return channel carried water to the laboratory sump where it could be pumped back into the flume.

4.3.2 Experimental Procedure

Before running the experiments, the pump was turned on, and the control valve was used to adjust the flow until the water was exactly at the same level as the top of the model G304 weir. The height of the water surface was then measured using a point gauge, representing the weir crest elevation (P). The flow from the pump was then increased to get different head levels in the head tank. Details of each test are provided in Table 4.5. To obtain the desired head elevations, the point gage was set to a predetermined height, and the pump discharge was adjusted until the water level was at the point gauge level. A fifteen-minute delay was allowed to ensure that the flow was steady. The camcorder was mounted into position directly above the weir. An external screen was connected to the camcorder, and the camcorder infrared remote was used to adjust the settings of the camcorder while watching the output display on the external screen. The camcorder settings and the laboratory lighting were adjusted for optimum tracer particle visibility. Light reflections on the water surface were minimized by shading direct reflections.

Table 4.5 Experimental model conditions

Test	*Date*	*Forebay depth upstream of weir (ft)*	*Head above weir crest (ft)*	*Weigh Tank Q (ft^3/s)*	*Water Temperature (^oC)*	*Pixel-Distance Ratio*
1	7/9/2011	0.318	0.07	0.073	20.80	13.35
2	7/9/2011	0.347	0.10	0.116	20.80	13.35
3	7/18/2011	0.395	0.15	0.212	20.80	13.50
4	7/18/2011	0.428	0.18	0.292	20.70	13.50
5	7/19/2011	0.452	0.21	0.395	20.40	14.25
6	7/19/2011	0.477	0.23	0.448	20.70	14.30
7	7/19/2011	0.518	0.27	0.577	20.75	14.70
8	7/19/2011	0.558	0.31	0.705	20.85	14.80
9	8/4/2011	0.598	0.35	0.861	20.80	14.20
10	8/4/2011	0.634	0.39	1.056	20.90	14.40
11	8/4/2011	0.680	0.43	1.176	20.95	14.55

Once steady state was reached, the height of the water above the weir and the temperature of the water were recorded.

4.3.3 Calculation of the Pixel-to-Distance Ratio

For laboratory measurements, a calibration mesh (Figure 4.22) was used to determine pixel-to-distance ratios as shown in Table 4.5. In contrast with the field measurements, for the laboratory measurements the calibration mesh was placed at exactly the same level as the water surface and recorded for about 30 seconds at the start of every test. For model measurements, as the flow rate was increased for each test, the distance from the camera to the water surface decreased because of the increased elevation of the water surface inside the head tank. This resulted in corresponding increases in the pixel-to-distance measurement (see Table 4.5).

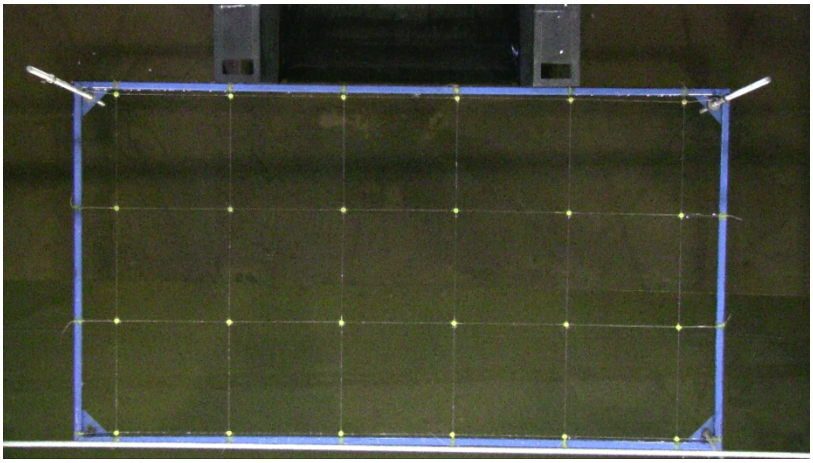

Figure 4.22 Metal framed mesh used for estimating pixel sizes (model tests)

4.3.4 Discharge Measurements

Following calibration of the camera, discharge measurements were conducted and recorded. Discharges were measured using the weigh tank at the outlet of the tail box. The weight of the tank when empty (the initial weight) was recorded. A diversion chute was then engaged and the flow exiting the tail tank was diverted into the weigh tank. The weigh tank was then allowed to fill, and the time it took for the diverted water to fill the weigh tank was measured using a stopwatch. When the weigh tank was full, the final weight of the tank and diverted water was recorded. The discharge was calculated using Equation 3.1. Each discharge measurement was repeated until values of measured discharge were within ±2%; this provided some assurance that the model had reached steady state. The averages of discharge measurements recorded before and after each LPIV test are given in Table 4.5.

Once the discharges were recorded the height of water above the weir and the temperature of the water in the head tank were rechecked and recorded. The camcorder was then set to start recording and tracer particles were evenly scattered over the entire span of the head tank. More particles were added until a recording with a length of about

4 minutes had been captured; each minute of recording produced 1800 frames. A second discharge measurement was taken following the test and was verified in the same way as the initial discharge measurement. Following each test, the discharge was increased and the experiment was repeated.

4.3.5 Model LPTV Measurements

Model experiments were done with the camera viewing the entire weir area. The model test was conducted such that the camera was directly above the area of interest. Unlike for the prototype tests, for the model tests it was not necessary to merge image data because each video recording covered the entire model weir structure. The calibration grid discussed in Section 4.3.3 was used to determine the equivalent size of each pixel. Since the grid was always placed on the surface of the flow before each test, it could be used to determine the scale of the flow surface. For each test, an image of the calibration grid was loaded into the FFCMD analysis program. The grid was used with the program to find the number of pixels per centimeter of water surface. This information was then used by the program to determine velocities after tracer displacements were found.

For the model tests, the imaged areas were large compared to those of the prototype tests, and velocities in different parts of the image were quite different. Consequently, particle displacements were much greater above the weir than well-upstream of the weir. This created problems when processing the images, because in regions with low velocities, particle displacements were not discernible. To rectify the problem, different separation times were used to calculate velocities in different regions of the flow. In other words, in regions of the flow with low velocities, one or more

images were skipped so that tracer displacements would be larger, and the separation time was correspondingly increased. For calculating velocities in regions with high velocities, no images were skipped, and the image separation time was 0.033s. The images from each test were batch processed to get complete velocity vector fields. Velocity vector filtering was conducted on all model tests just as it was on the prototype tests. A typical example of a velocity distribution plot for the model after all filtering processes is shown Figure 4.23.

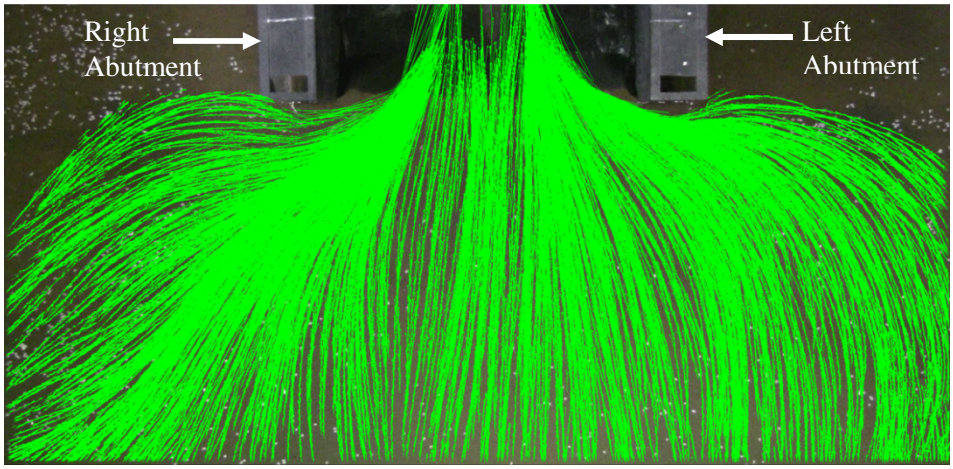

Figure 4.23 Velocity vectors for model Test 10 after filtering

4.4 Field and Laboratory Average Velocity and Discharge Computations

4.4.1 Depth Averaged Velocities

One of the primary objectives of this project was to determine discharges over the G304 weir using LPTV and to compare the results with other forms of measured discharge. The method employed measuring the surface velocity to estimate depth-averaged velocities for each location and then using the depth-averaged velocities to compute the discharge using the equation:

$$Q = \sum U_i A_i \tag{4.4}$$

where Q is the discharge for a cross section, A_i is the cross-sectional area of a subsection of the flow and U_i is the mean velocity normal to the subsection area. Since the velocity in most flows varies with horizontal position and depth, it is a regular practice to measure velocity at several positions along a transect of the channel and to associate each velocity with the sub-area of the flow cross section closest to it.

The mean velocity was calculated by assuming that the velocity distribution below the surface followed a theoretical distribution (e.g., the power law or the logarithmic law). Then, the measured surface velocity was used in conjunction with the theoretical velocity distribution to calculate the mean velocity at each location of the flow. In uniform open-channel flow, the power law and the logarithmic law provide a relatively accurate description of the velocity distribution (Chanson, 1999). Of these two equations, the power law is the easiest to apply and is expressed as (Cengel and Cimbala,2010):

$$\frac{u}{U_{max}} = \left(\frac{y}{H}\right)^{\frac{1}{n}} \tag{4.5}$$

where u is the velocity at the distance y from the bed (measured upwards), U_{max} is the surface velocity, and H is the depth. 1/n is the exponent of the power-law, and is commonly set to 1/7 for open channel flows (Cengel and Cimbala,2010). The logarithmic law is expressed as (Cengel and Cimbala,2010):

$$\frac{u}{u_*} = \frac{1}{k}\ln\left(\frac{30y}{k_s}\right) \tag{4.6}$$

where u_* is the boundary shear velocity, k_s is the Nikrusade equivalent sand roughness and k is the von kármán constant. Because the boundary shear velocity was unknown for

this research, the power-law was most suitable for calculating depth- averaged velocity. By integrating the power law over the depth, the depth-averaged velocity was found to be $7/8^{th}$ of the measured surface velocity. Thus, the surface velocities measured with LPTV could be used to estimate depth-averaged velocities and consequently discharges. Note that the validity of this conversion is dependent on the assumption that the power law is valid, and the literature casts doubt on this assumption in the vicinity of the leading edge of the weir. According to the literature, it seems apparent that the velocity distribution at a weir face is not uniform. Instead, the velocity increases from the free surface downwards and is greatest just above the weir crest. The velocity then decreases from its maximum just above the weir crest to zero at the crest. Hager and Schwalt (1994) conducted a study of the velocity distribution over a broad-crested weir. These results are discussed in Section 2.10. Their work was conducted on a broad-crested weir whose parameters are similar to the G304 weir. The dimensionless profile determined by Hager and Schwalt was integrated over the depth, and the ratio of the surface velocity to the mean velocity was found to be 1.14 (as opposed to 0.875 found using the power law). This factor was applied to the LPTV surface velocity measurements at the weir face to obtain mean velocities at the weir face. It should be noted, however, that the velocity distributions given by Hager and Schwalt are for flow without tail-water, and in the present case, the flow over the weir is in some cases influenced by the gate setting of the weir structure. The gate causes the backwater to back-up behind and above the weir, and thus the velocity profile will likely not follow the power law or Hager and Schwalt's measurements mentioned above.

Average surface velocities were calculated using FFCMD for prototype Transects U and A and for one transect in the model (Transect U): Transect U is approximately two and a half times the head above the weir crest (2.5H) upstream of the weir face, and Transect A is directly above the weir face. These two transects are shown in Figures 4.24 and 4.25. Note that Transect U cuts both vertically and horizontally across the flow; whereas Transect A only cuts horizontally across the flow. The $1/7^{th}$ power law was applied at Transect U to obtain the mean velocity, and the mean velocity was integrated across the cross-sectional area of interest to obtain the discharge. At Transect A, the correction factor from the velocity profile of Hager and Schwalt (1994) was applied to obtain depth-averaged velocities.

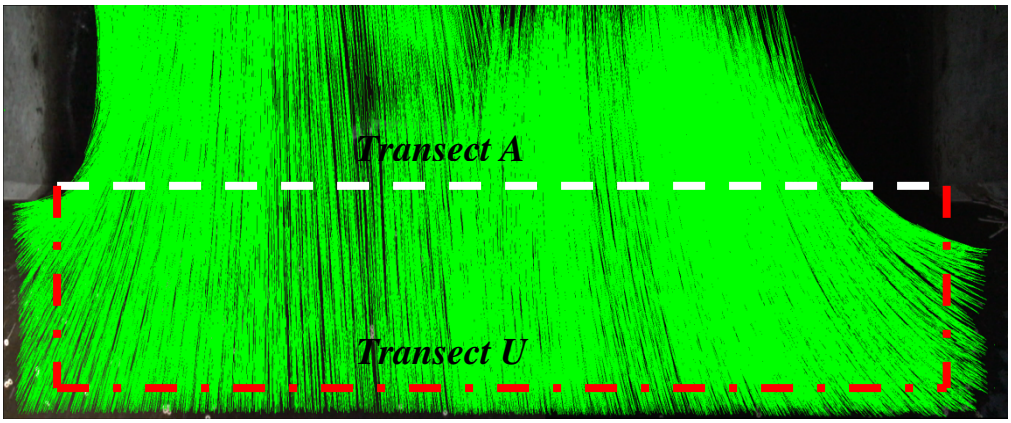

Figure 4.24 Average velocity calculation locations for prototype measurements

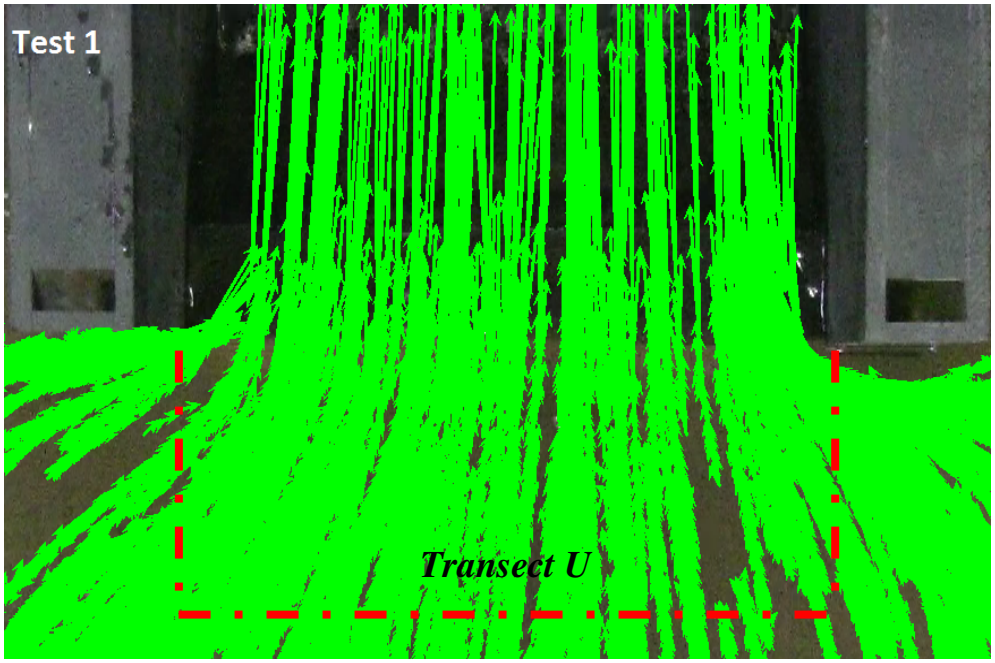

Figure 4.25 Average velocity calculation locations for model measurements

4.4.2 Average Surface Velocity Estimations

LPTV analysis of every consecutive pair of images results in a set of velocity measurements. Each successful tracer particle match yields one velocity vector at the centroid of the match. Since each pair of images may have many tracer particles and there are many pairs of images, the resulting number of velocity vectors can be overwhelming. In many of the tests reported herein, more than 80,000 velocity vectors were available after filtering.

The FFCMD program allows the data to be manipulated to compute spatially averaged surface velocities. In order to find average velocities, all of the velocity vectors must be entered into a large table. The user then defines a grid of points on the image where the average velocities will be determined. Since velocity vectors calculated from PTV are randomly positioned, the analysis program averages all of the

vectors within a specified range of each grid point to determine the velocity at that grid point. The resulting average velocity is then plotted at the grid point.

Figure 4.26 shows the grid cell arrangement for the average surface velocities computed at the weir face of the prototype. The program grid size setting was limited to a minimum of two columns and two rows, so all grids were computed with at least two rows and two columns of grid points. For the discharge measurements only a single transect of velocity measurements is needed, and so the grid cells were arranged so that for horizontal transects, the centerline of one of the two rows of grid points was directly above the required transect. Velocity data from the second row were discarded. Similarly, for vertical transects, only one column of velocity data was retained even though two columns of velocity vectors had to be computed.

To calculate the average surface velocity at the weir face, a grid of forty one columns by two rows was created, starting at the inside face of the left weir abutment and extending to the inside face of the right weir abutment. The resulting grid cells were 50 pixels by 50 pixels in size, and the entire calculation grid was 2050 pixels wide. The actual weir length was 2063 pixels wide, so the 13 pixel difference had to be compensated for in the discharge calculations. The 50 pixel by 50 pixel averaging region is somewhat arbitrary, but is related to the size of a typical PIV interrogation region of 64 pixels by 64 pixels and was based on the order of magnitude of measured velocities in the region of the weir. The prototype weir was 266.97 cm wide, and the size of each averaging area was 6.5 cm by 6.5 cm; whereas the particle displacement between image frames was between 5 and 10 cm for the fastest flows. A smaller averaging cell might not have enough measurements within it to produce a reliable

result, and selecting a larger averaging region would reduce spatial resolution and cause results to be averaged over regions with strong velocity gradients. The program calculated average velocities at the center point of each grid cell by averaging the x and y components of the tracer velocities measured within each cell. Average surface velocities were calculated for grid points along two transects: the transect at the face of the weir, and the transect upstream of the weir as shown in Figures 4.24 and 4.25.

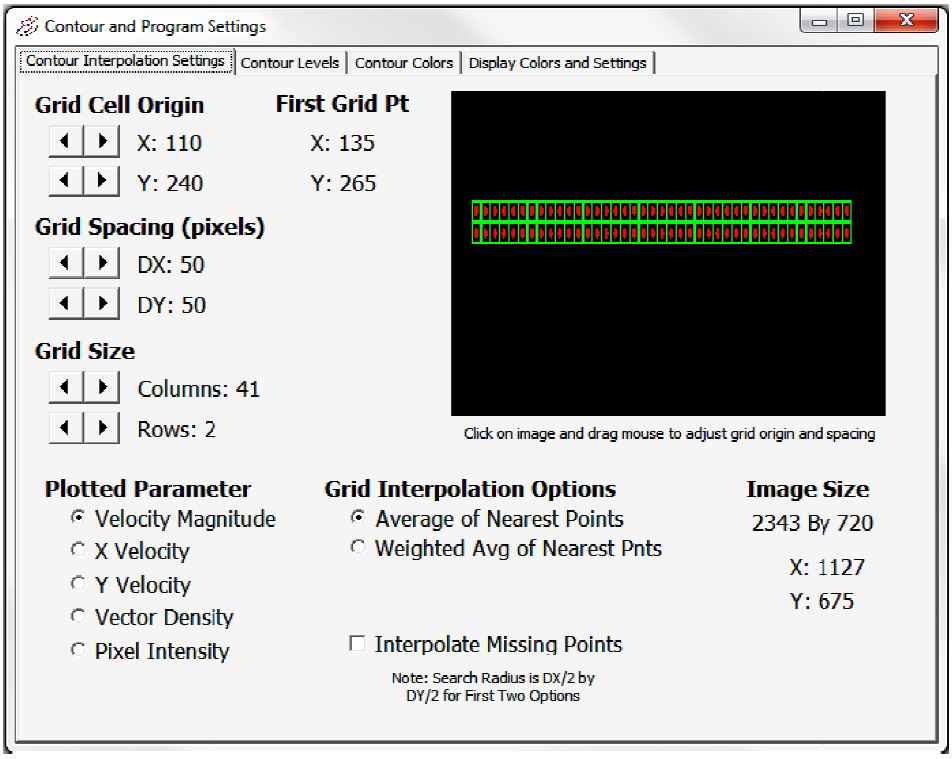

Figure 4.26 Example grid cells at the prototype weir face

A sample of the resulting average velocity distributions for the two transects is shown in Figure 4.27 for Test B5 in the prototype. The light blue vectors are at the weir face, the yellow vectors are for the transect 2.5H, upstream of the weir face, and the white vectors are for flow through the sides of the upstream transect.

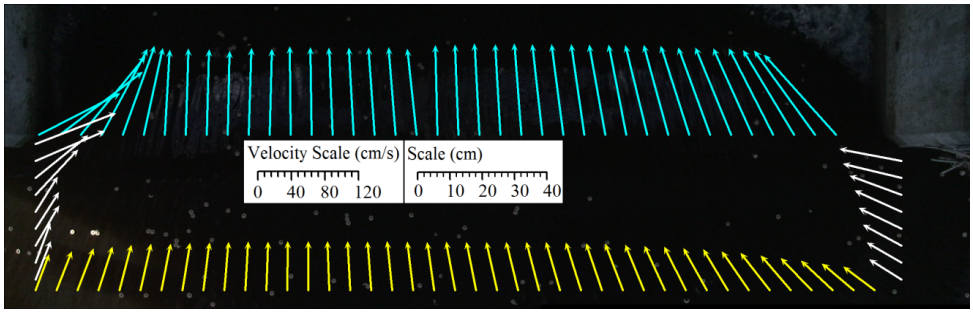

Figure 4.27 Average velocity distributions for field Test B5

Similarly for the model to calculate the average surface velocity at the weir face, a grid of fourteen columns by two rows was created, starting at the inside face of the left weir abutment and extending to the inside face of the right weir abutment. The selected grid cells were 40 pixels by 40 pixels in size.

4.4.3 Discharge Calculations

Discharges were calculated at Transects U and A for both the prototype and the model. The average surface velocity calculations described in the previous section were integrated across the two transects. The discharge calculation based on the power law was:

$$Q = \sum (\frac{7}{8}) B_i H_i V_i \tag{4.7}$$

for the upstream transect, where a uniform flow distribution was assumed. For the flow above the weir, the discharge calculation was based on Hager and Schwalt (1994):

$$Q = \sum 1.14 B_i H_i V_i \tag{4.8}$$

where B_i is the breadth of each grid cell, V_i is the average surface velocity for each grid cell, and H_i is the depth of each grid cell. In the prototype, the elevation of the bed upstream of the weir was constant according to the design plans of the supply canal. In

the model, a platform was installed upstream of the weir to simulate the scaled bed geometry of the prototype supply canal. Thus, the bed elevation upstream of the weir was also uniform for the model. In both cases, depth above the bed was used for H to calculate the discharge upstream of the weir, and depth above the weir was used for H to calculate the discharge at the weir face.

Chapter 5. **Results and Discussion**

5.1 Introduction

Results were obtained using the equipment described in Chapter 3 and the measuring techniques discussed in Chapter 4. The data collected included LPTV velocity measurements, ADV velocity measurements, and ADFM discharge measurements in the prototype and LPTV and weigh tank discharge measurements in the model. The LPTV/PTV data were processed as discussed in Chapter 4 using FFCMD to estimate surface velocities and average surface velocities over the prototype and model weirs. The average velocity measurements were done at Transects U and A as discussed earlier. The depth-averaged velocities at Transect U (at a distance greater than 2.5H upstream of the weir) were estimated by applying the power law to the average surface velocities measured along the transect for both the prototype and the model. Then, the depth-averaged velocities were used to compute discharges over the weir structures using Equation 4.7. A total of 10 LPTV tests were collected on 02/10/2009 (called low head tests) and 02/12/2009 (called high head tests) and 13 LPTV tests were collected in the model. The results of these tests are presented in this chapter. The LPTV discharges calculated for the prototype were compared to simultaneous ADV and ADFM discharge measurements. Discharges measured in the model using LPTV were compared with discharges measured using the weigh tank. The results of each of these processes are presented in the following sections.

5.2 Surface Velocity Measurements using LPTV

The LPTV process discussed in Chapter 4 was applied to determine two-dimensional surface velocity distributions over the prototype and laboratory weir

structures. Velocity vector distribution plots are given in Figures 5.1, 5.2, and 5.3 for the highest low-head flow in the prototype, the highest high-head flow in the prototype, and Test 10 in the model, respectively.

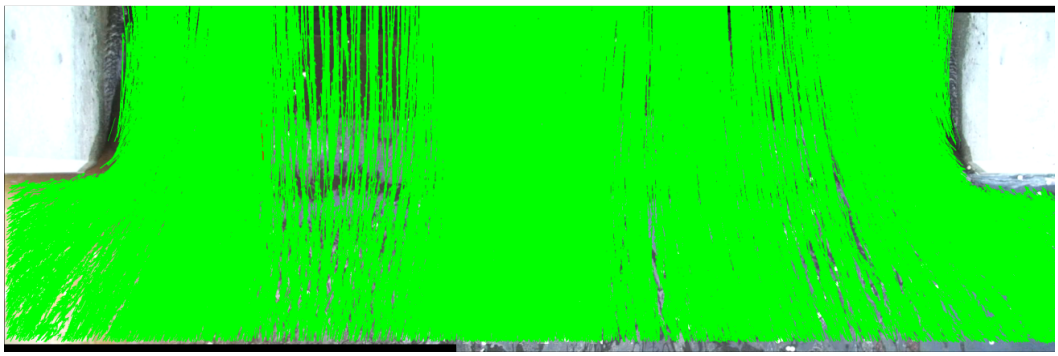

Figure 5.1 Surface velocity distribution (Test A5)

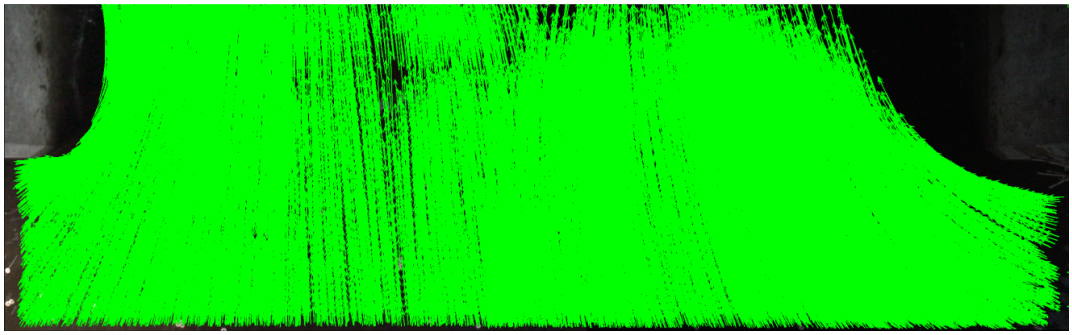

Figure 5.2 Surface velocity distribution (Test B5)

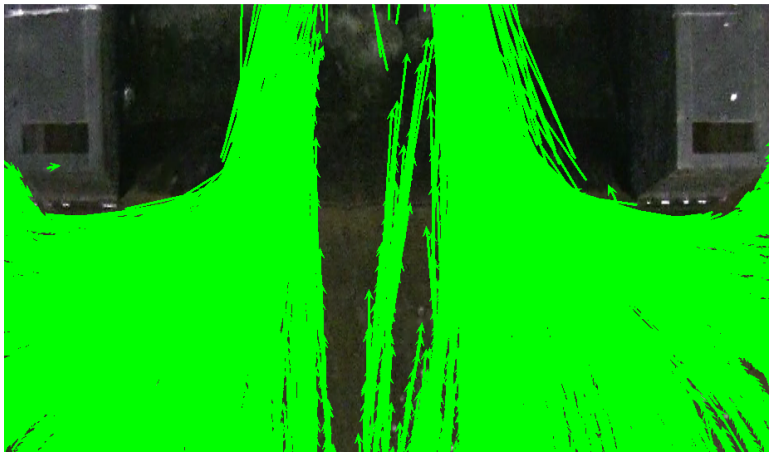

Figure 5.3 Surface velocity distributions (Model Test 8)

Contour plots that correspond to Figures 5.1 through 5.3 are given in Figures 5.4 through 5.6, respectively. The velocity distributions for all of the prototype tests are given in Appendix A, and the distributions for all of the model tests are given in Appendix D. Contour plots of the surface velocity magnitude are given in Appendices B and E for the prototype and model tests, respectively.

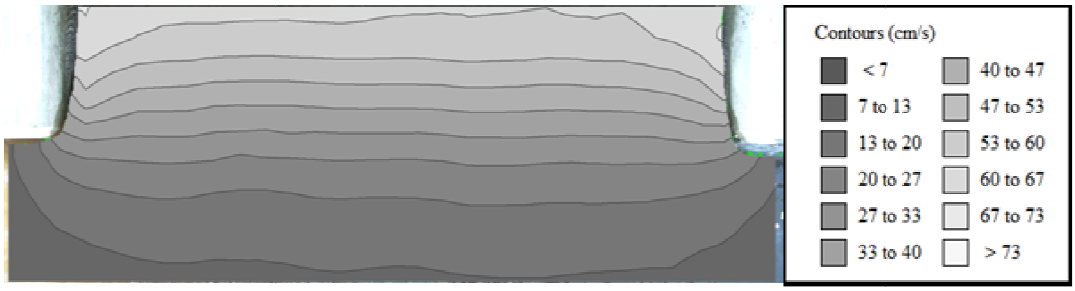

Figure 5.4 velocity contour plot for prototype Test A5

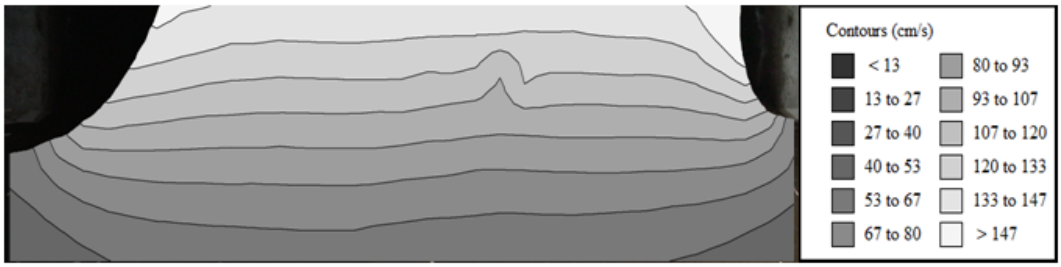

Figure 5.5 Surface velocity contour plot for prototype Test B5.

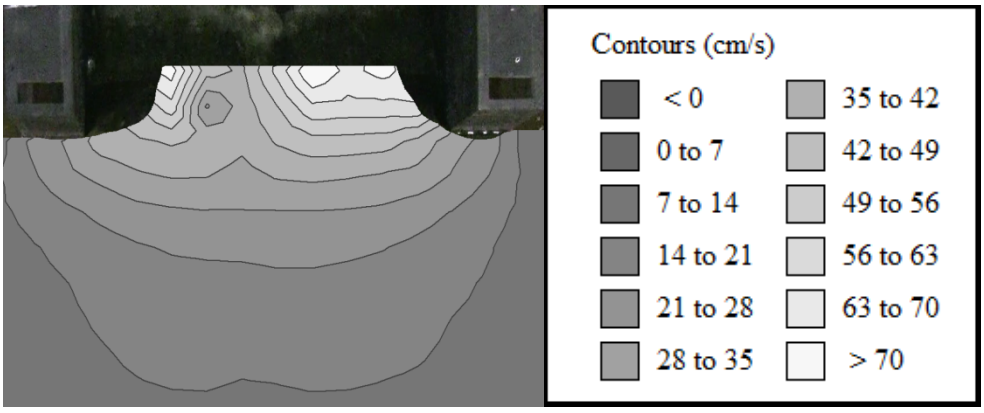

Figure 5.6 Surface velocity contour plot for model Test 8

For all tests, the approach velocities at distances of 2.5H upstream of the weir and beyond are always smallest, and flow is considered to be uniform. The flow rapidly accelerates as it approaches the weir face. For laboratory flows, the flow regime changed from subcritical upstream of the weir to supercritical downstream of the weir, and the flow passed through critical somewhere above the weir. For prototype tests, the transition from sub-critical to super-critical flow could not be defined as well since the gate opening and/or the tail water depth often controlled the flow. The contour plots of the velocity magnitude clearly show tracer particle velocities gradually increasing in the direction of the flow. Baud et al. (2005) found that they could accurately measure discharge over a step using floating tracer particles and a reliable numerical algorithm, but it is quite possible that the measurements presented herein do not produce the correct average velocity of the flow because of assumptions made about the velocity distribution. Upstream of the weir flow acceleration is not nearly so strong. In this region the assumptions made about the velocity distribution are likely to be more accurate, and tracer velocities are also likely to be more accurate because velocity does not change as rapidly with space in this region.

The velocity vector distributions provided in Figure A.1 of Appendix A show that for the low head tests, there is a fairly uniform distribution of vectors across the entire flow region for all tests. On the contrary, for the high head tests (Figure A.2 of Appendix A), the first two tests shown in Figure A.2 show that the flow is moving to the right; whereas for the last three tests, the flow was moving to the left. Three reasons were identified for variations in observed flow patterns: (1) Flow near the edges of the weir is strongly influenced by abutments effects which become much stronger for higher

discharges, (2) canal momentum effects – like all side weirs, flow across the G304 weir is influenced by the primary direction of flow in the canal, and (3) wind effects can have a significant impact on surface velocities.

Comparison of Figures A.1 and A.2 clearly show how abutment effects become more pronounced for higher flows. For the low head, low discharge flows shown in Figure A.1, there is not much separation of the flow from the abutments, but for the high head, higher discharge flows shown in Figure A.2, flow separation near the abutments is significant.

For the present experiments, wind and canal momentum effects both appeared to play a role. In Figure A.2, the measured surface velocity vectors are noticeably angled towards the right abutment for Tests B2 and B3. It is suspected that this shift is due to the wind. For tests with higher discharge (B4 through B6), flow momentum appears to become more important than wind. Regrettably, no local wind speed measurements were collected during these tests because the impact of the wind on the velocity and discharge measurements was unforeseen. The best alternative was to get wind information from the closest weather station, which was Palm Beach International Airport (PBI), 30km away. Wind data from the Weather Underground website (2013) for the times when tests were run are given in Table 5.1 for PBI. A more complete set of wind data for PBI on the days of the experiments are given in Figures 5.7 and 5.8. Based on Figures 5.7 and 5.8, wind speeds were higher on February 10 than on February 12, but winds were less consistent in speed and direction on February 12.

Note from Figures 5.7 and 5.8 that the prevailing wind direction was more easterly on February 10 and more southerly on February 12. The weir face and the canal

were measured using Google Earth to have an orientation of 34 degrees from north as depicted in Figure 5.9, and flow over the weir is perpendicular to the canal axis (~124 degrees from north). Since the winds on February 10 were East South East (~120 degrees), they would push the surface water and the tracers primarily towards the weir, but the winds on February 10 which were more southeasterly (~150 degrees) would push the surface water and the tracers more towards the north weir abutment as was observed in Figure A.2 for Tests B2 and B3.

According to literature presented in Chapter 2, the wind can alter the water surface velocity by 3 percent of the wind speed in the direction of the wind. Table 5.1 shows possible wind drift values based on the PBI wind measurements to provide an idea of the potential influence of the wind on the measured surface velocities. It is difficult to assess what the effect of the wind on the discharge in the culvert is for the current measurements, especially within the confined space of the weir structure, but the fact that estimated free surface wind drift speeds are similar in magnitude to some of the velocity measurements certainly casts some uncertainty on the velocity profile assumptions.

Table 5.1 Wind speed and direction for the prototype tests

Test	Wind speed(mph)	Wind speed(cm/s)	Wind drift Speed(cm/s)	Wind direction
A2	17.3	773.31	23.20	ESE
A3	17.3	773.31	23.20	ESE
A4	16.1	719.67	21.59	SE
A5	16.1	719.67	21.59	SE
A6	16.1	719.67	21.59	SE
B2	3.5	156.45	4.69	WNW
B3	12.7	567.69	17.03	SE
B4	12.7	567.69	17.03	SE
B5	11.5	514.05	15.42	SSE
B6	9.2	411.24	12.34	SSE

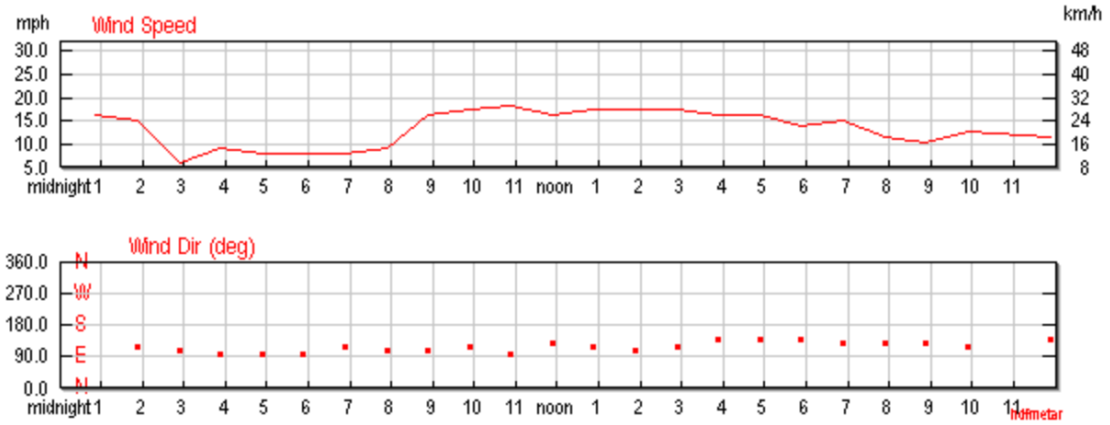

Figure 5.7 Wind speed and direction on February 10, 2009 at PBI (after Weather Underground, 2013

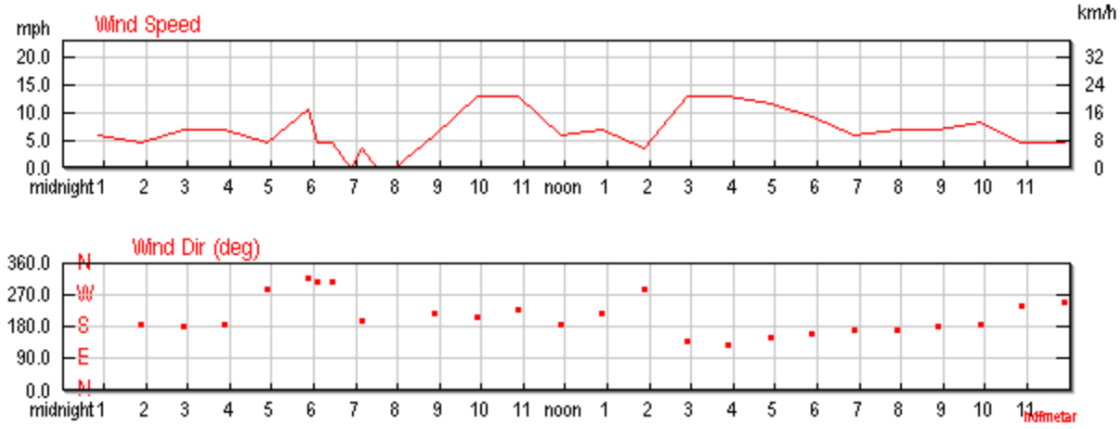

Figure 5.8 Wind speed and direction on February 12, 2009 at PBI (after Weather Underground, 2013)

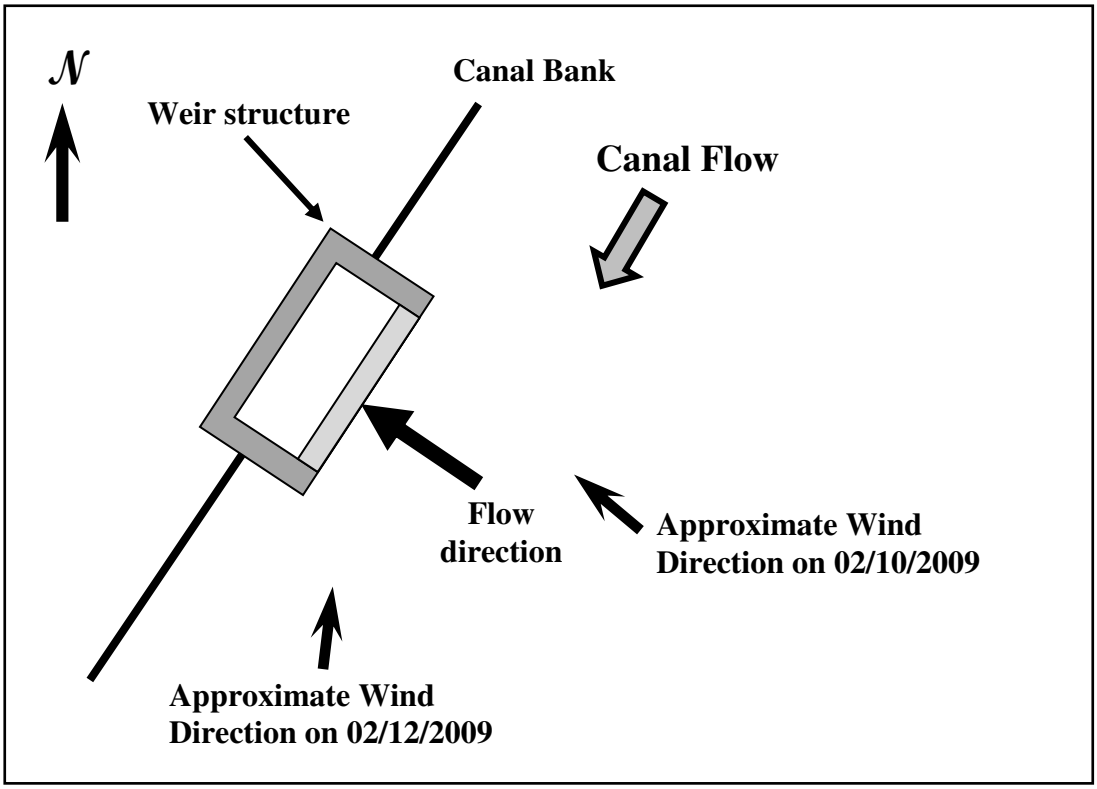

Figure 5.9 Orientation of canal, weir structure and wind-direction (at the time of testing) with respect to north axis

Canal momentum effects also appear to influence flow over the weir for Tests B4 through B6 in Figure A.2. In tests B4 through B6, it is apparent that the flow separates from both the north and the south abutments, and that the separation is greater on the north side than on the south side of the weir – this is opposite of the separation effect that the wind appears to cause. All of the flow in the canal comes from the north, and it is thought that the preferential momentum of the flow causes more flow to pass over the south side of the weir, just as it would for a traditional side weir. This behavior may influence the accuracy of discharge estimates in cases where the velocity in the canal is high. Additional testing would be necessary to determine the impact of the flow momentum on discharge distribution.

5.3 Average Surface Velocity

The average surface velocity is the spatial average of all surface velocity vectors within a selected distance of the averaging point. Average surface velocity distributions were calculated as described in Chapter 4. The average velocity distributions for Transects U and A for the prototype tests are shown in Figures C1 and C2 in Appendix C, and the average velocity distributions for Transects U and A for the model tests are shown in Figure F1 of Appendix F. Average velocity plots for the model and prototype in Appendix C and F show fairly uniform velocity distributions across the weir length in most cases with slightly larger velocities towards the midsection and reduced velocities at the abutments. The directions of the vectors are clearly affected by the abutments, and in the case of the prototype, by wind and channel currents. In the model, average velocity measurements at the weir face were not as reliable as in the prototype. Strong curvature of the water surface at the weir face in the model caused issues with light reflections, especially for high discharges. Furthermore, it was more difficult to track particles near the weir face in the model because of the scale of the weir and the speed of the tracer particles over the weir (a higher frame rate for the video camera would have improved results substantially, but in these tests the camera frame rate was limited to 30 frames per second).

5.4 Measured Discharges

Average velocities were used to compute discharges at Transects U and A. Only the components of the velocity that were perpendicular to the transect were used to calculate fluxes across the transect compute the discharge. For example, along Transect A, only the y-components of the velocity vectors were used in discharge calculations (these are

represented by the sky-blue velocity vector in Figure 4.27). For Transect U the y-components of the velocity vectors a distance 2.5H upstream of the weir (represented by the yellow velocity vectors in Figure 4.27) and the x-components of the velocity vectors of the flow from the sides of the weir (measured from the face of the abutment to a distance 2.5H upstream and represented by the white velocity vectors in Figure 4.27) were used in discharge calculations.

5.4.1 Field Discharge

One goal of this research was to determine if discharge over the weir structure could be accurately measured using LPTV. The explanation of prototype discharge measurements is given in Chapter 4. Discharges measured in the prototype using LPTV, the ADV array, and the ADFM are presented in Table 5.2. The discharges measured using LPTV upstream of the weir (at U) and above the weir face (at A) are also compared to the discharges measured using ADFM and ADV devices in Figure 5.10 and Figure 5.11, respectively.

Table 5.2 Prototype estimated discharges

Test	Gate Opening (ft)	Canal depth upstream of weir (ft)	Depth above weir (ft)	LPTV Q at Transect A (cfs)	LPTV Q at Transect U (cfs)	ADFM Q (cfs)	ADV Q (cfs)
A2	**0.5**	**3.14**	**0.95**	**5.65**	**10.90**	**9.00**	**10.80**
A3	**1.0**	**3.12**	**0.78**	**9.43**	**20.29**	**22.70**	**22.10**
A4	**2.0**	**3.10**	**0.86**	**9.23**	**20.51**	**22.50**	**22.70**
A5	**4.0**	**3.05**	**0.81**	**9.02**	**20.13**	**21.20**	**21.30**
A6	**0.75**	**3.03**	**0.80**	**7.48**	**16.17**	**16.90**	**16.60**
B2	**0.5**	**3.91**	**1.73**	**25.81**	**17.57**	**13.30**	**14.40**
B3	**1.0**	**3.86**	**1.64**	**31.28**	**34.30**	**31.70**	**29.80**
B4	**2.0**	**3.81**	**1.31**	**46.93**	**59.40**	**56.50**	**53.50**
B5	**4.0**	**3.71**	**1.46**	**44.18**	**58.30**	**56.10**	**52.10**
B6	**1.5**	**3.61**	**1.35**	**36.38**	**42.84**	**45.30**	**41.70**

Clearly, discharges measured with LPTV upstream of the weir are in better agreement with ADV and ADFM measurements than discharges at the weir face. The assumption made about the velocity distribution above the weir face appears to be incorrect, at least for some of the flows. There are multiple reasons that the assumed velocity distribution could be wrong: (1) The velocity distributions provided by Hager and Schwalt (1994) are for flow over a broad-crested weir with no downstream effects, but some of the present prototype tests are controlled by a downstream gate and tail water, (2) for some tests, wind affects the span-wise velocity distribution over the weir, (3) for some tests, flow in the supply canal affects the span-wise velocity distribution over the weir, and (4) the confined nature of the water inside the weir box (downstream of the weir and upstream of the gate) create flow dynamics that may affect the velocity distribution. Assumptions about the velocity distribution are likely the primary reason that LPTV does not perform well for discharge calculations above the weir. As an alternative to assuming that the velocity distribution above the weir is fully developed,

using a numerical model, to model the flow over the weir in conjunction with the particle tracking velocity data that were provided with this study would likely provide improvement in the resulting measurements.

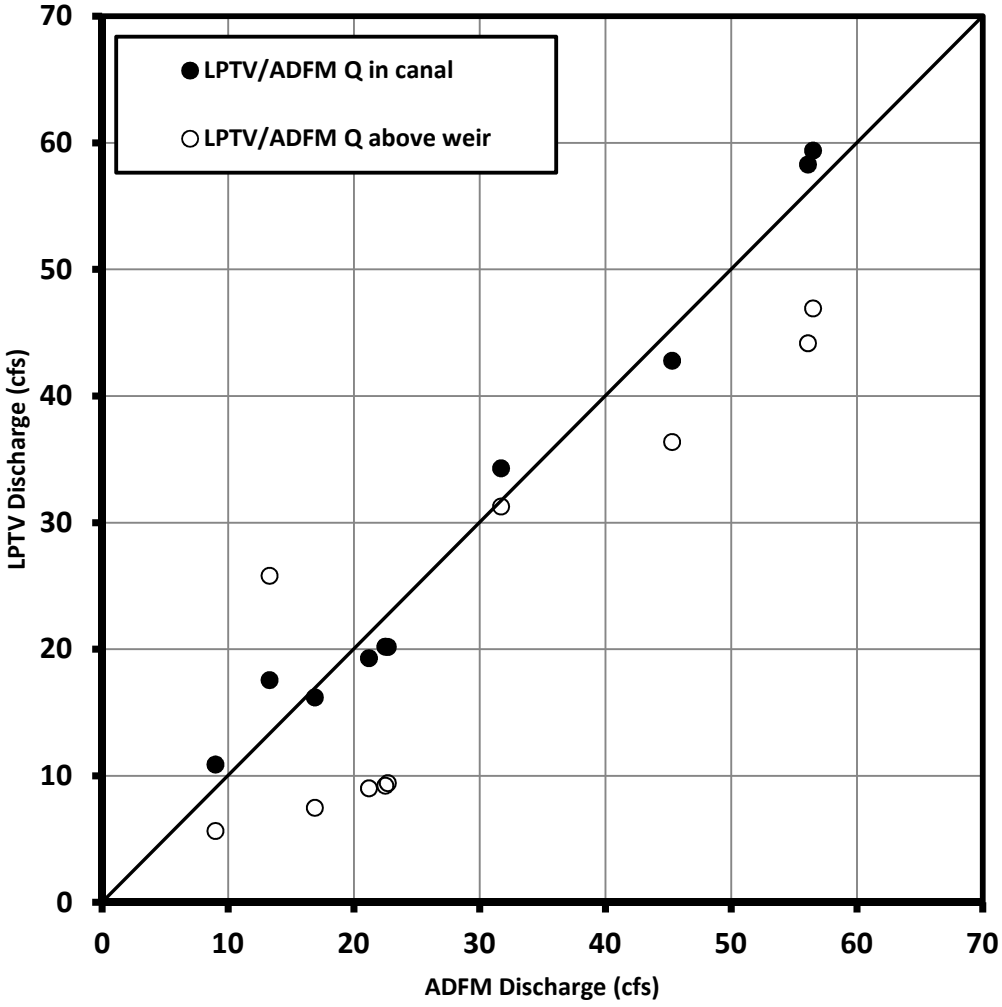

Figure 5.10 Comparison of LPTV Discharges measured above the weir and upstream of weir with ADFM discharges measured inside the culvert

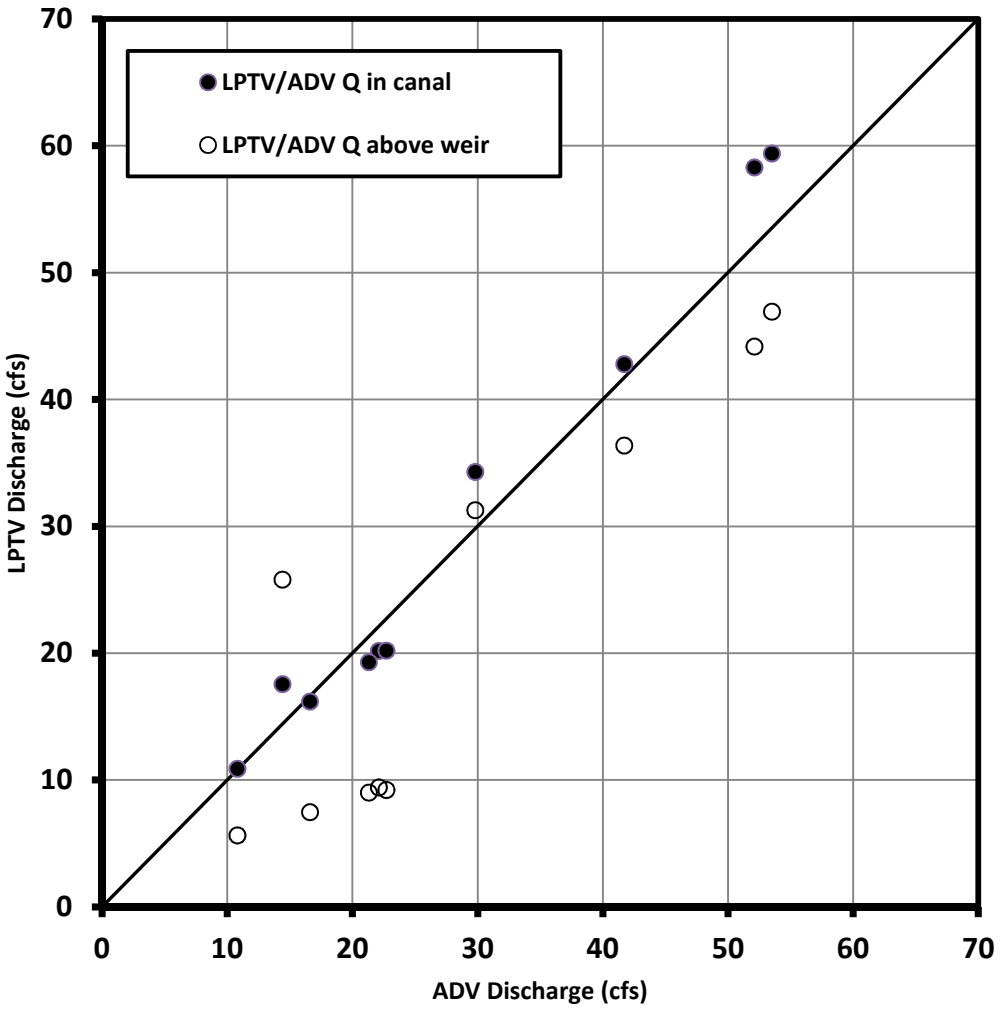

Figure 5.11 Comparison of LPTV discharges measured above the weir and upstream of weir with ADV discharges measured inside the culvert

In addition to assumptions about the velocity distribution, two other possible reasons for a discrepancy between the LPTV and acoustically measured discharges should be considered. First, there is the potential for persistent eddies to form at the water surface of the flow over the weir. The upwelling of water that comes from the bed of the canal can create preferential flow lines for particles floating on the surface; this phenomenon was observed in some cases in the model. The preferential flow lines of the tracer particles can have a different velocity than the cross-sectional average surface velocity.

Second, the pixel-to-distance ratio could have been more accurately measured. Although changes of the pixel to distance ratio associated with changes in water depth can be compensated for, it would have been optimal to measure the pixel to distance ratio at the time of each test.

5.4.2 Laboratory Discharge Measurements

The laboratory scale model experiments were conducted with the gate fully open and with no tail water for all discharges. The main purpose of the laboratory work was to assess the accuracy of using particle tracking velocimetry for discharge measurements in a more controlled environment. In the model, LPTV was only used to measure discharges at the transect that was upstream of the weir (unlike for the prototype tests). Discharge measurements made using LPTV and a weigh tank at the culvert outlet are given in Table 5.3 and Figure 5.12.

Table 5.3 Model discharge measurements

Test	Canal depth upstream of weir (ft)	PTV Q at Transect U (cfs)	Weigh Tank Q (cfs)
1	0.32	0.072	0.073
2	0.35	0.110	0.114
3	0.40	0.196	0.212
4	0.49	0.301	0.292
5	0.45	0.390	0.395
6	0.48	0.428	0.441
7	0.52	0.572	0.577
8	0.56	0.700	0.705
9	0.60	0.849	0.861
10	0.63	0.988	1.056
11	0.68	1.086	1.177

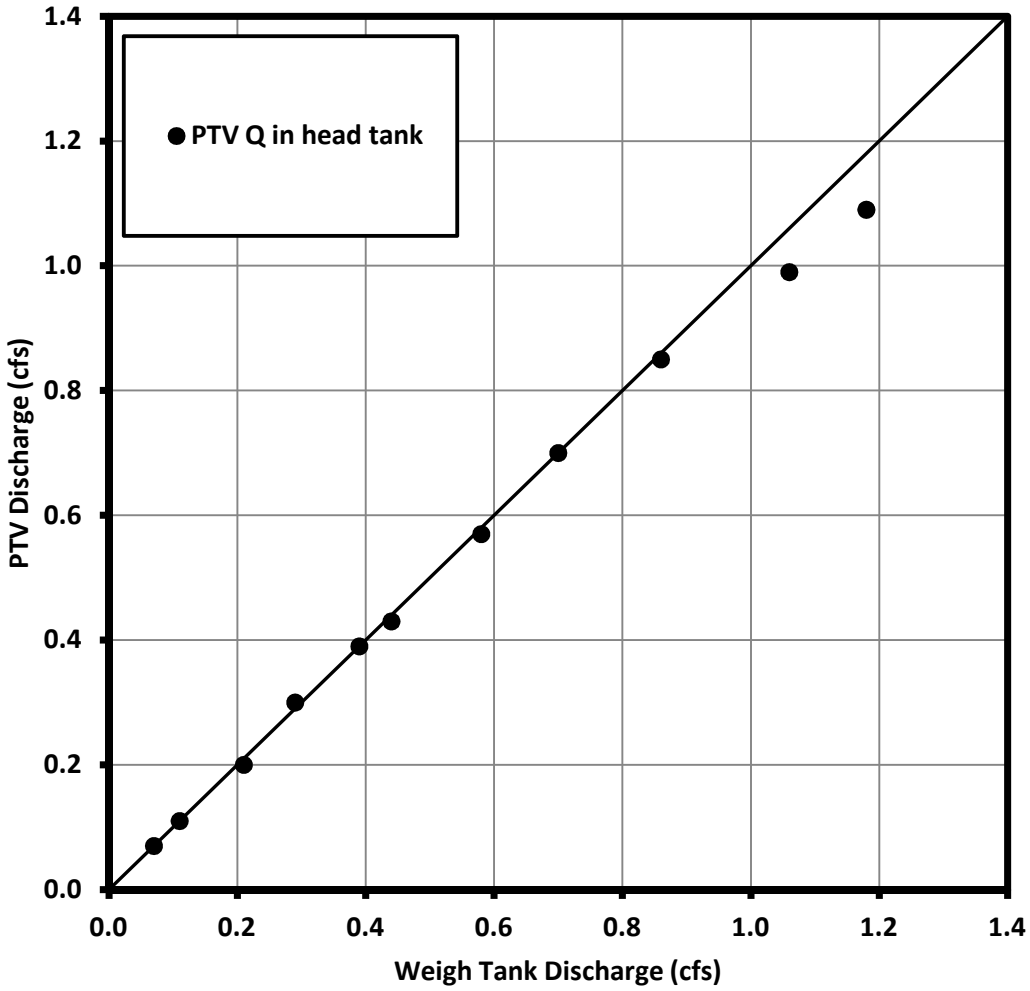

Figure 5.12 Comparison of PTV discharges measured above the weir and upstream of weir with discharges measured using a weigh tank at the culvert outlet

Figure 5.12 shows that the discharges measured with PTV and the weigh tank are in close agreement when the PTV measurements are collected upstream of the weir. There does, however, appear to be a slight bias in the data. This bias might be because the assumption about the velocity distribution is incorrect, but it could also be caused by the way in which the LPTV system or weigh tank are calibrated and used. For the last two tests in the model, the weigh tank measurement yields a higher discharge than the

PTV measurement. This may be related to an observation by Rajaratnam and Muralidhar (1971) who noted that the length (L_e) of a standing eddy in the vicinity of the weir was directly influenced by the approach head. The ratio of L_e/P consistently increased with increasing H/P. As a result, the standing wave eddy increased in size with increasing head, influencing the velocity distribution in the water column. During the laboratory tests, water bubbles rising to the surface became more noticeable with increasing head and this may have been due to the increase in the size of the eddy. It should be noted that such an eddy may be an effect of the model scale and it is quite possible that a standing eddy upstream of the weir will not behave the same way in the prototype as in the model.

5.5 Prototype Abutment Effects

Abutment effects on the discharge over the G304 structure were studied by estimating the discharge across eight equal cross-sectional areas as show in Figure 5.13.

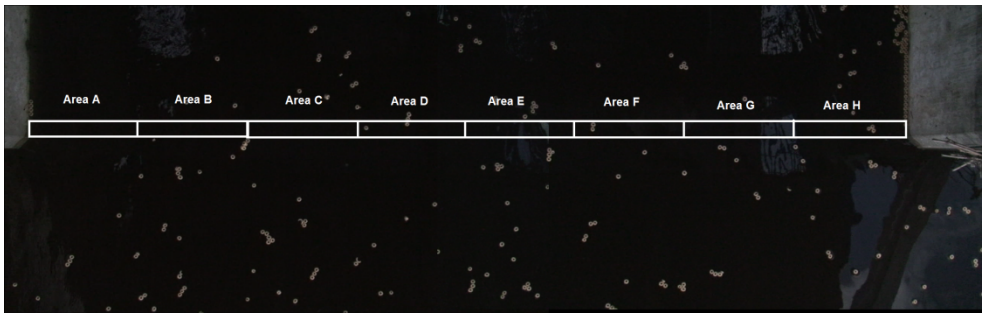

Figure 5.13 Discharge measurements across eight equal cross-sectional areas

The average velocities used to estimate span-wise flow rate distributions were the discharges measured at the weir face. These velocities were not accurate for calculating total flow rate because of uncertainty about the true vertical velocity distribution above the weir. However, as long as vertical velocity distributions at different parts of the weir

can be treated as vertically self-similar (that is, velocity distributions at different locations above the weir have the same shape), the average surface velocity measurements will still provide an accurate representation of the span-wise distribution of the flow, even if the conversion factor for surface velocity to depth-averaged velocity is not accurately known. Results are presented as percentages of the total flow for each test and are given in Table 5.4. Figure 5.14 and Figure 5.14 show the percentage of discharge carried by each sub–section of the weir for the various tests.

Table 5.4 Percentages of total flow over the weir across four equal cross sections

Test	Area A (% of total flow)	Area B (% of total flow)	Area C (% of total flow)	Area D (% of total flow)	Area E (% of total flow)	Area F (% of total flow)	Area G (% of total flow)	Area H (% of total flow)
A2	14.20	13.20	13.10	12.95	13.16	12.49	11.27	9.63
A3	12.05	12.20	12.46	12.42	12.51	12.76	12.85	12.73
A4	11.26	13.27	13.27	11.67	13.55	11.97	12.74	12.06
A5	11.86	12.71	12.52	12.57	12.63	12.94	12.67	12.10
A6	12.29	12.69	11.07	13.24	13.05	12.03	12.73	12.90
B2	5.25	6.01	6.57	8.08	14.24	17.55	18.11	24.18
B3	11.30	11.86	12.94	13.71	14.37	14.60	14.33	6.90
B4	10.91	12.38	12.67	12.76	13.26	13.09	12.71	12.25
B5	10.97	12.89	12.82	12.86	13.29	13.19	12.38	11.59
B6	12.97	13.29	12.99	12.81	12.82	12.35	12.23	10.55

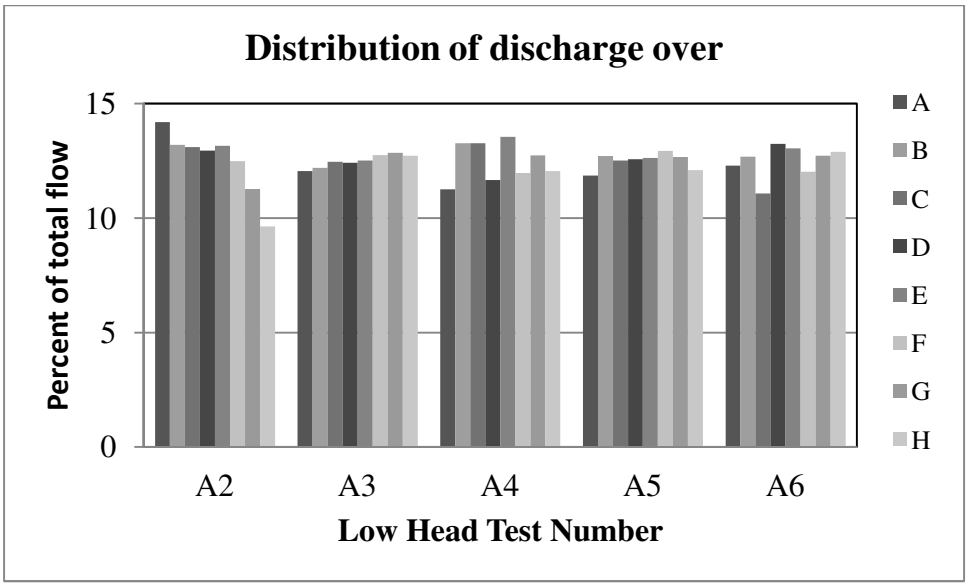

Figure 5.14 Distribution of discharge over weir for low head tests

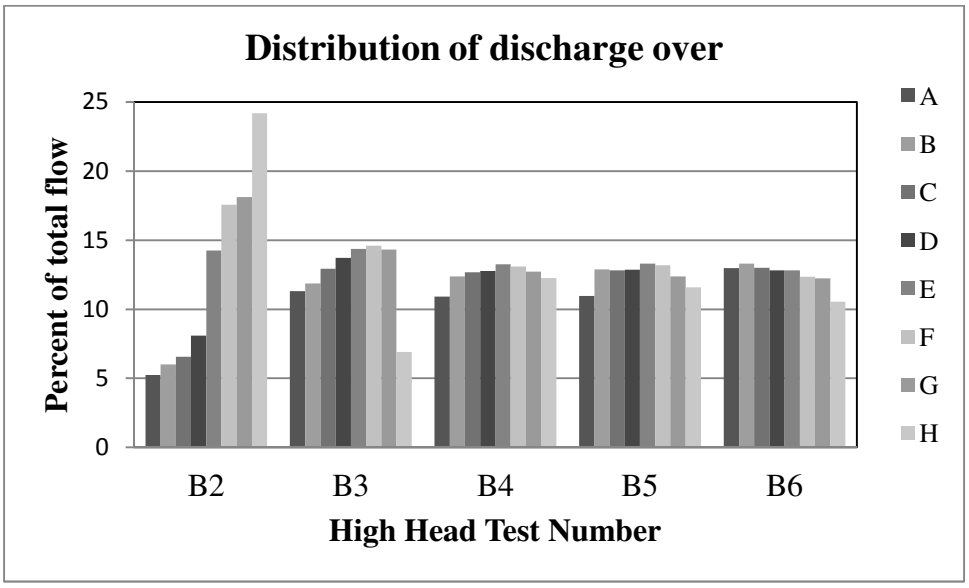

Figure 5.15 Distribution of discharge over weir for high head tests

The above results indicate that the discharge over the weir was significantly influenced by the wind, by the abutments and by the gate opening, especially for the high head drop tests. Except for the lowest gate setting for the low head tests, the discharge appears to have been evenly distributed across the weir. Abutment effects

were not strong for the low head tests, but for the lowest gate setting, flow rates were highest near the left abutment. This distribution could have been because of either geometry effects or wind effects. For high gate openings (except for Test B2 and B3), the majority of the flow was concentrated at the center of the weir, and the effective length of the weir was approximately equally reduced on both ends. For Tests B2 and B3 it appears that the wind had a greater impact than geometry and momentum.

The high head tests (Figure 5.15) show results that are similar to the results of the low head tests when the gate was fully open (4.0 ft) or almost fully open (2.0 ft) and the discharges were high; whereas for the two lowest gate openings, there was an exaggeration of the flow towards the right abutment. It is suspected that this effect was due to wind action and not a characteristic of the structure, itself. Figure A.2 illustrates how the wind affects surface velocities for the lowest gate opening (0.5 ft) and for the high head flows. Table 5.1 presented wind speed and direction recorded at the weather station as discussed earlier. The estimated wind drift for these prototype tests ranged from 12.3 cm/s to 23.2 cm/s; these values are significant compared to the average surface velocity values computed for the tests.

Chapter 6. **Conclusions**

6.1 Overview

In this thesis, prototype and model flow measurements were gathered to study flow over a weir that is part of a gated circular culvert system, the G304 structure of SFWMD. The data were collected and studied to examine how discharge and velocity can be measured in the system for a wide range of flow conditions and to better understand hydraulic behavior of the structure.

The first goal of this thesis was to measure discharge using particle tracking velocimetry and to compare results to discharge measurements using ADVs, an ADFM, and a weigh tank. A second goal was to understand approach velocity and study abutment effects for a range of flow conditions. In addition, a laboratory model was used to access the accuracy of using particle-tracking velocimetry to measure discharge over the G304 weir structure.

A literature review was provided to help understand various flow conditions over this type of structure. Furthermore, PTV analysis software was improved in parallel with this project to obtain better results from PTV images collected during field measurements, which are inherently noisy. The PTV software was written and revised by Dr. David Admiraal with some of the revisions stemming from discussion about improved processing techniques with the author of the thesis.

6.2 General Observations

Several conclusions can be made from comparisons between measured prototype discharges and the plots that compare discharge measurements collected with LPTV to ADFM and ADV measurements inside the culvert (Figures 5.10 and 5.11).

Discharges measured with the ADV array and with the ADFM were in agreement with each other and were within 10% for all but the lowest discharge. For all tests, the LPTV discharges measured upstream of the weir were in close agreement with the discharges measured using ADFM and ADV devices, but for higher head tests the differences between LPTV discharges and the other measurements were greater except for in Test B.6. Differences in wind conditions between the two days that the data were collected may have played a role. For lower discharge measurements, it is quite possible that wind speed and direction influenced the floating particles, however as the discharge increased, flow momentum effects likely dominated over effects of the wind in the vicinity of the weir.

For the prototype tests with higher heads, LPTV discharge measurements at the upstream transect were biased high when compared to corresponding ADFM and ADV measurements. There are two possible explanations for this: (a) from observation of plots of the surface velocity distribution over the weir region of interest for the higher head tests and from the field report data it can be concluded that the wind had a significant impact on surface velocities, (b) for higher weir flows the flow in the canal and the profile of the water surface across the weir likely had a more significant influence on local velocity distributions than for low head tests. Note that the data in Table 5.2 for high head tests show a clear difference not only between LPTV and acoustic discharge measurements, but also between the ADFM and ADV measurements. The ADV discharge measurements are lower except for the test with the lowest discharge. In other words, differences between the discharges measured with LPTV and

the two acoustic methods are not unlike differences between the discharges measured with the two acoustic methods.

When discharge was measured above the weir with LPTV, discharge measurements were lower than the discharges measured with the ADVs and the ADFM for all tests except for Test B2. Based on reviewed literature, the bias can at least in part be attributed to the vertical velocity distribution directly above the weir, which could not be directly measured in these experiments. There is also a possibility that the floating LPTV particles align themselves with low velocity regions of the flow. Such alignment was observed during model tests, but was not readily apparent from the more even distributions of particles observed in the prototype measurements. Discharges measured by applying particle tracking directly above the weir resulted in very low discharge estimates, especially for the lower head tests (for which the differences between LPTV- and ADFM-based discharge measurements were about 50%). It does appear, however, that particle tracking velocimetry can be safely applied to measure velocity and discharge well-upstream of the structure where velocity distributions can be treated as uniform.

Observation of the span-wise distribution of discharge over the weir structure showed that the abutments have a significant effect on the flow over the G304 structure. For the lowest flow rate (smallest gate opening) of the low head tests, flow was biased to the left side of the weir, and the right abutment caused a greater percent reduction in overall flow than in other tests. This was as result of the wind and flow momentum effects discussed earlier. For the higher head tests, the lowest flow rates also showed the strongest difference between the discharges measured on the two sides of the weir, but

in the case of the higher prototype heads, the higher flow rates were biased towards the right side of the weir. The side of the weir that the flow was concentrated on appeared to vary from test to test, but with increasing gate opening and discharge the two abutments tended towards having approximately the same effect on flow reduction, with most of the flow concentrated at the center of the flow region. Wind and other external effects appear to have greater impact for low discharges. When discharges increased, the head gradient across the weir appeared to dominate.

From the laboratory results it can be concluded that LPTV gives a good estimate of discharge over the weir structure compared to other accurate means of measurement, especially when discharge is measured well-upstream of the weir, where velocity distributions approach uniform. However, it was also apparent that as discharge increased to the highest levels that were tested, discharges measured with LPTV began to diverge from discharges measured with the weigh tank. Either surface turbulence began to interfere with the LPTV measurements, or the water surface profile became too steep, invalidating the assumption of a uniform velocity profile, and possibly having an impact on pixel-to-distance ratio assumptions.

6.3 Future Work

The results of this research show that there are several changes that can be made to the experiments to improve the results of future research and to better understand the nature of the flow through the G304 structure. To extend the results of this research the following things can be examined:

- The LPTV procedure at the prototype structure could be repeated, but with an improved calibration method for determining the pixel to distance

ratio. Preferably, the new calibration method would utilize a grid similar to the one used to calibrate each laboratory model test.

- A better surveying method could be used to measure height of water above the weir crest. The new method should improve estimates of the discharge over the weir face. Furthermore, study of the velocity profile over the weir would provide a better understanding of discrepancies between LPTV and acoustic discharge measurements. Ideally, such a study would provide measurements of both surface velocity and vertical velocity distribution.
- In future LPTV studies of low-velocity surface flows, it seems imperative that wind speed and direction be measured in the vicinity of prototype structures. Methods of applying corrections based on wind effects should also be explored.

References

Ackers, P. (1978). Weirs and flumes for flow measurement. Wiley, Chichester; New York.

Admiraal, D. M. (2012). “Weir, Sluice Gate, and Culvert Literature Related to G304/G306 Control Structures: A Literature Review Prepared for the Operations and Hydro Data Management Division of the South Florida Water Management District.”

Admiraal, D. M., and Clark, M. (2009). "Design, construction, and calibration of G304 physical model with velocity and head loss measurements." South Florida Water Management District Report.

Admiraal, D. M. (2012). "Flow Field Captor Muliti-Dimensional PIV/PTV program (Help Files)." .

Adrian, R. J. (2005). "Twenty years of particle image velocimetry." *Experiments in Fluids,* 39 159-169.

Adrian, R. J. (1981). "Particle-Imaging Techniques for Experimental Fluid Mechanics." *Annual Review of Fluid Mech.,* (23), 261-304.

Bagheri, S., and Heidarpour, M. (2011). "Characteristics of flow over rectangular sharp-crested side weirs." *J.Irrig.& Drain.Engrg.,* 138(6), 541-547.

Baines, W.D. and D.J. Knapp (1965): "Wind driven water currents",*J. Hydraulics Division, ASCE* 91, 205-221.

Baud, O., Hager, W., and Minor, H. (2005). ”Toward Nonintrusive Flood Discharge Measurement.” *J. Hydraul. Eng.*, 131(12), 1031–1035.

Borghei, S. M., Jalili, M. R., and Ghodsian, M. (1999). "Discharge co-efficient for sharp crested weir subcritical flow." *J. Hydr. Engrg.,* 1250(10), 1051-1056.

Bureau of Reclamation. (1997). Water measurement manual. The Bureau of Reclamation, Denver, Colorado.

Castex,L.,(1969). “Quelques nouventes sur les deservoirs pour la mesure de debits”*,,La Houille Blanche*,No.5,541-548.

Cengel, Y. A., Cimbala.,J.M. (2010). Fluid Mechanics Fundamentals and Applications. Mc Graw Hill, New York,NY.

Chanson,H .(1999) The Hydraulics of Open Channel Flow. Butterworth-Heinemann Woburn,Massachusetts.

Clark, M. (2009). "Physical model of a combined weir, sluice gate, and culvert control structure." Master's Thesis, University of Nebraska - Lincoln.

Cowen, E.A., and Monismith,S.G.(1997). "A hybrid digital particle tracking velocimetry technique." *Experiments in Fluid*, 22(199-211).

Felder, S., and Chanson, H. (2012). "Velocity and Pressure Measurements on a Broad-Crested Weir:Physical Measurement." *4th IAHR International Symposium on Hydraulic Structures,* Porto, Portugal.

Finnemore, E. J., and Franzini, J. B. (2002). Fluid Mechanics with Engineering Applications. McGraw-Hill, New York,NY.

Gonzalez, J.A (2005) Ratings for Pressurized Flow in Gated Culverts with Weir-Box Inlet G304A-J and G306A-J Technical Publication SHDM Report # 2005-02

Gonzalez, J.A (2007) Direct communication with Juan Gonzalez – slides provided from SFWMD.

Gonzalez, C. A., and Chanson, H. (2007). "Experimenatal measurements of velocity and pressure distribution on a large broad-crested weir." *Flow Meas.&Instr.,* 18 107-113.

Govinda Rao, N.S., and Muralidhar,D.(1963) "Discharge characteristics of weirs of finite-crest width", *Houille Blanche*, 18(5),537-545.

Hager, W. H. (1978). "Lateral outflow over side weirs." J.Hydr.Engrg., 113(4), 491-504.

Hager, W. H. (1999). Wastewater Hydraulics. Springer 1st Edition, Berlin, Germany.

Hager, W. H., and Schwalt, M. (1994). "Broad-Crested Weir." *J.Irrig.& Drain.Engrg.*, 120(1), 13.

Jesuthasan, N., Baliga, B. R., and Savage S.B. (2006). "Use of particle tracking velocimetry for measurements of granular flows: Review and application." *KONA,* (24), 15.

Keulegan,C.H.(1951). "Wind tides in small closed Cannels". *J.Res., Nat. Bur. Stand*, 46,358-381

King, H. W. (1918). Hand book of hydraulics for the solution of hydraulic problems. Hill Publishing Co.Ltd, London.

Lin, J. T., and Gad-El-Hak, M. (1984). "Turbulent current measurements in a windwave tank." *J. Geoph. Res.*, 89(1), 627-636.

Liu, C., and Tao, L. (2007). "Two-Dimentional Digital Particle Tracking Velocimetry Algorithm Based on the Image of Particle Trace." *J. Coastal Res.,* (50), 415-419.

Lloyd.P.M., B. D. J.,Stansby.P.K. (1995). "Unsteady surface-velocity field measurement using particle tracking velocimetry." *J. Hydraul. Eng,* 33(4), 519-533.

Masch.F.D. (1963). "Mixing and dispersion of waste by wind and wave action". *Int.J.Air and waste pollution*, 7, 697-720.

Mays, L. W. (2001). Stormwater collection systems design handbook. McGraw-Hill, New York.

Meselhe E.A., Bradley A.A., Kruger A., and Muste M.V.I. (1999). "Low flow measurements in streams using video imagery." *ASCE/EWRI,* 38(12), 51.

Muslu, Y. (2001). "Numerical analysis for lateral weir flow." *J.Irrig.& Drain.Engrg.,* 127(4), 246-253.

Rajaratnam, N., and Muralidhar, D. (1971). "Pressure and Velocity Distribution for Sharp-Crested Weirs." *J. Hydr. Res.,* 9(2), 241-248.

Ramamurthy, A. S., Qu, J., and Vo, D. (2006). "Non-linear PLS method for side weir flows." *J.Irrig.& Drain.Engrg.,* 132(5), 486-489.

Ranga Raju, K. G., Prasad, B., and Gupta, S. K. (1979). "Side weir in rectangular channel." *J.Hydr.Div.,* 105(5), 547-554.

Rehbock,T., "Wassermessung mit Scharf kantigen ueberfallwehren." *Z Ver.dtsch Ing.*,73,817-823 (1929).

Roberson,J.A.,Crowe,T.C.(1985). Engineering Fluid Mechanics, Third Edition. Houghton Mifflin Company, Boston.

Ruhnau, P., Guetter, C., and Putze, T. (2005). "A variational approach for particle tracking velocimetry." *Meas. Sci. Technol.,* 16 1449-1458.

Singer,J.,(1964) "Square-edged broad-crested weir as a flow measurement device." *Water and Water engineering*, 28,No.820,229-235.

Singh, R., Manivannan, D., and and Satyanarayana, T. (1994). "Discharge coefficient of rectangular side weirs." *J.Irrig.& Drain.Engrg.,* 120(4), 814-819.

Sokoray-Varga, B., and Jorza, J. (2008). "Particle tracking velocimetry(PTV) and its application to free surface flows in laboratory scale models." *Peer. Pol. Civil Eng,* 2(52), 63-71.

SonTek. (2001). "Acoustic Doppler Velocimeter (ADV) SonTek 10-MHz." http://www.sontek.com/10mhzadv.php (March/18, 2012).

Subramanya, K., and Awasthy, S. C. (1972). "Spatially varied flow over side-weirs." *J.Hydr.Div.,* 98(1), 1-10.

Teledyne Isco. (2009). "ADFM® Pro20 Velocity Profiler *For large pipes and open channels*." http://www.isco.com/products/products3.asp?PL=2022010 (March/18, 2012)

Tang,F.L.W., Wu,J., and Chang,C.C.(1978)."Wind-induced water surface set-up and drift currents." *Coastal Engineering*, **48**, 841-858.

Tsanis,I.(1989), "Simulation of wind-induced water currents." *J.Hydraul.Eng* 115(8),1113-1134.

Tsuruya, H., Nakamo, S., and Kato, H. (1985). "Experimental study on wind driven current in a wind-wave tank—Effect of return flow on wind driven current." *The Ocean Surface*, 425-430.

Wu, J. (1975). "Wind-Induced Drift Currents". *J. Fluid Mech.*, 68(1), 49-70

Weather Underground,Inc.(2013).http://www.wunderground.com/q/zmw:33480.1.99999

Appendix A. High Density Vector Plots in the Prototype

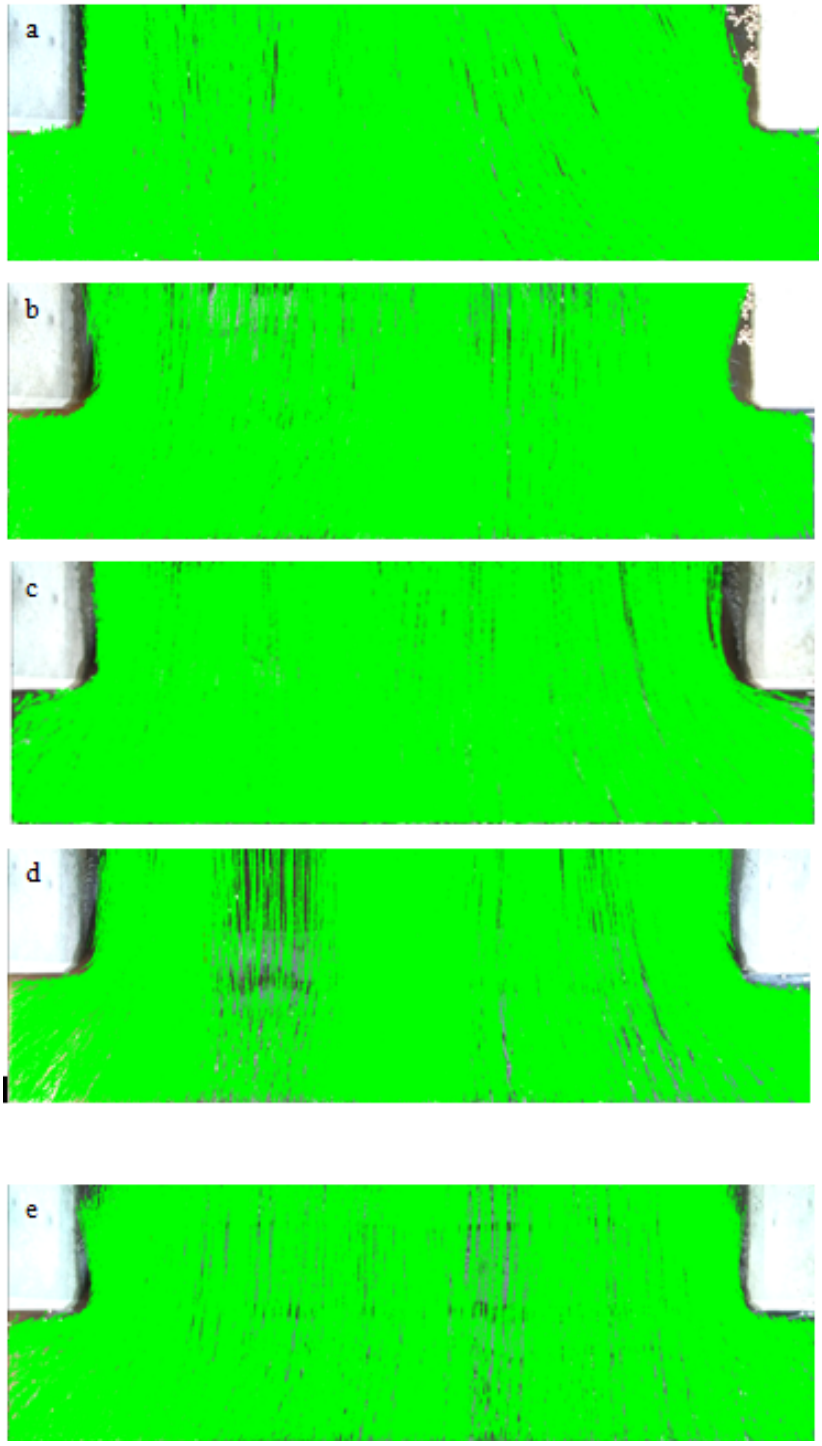

Figure A.1 Surface velocity distribution plots for the prototype for (a) Test A2, (b) Test A3, (c) Test A4, (d) Test A5, and (e) Test A6

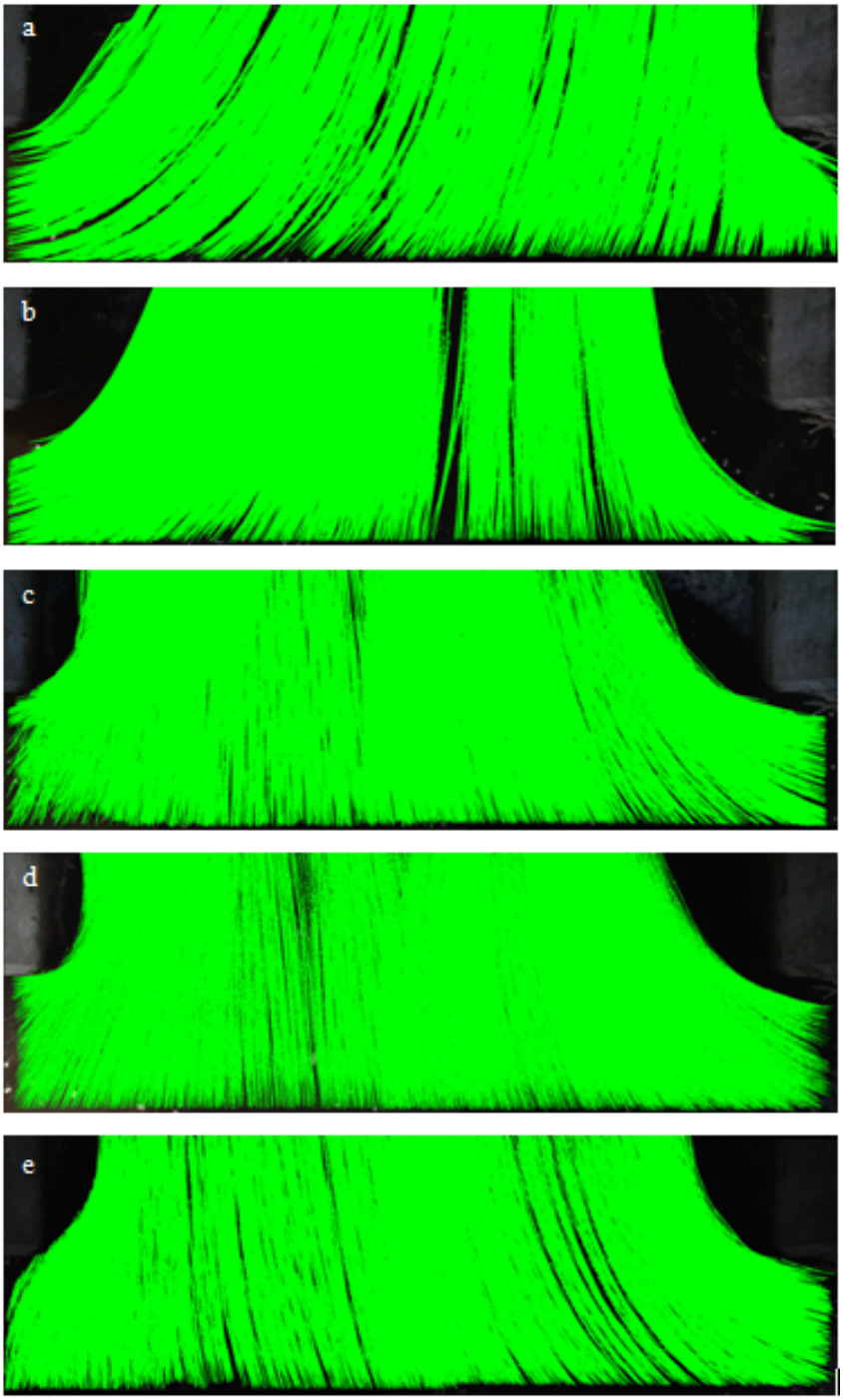

Figure A.2 Surface velocity distribution plots for the prototype for (a) Test B2, (b) Test B3, (c) Test B4, (d) Test B5, and (e) Test B6

Appendix B. Contours of Surface Velocity Magnitudes in the Prototype

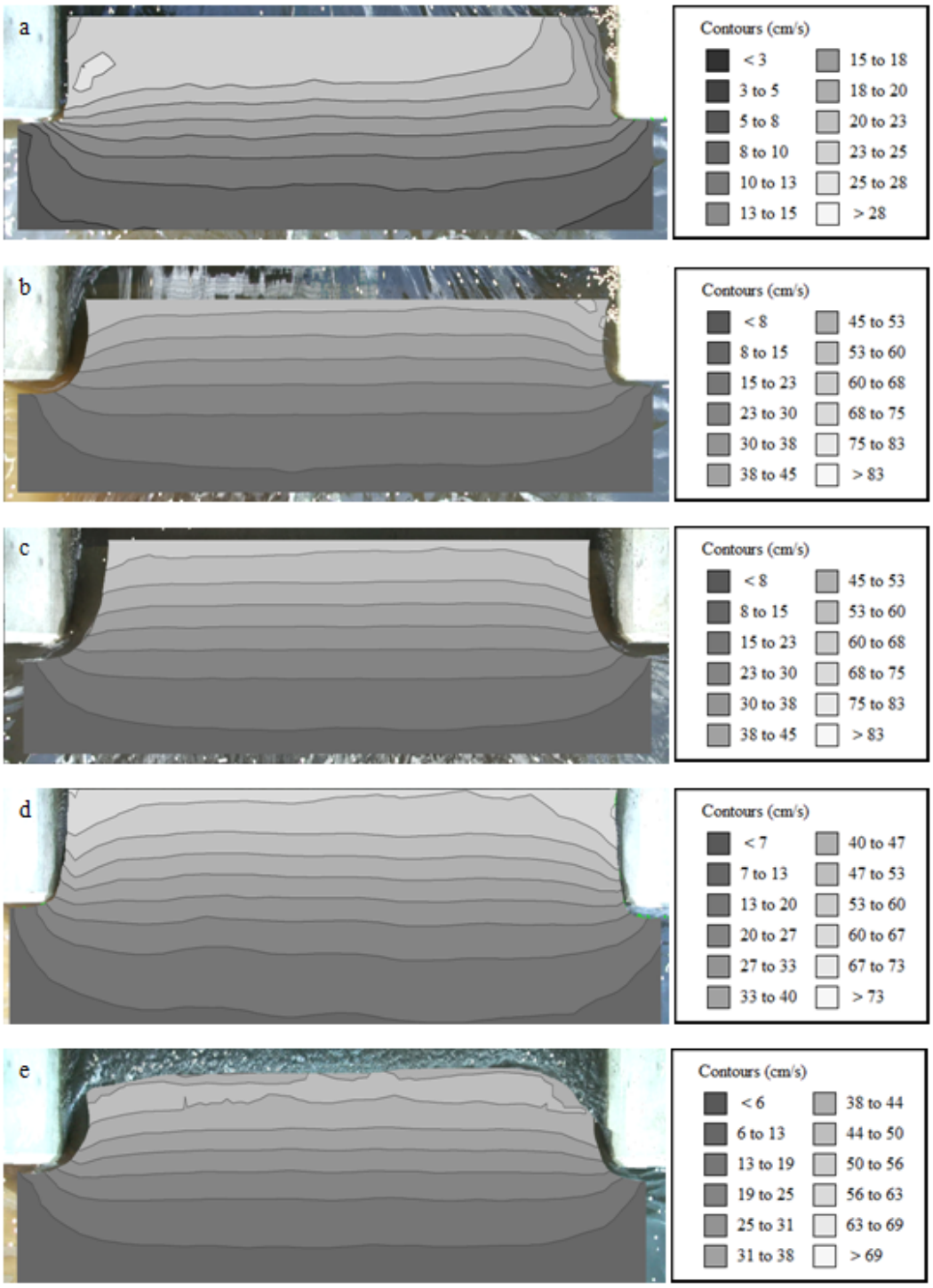

Figure B.1 Surface velocity contour plots for the prototype for (a) Test A2, (b) Test A3, (c) Test A4, (d) Test A5, and (e) Test A6

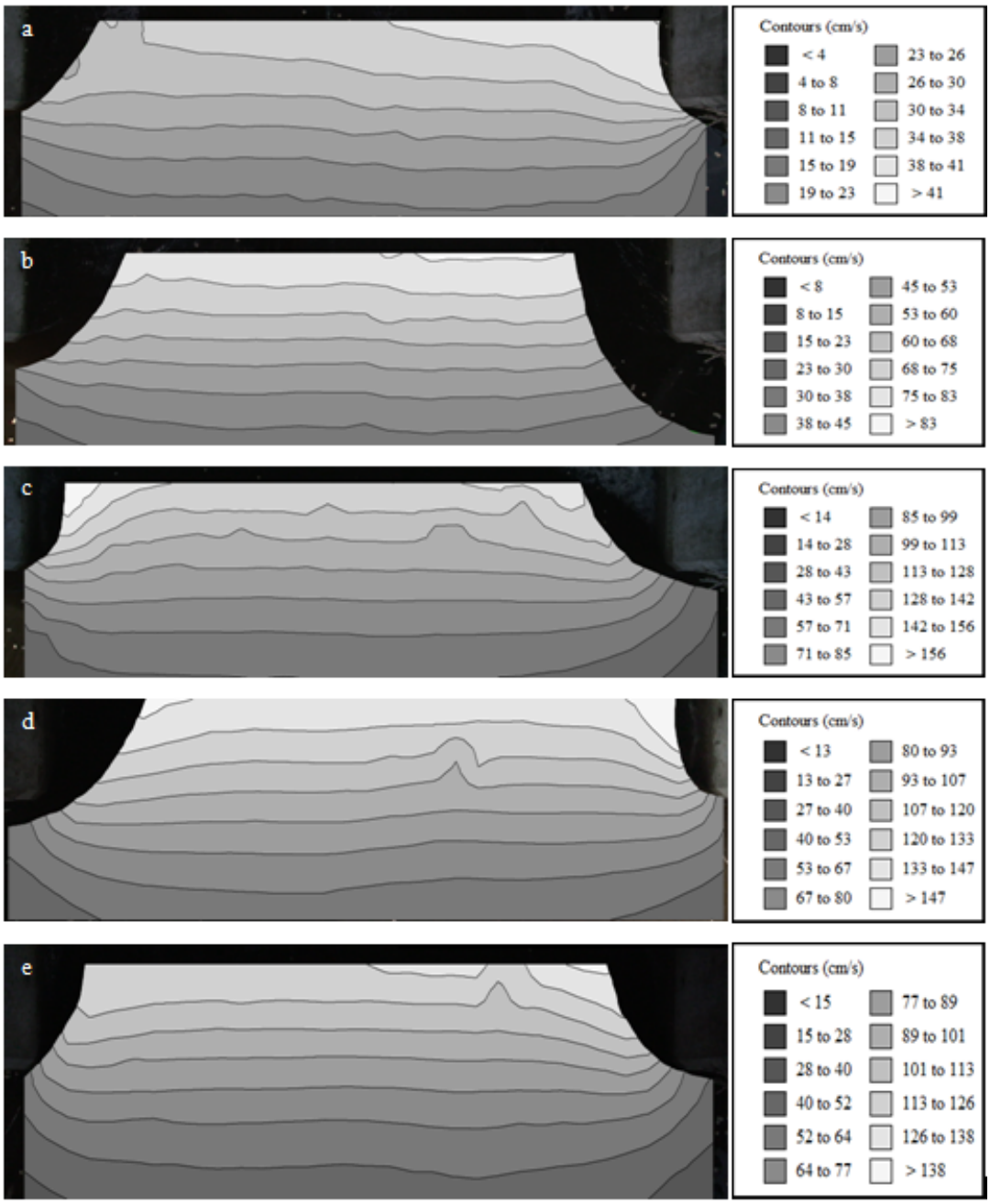

Figure B.2 Surface velocity contour plots for the prototype for (a) Test B2, (b) Test B3, (c) Test B4, (d) Test B5, and (e) Test B6

Appendix C. Locally Averaged Velocity Transects in the Prototype

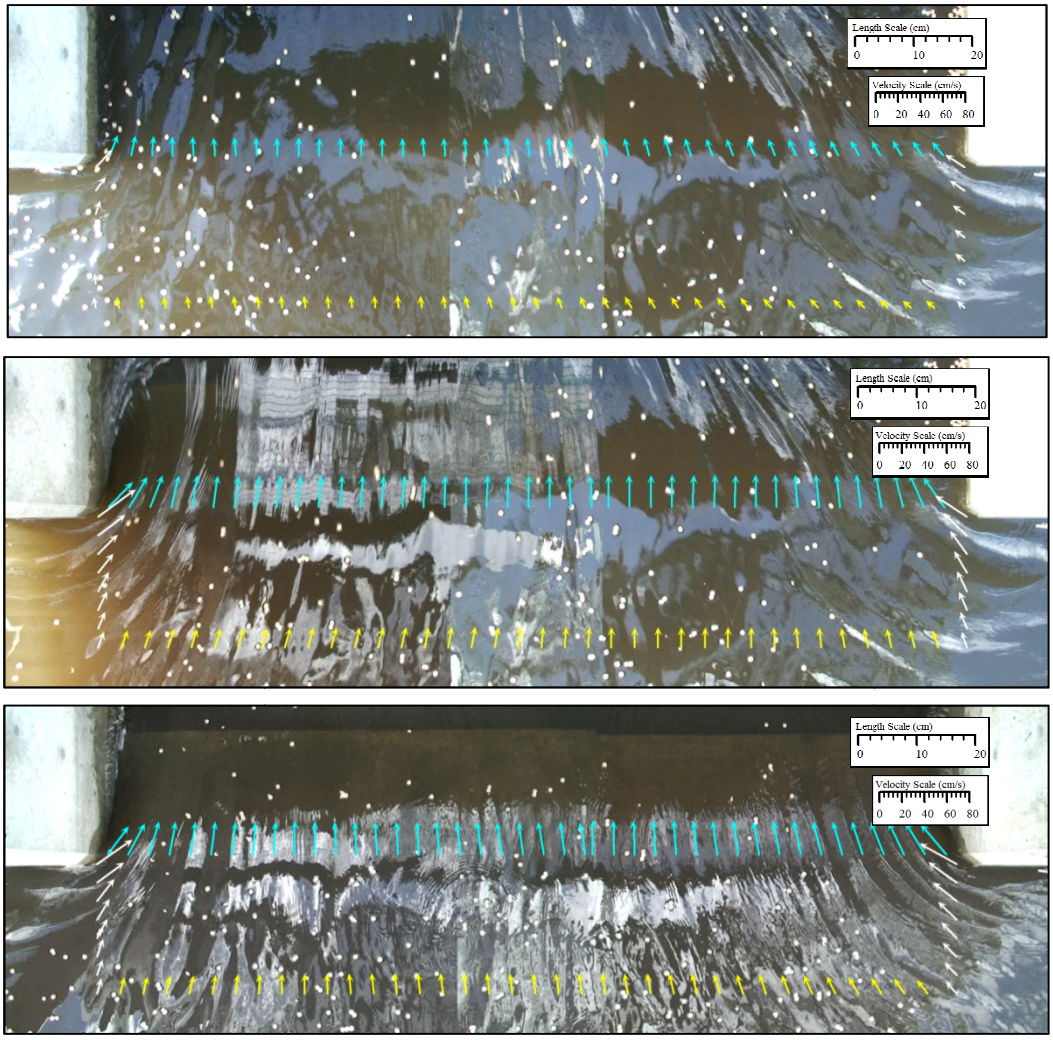

Figure C.1 Average surface velocity plots for the prototype for (a) Test A2, (b) Test A3, (c) Test A4

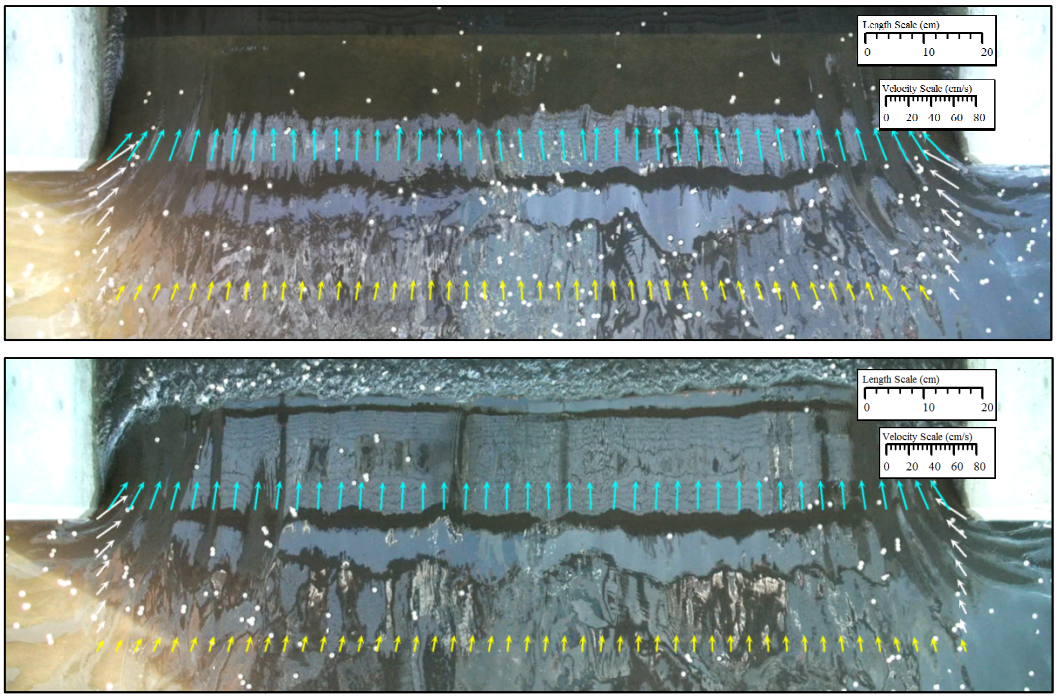

Figure C.1 (cont.) Average surface velocity plots for the prototype for (d) Test A5, (e) Test A6

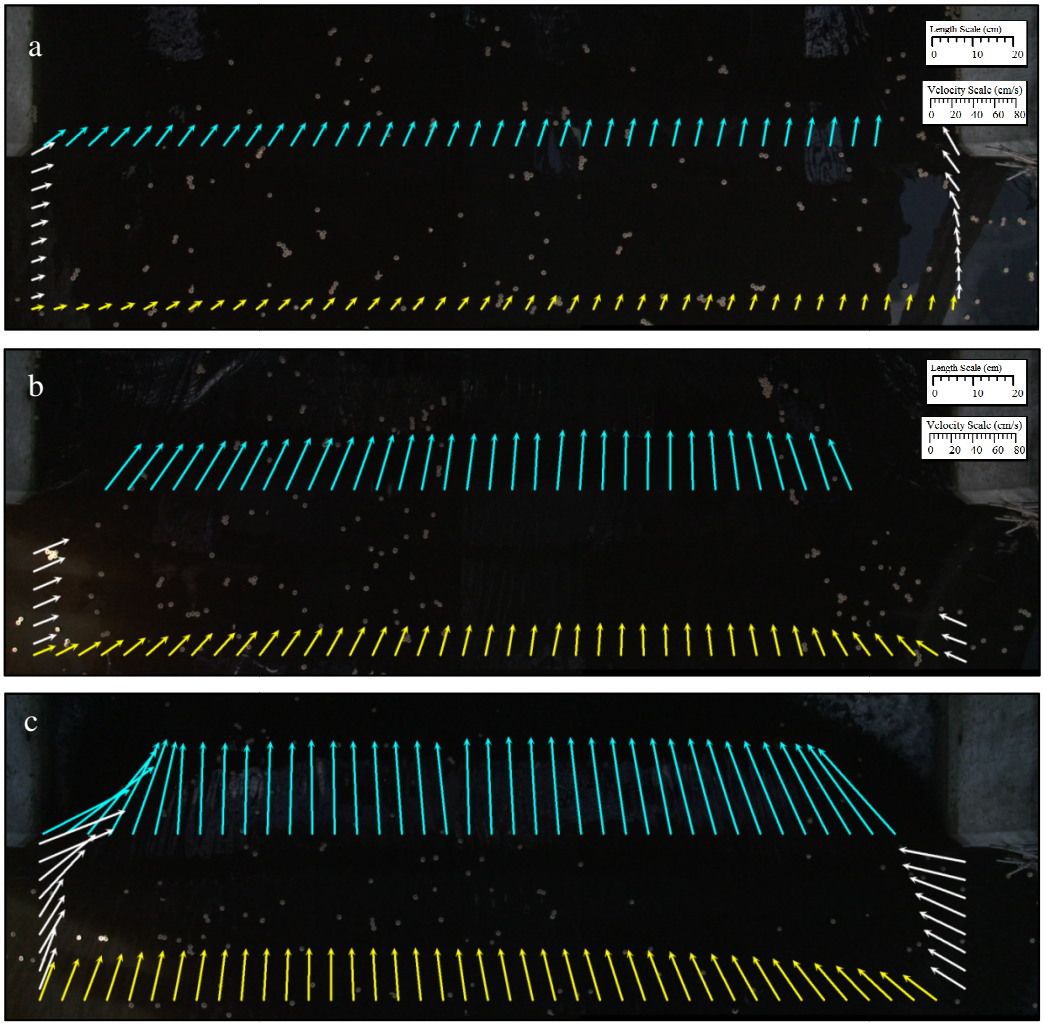

Figure C.2 Average surface velocity plots for the prototype for (a) Test B2, (b) Test B3, (c) Test B4

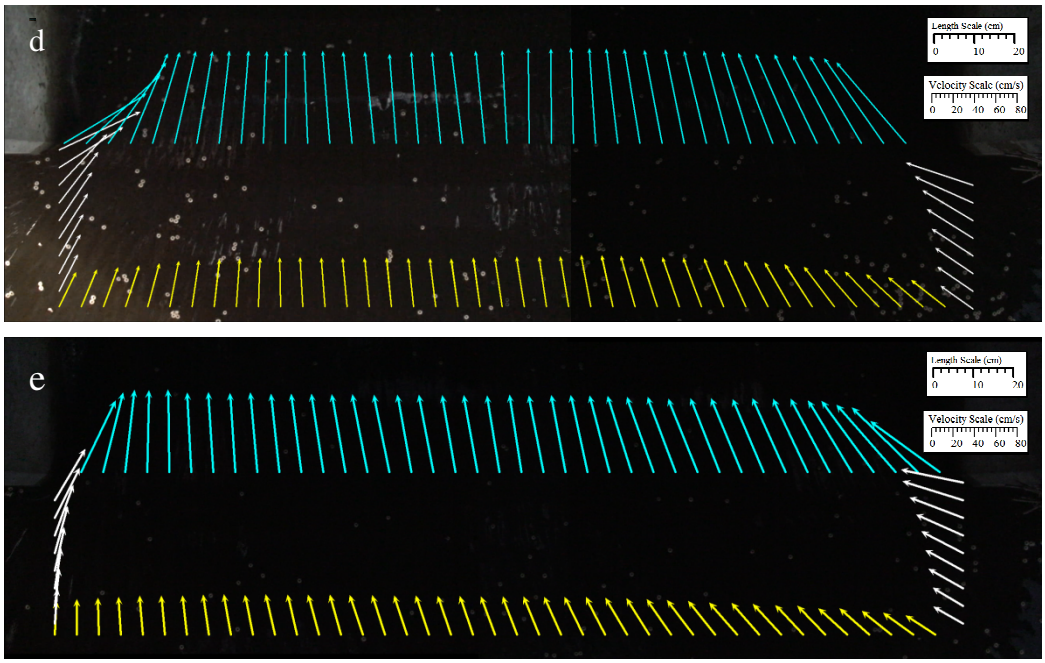

Figure C.2 (cont.) Average surface velocity plots for the prototype for (d) Test B5, (e) Test B6

Appendix D. High Density Vector Plots in the Model

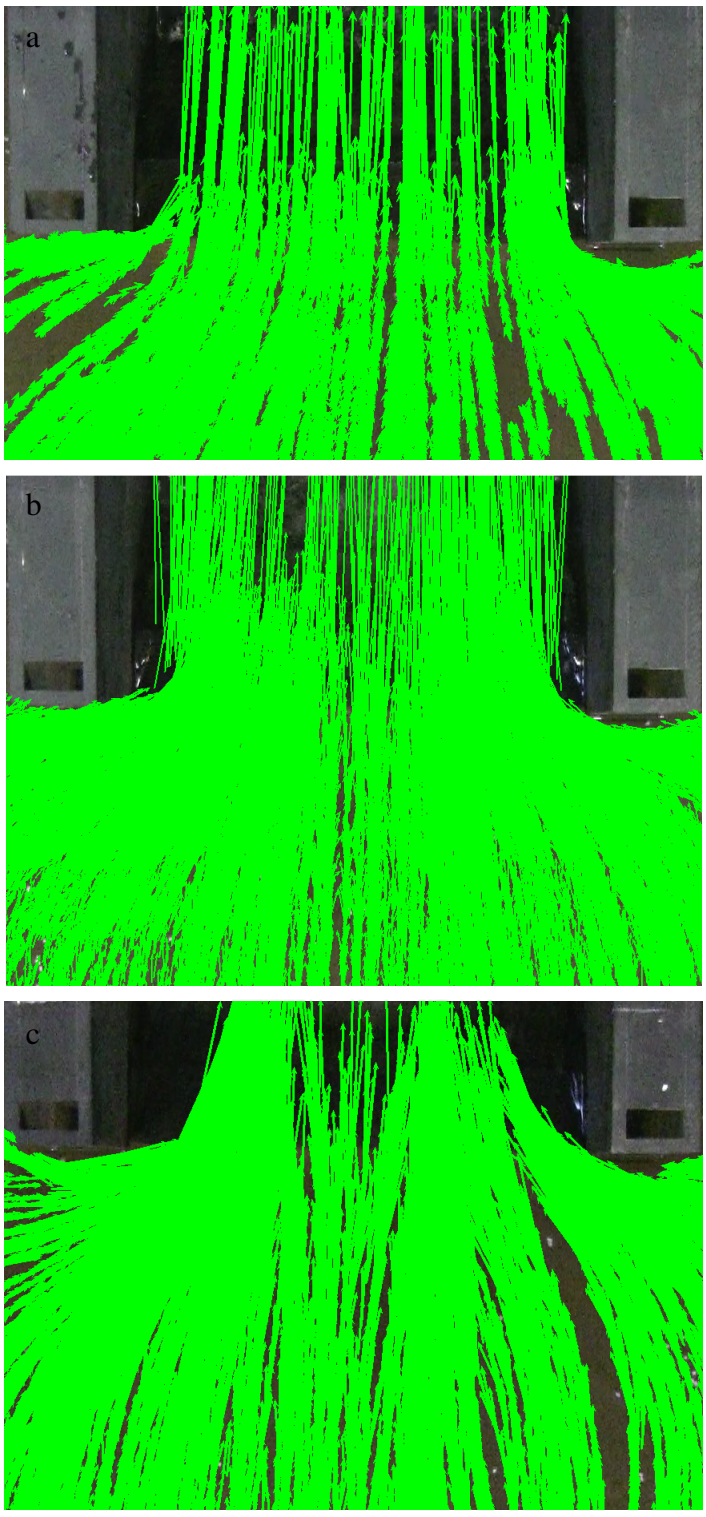

Figure D.1 Surface velocity distribution plots for the prototype for (a) Test 1, (b) Test 2, (c) Test 3

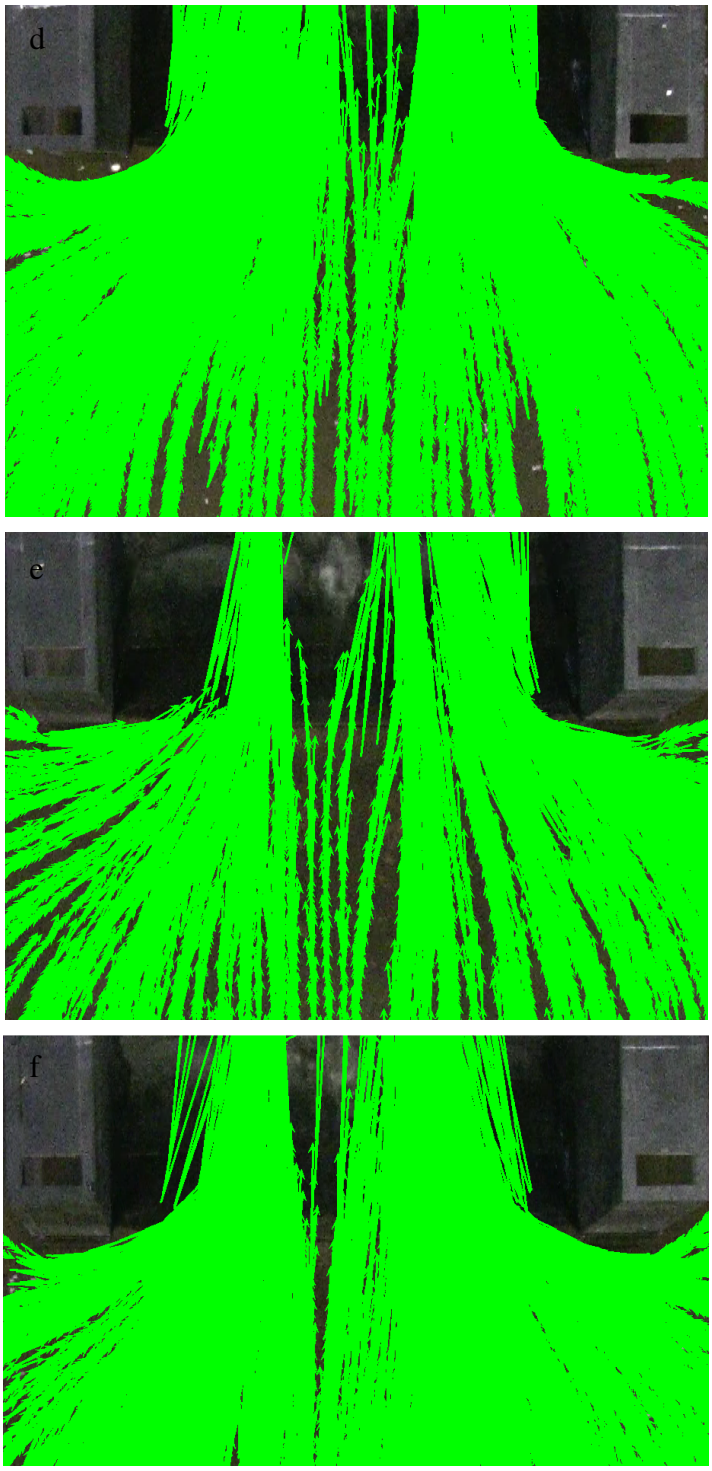

Figure D.1 (cont.) Surface velocity distribution plots for the prototype for (d) Test 4, (e) Test 5, (f) Test 6

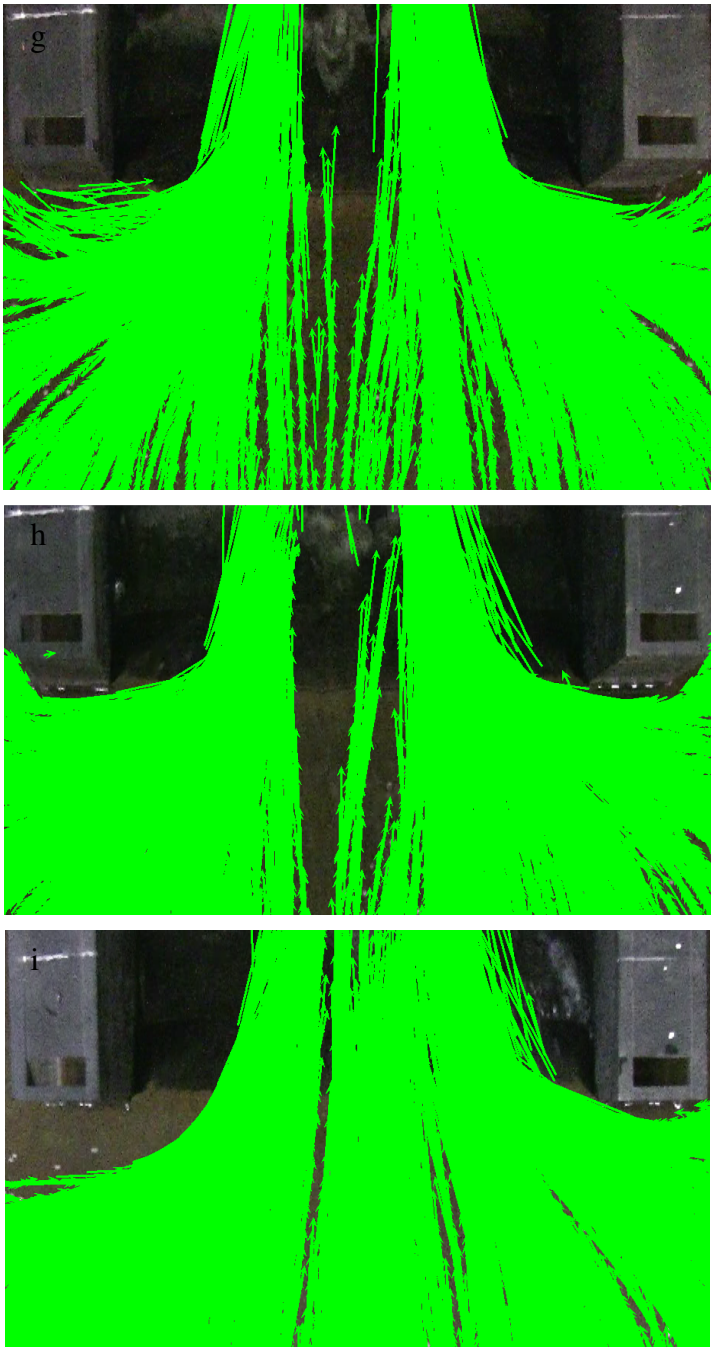

Figure D.1 (cont.) Surface velocity distribution plots for the prototype for (g) Test 7, (h) Test 8, (i) Test 9

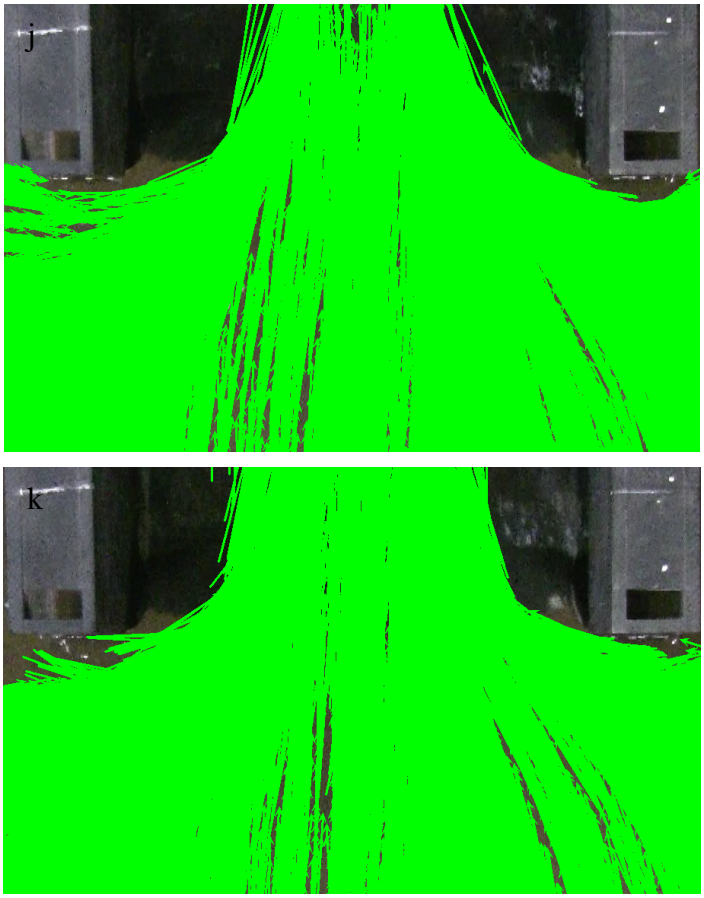

Figure D.1 (cont.) Surface velocity distribution plots for the prototype for (j) Test 10, (k) Test 11,

Appendix E. Contours of Surface Velocity Magnitudes in the Model

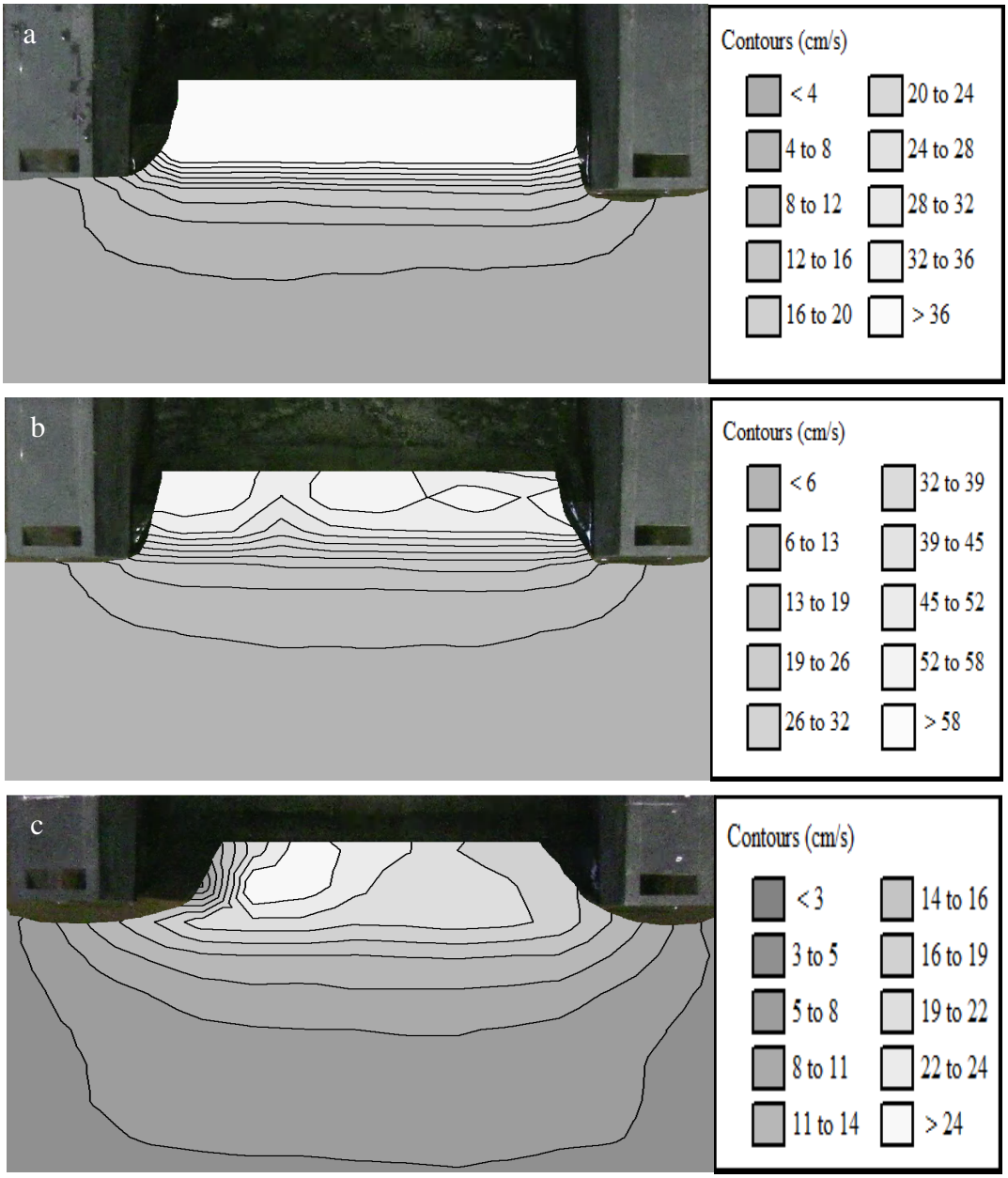

Figure E.1 Surface velocity distribution plots for the prototype for (a) Test 1, (b) Test 2, (c) Test 3

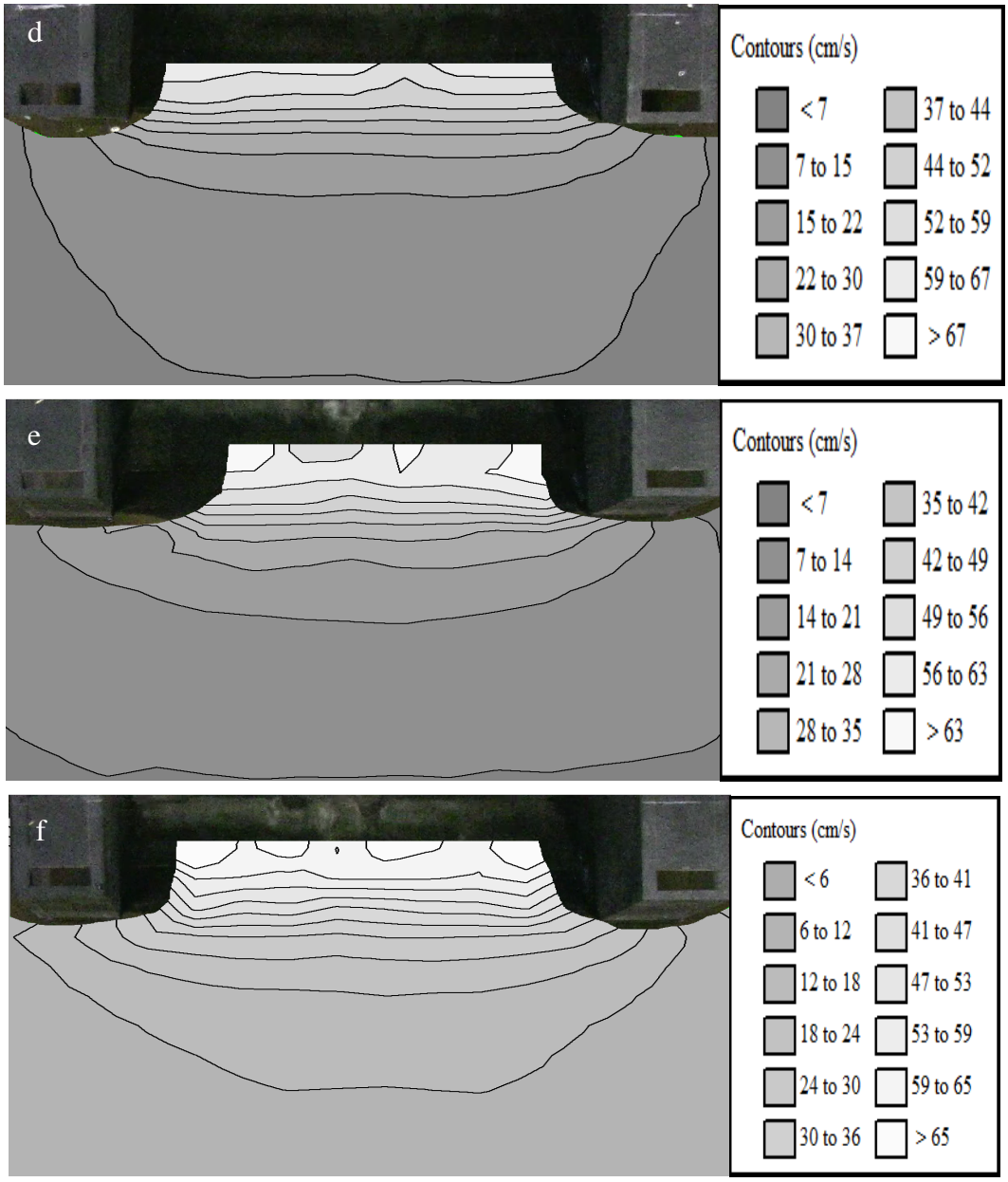

Figure E.1 (cont.) Surface velocity distribution plots for the prototype for (d) Test 4, (e) Test 5, (f) Test 6

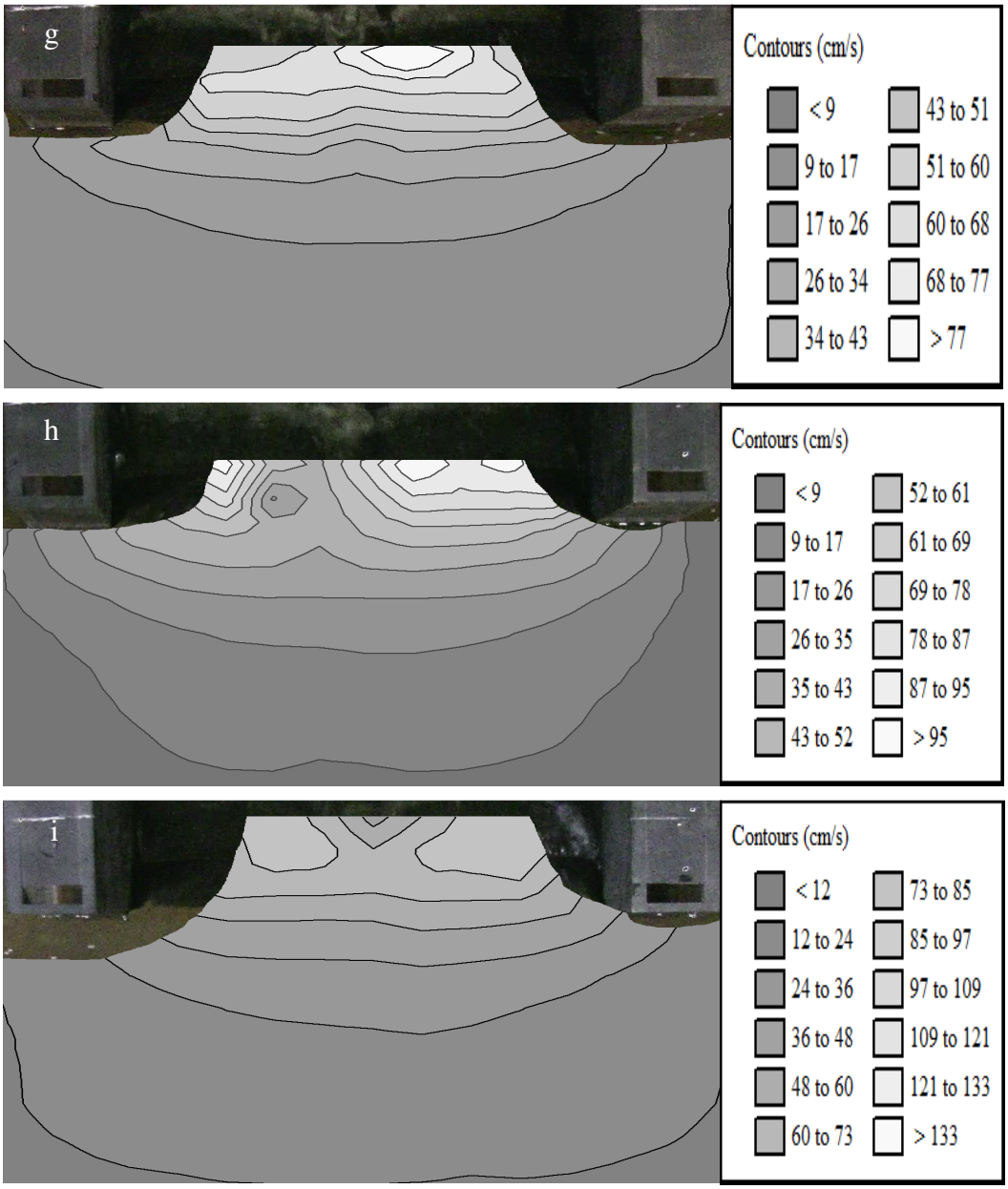

Figure E.1 (cont.) Surface velocity distribution plots for the prototype for (g) Test 7, (h) Test 8, (i) Test 9

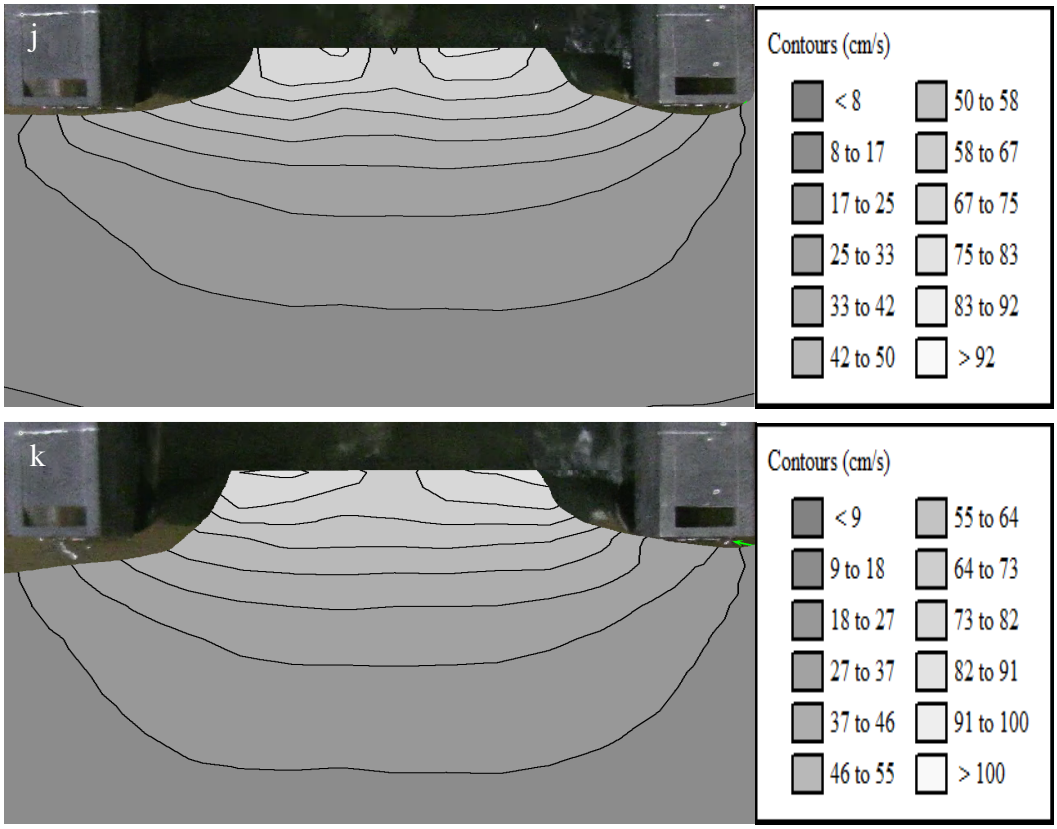

Figure E.1 (cont.) Surface velocity distribution plots for the prototype for (j) Test 10, (k) Test 11

Appendix F. Locally Averaged Velocity Transects in the Model

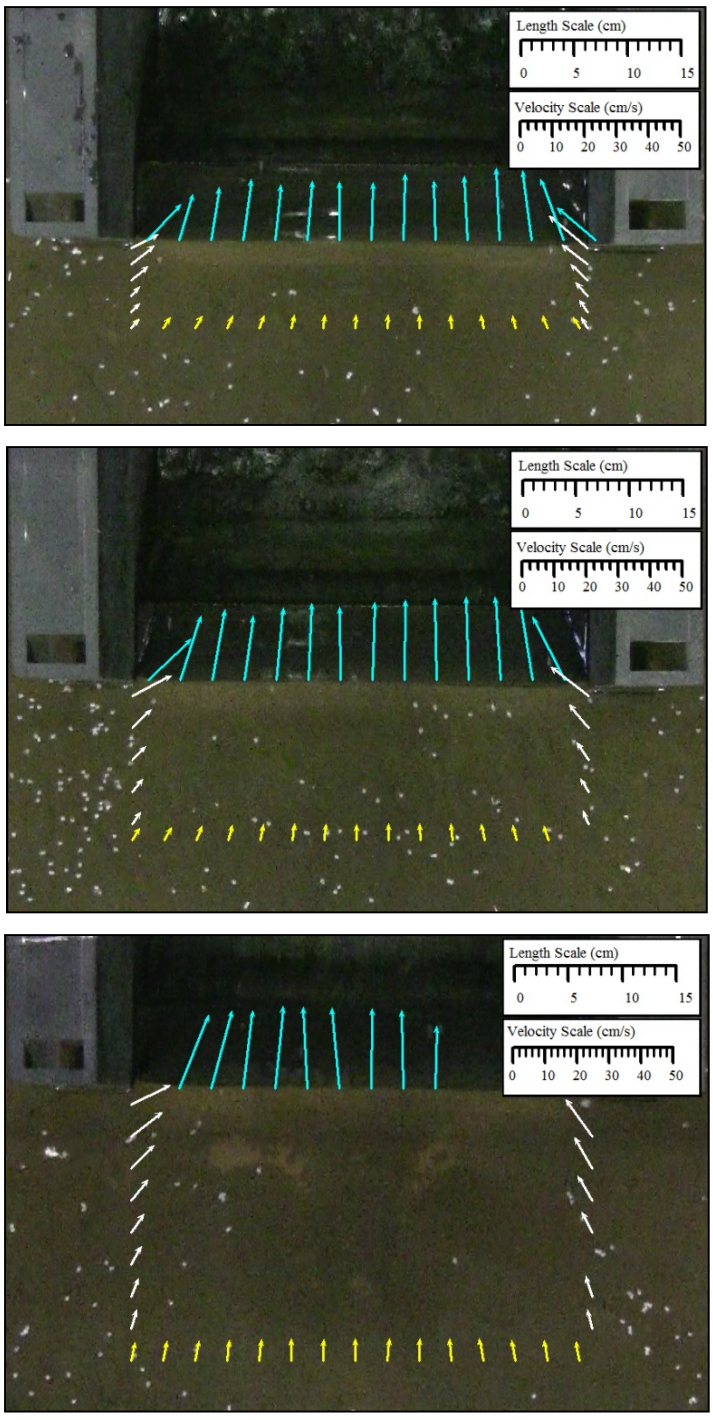

Figure F.1 Average surface velocity plots for the prototype for (a) Test 1, (b) Test 2, (c) Test 3

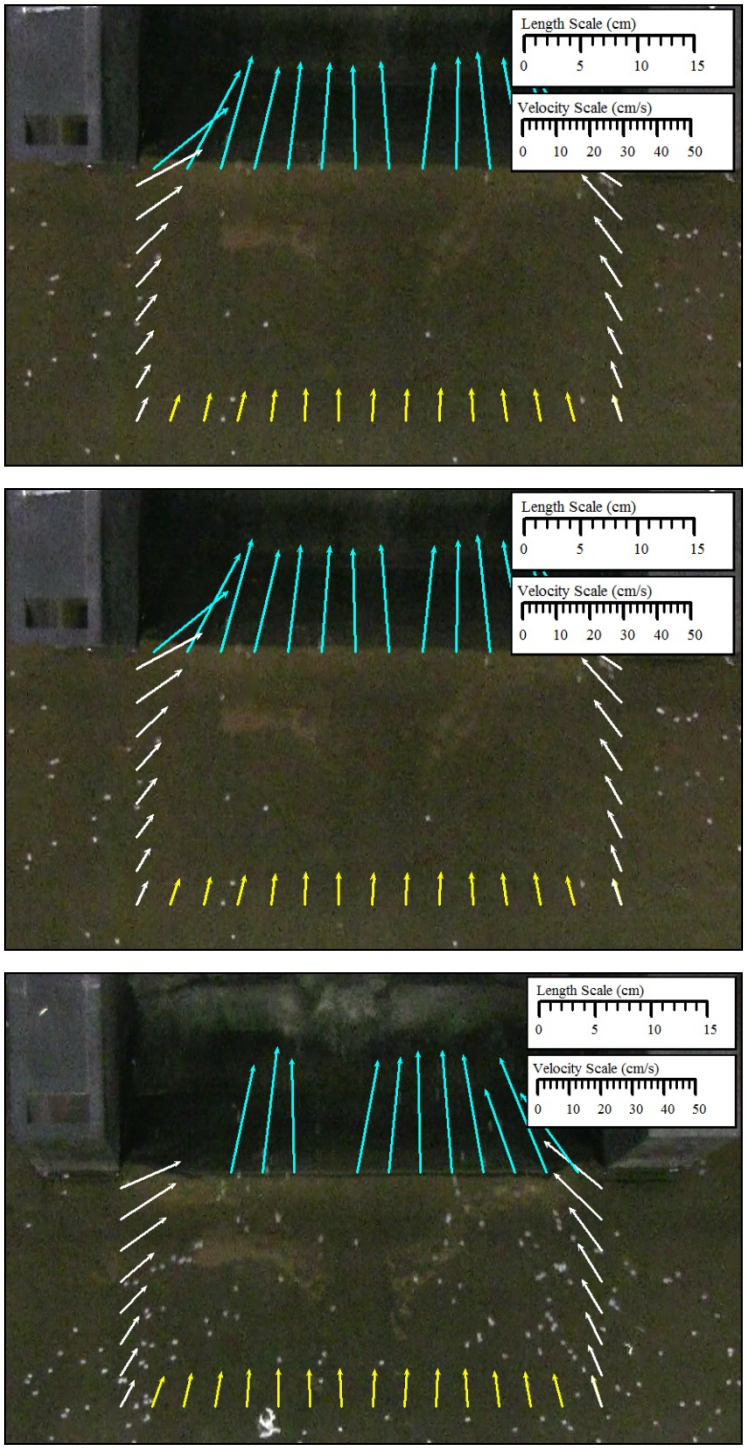

Figure F.1 (cont.) Surface velocity distribution plots for the prototype for (d) Test 4, (e) Test 5, (f) Test 6

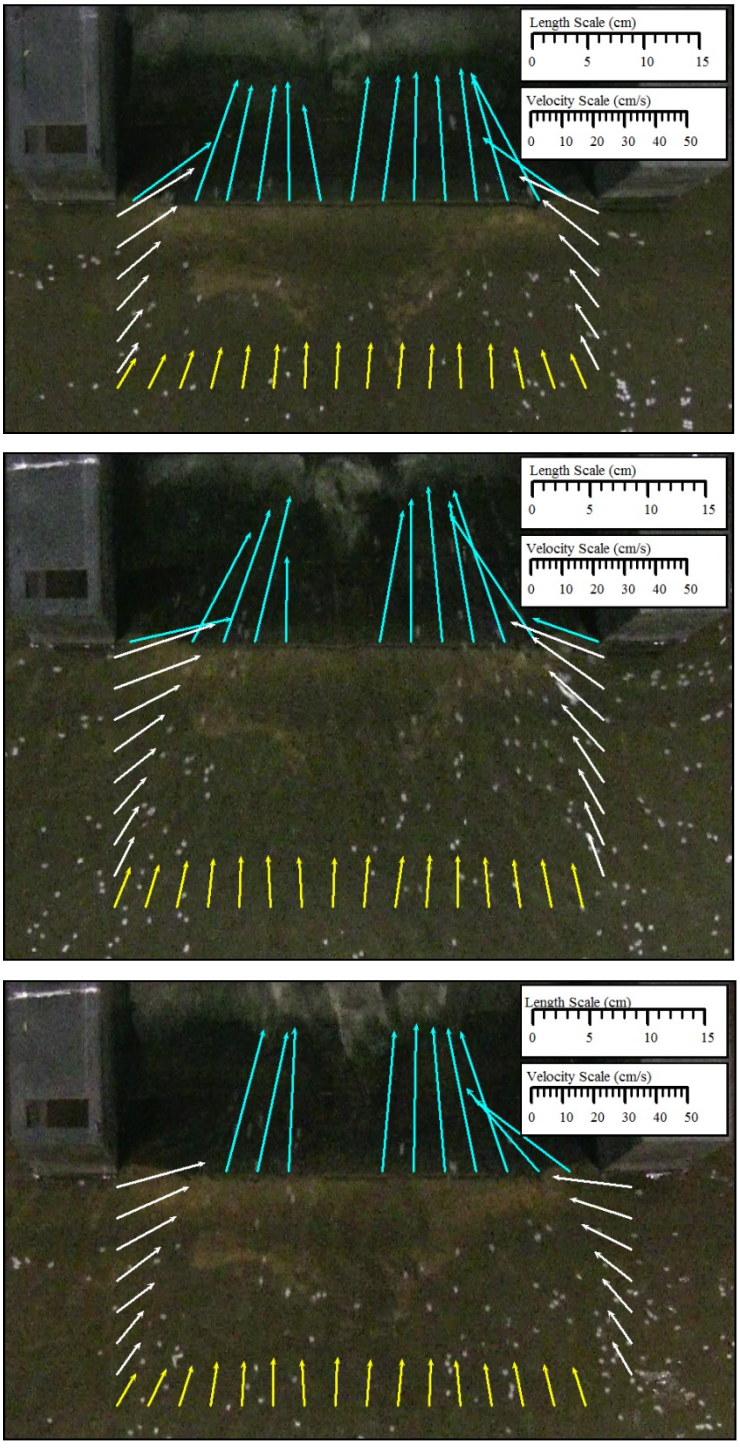

Figure F.1 (cont.) Surface velocity distribution plots for the prototype for (g) Test 7, (h) Test 8, (i) Test 9

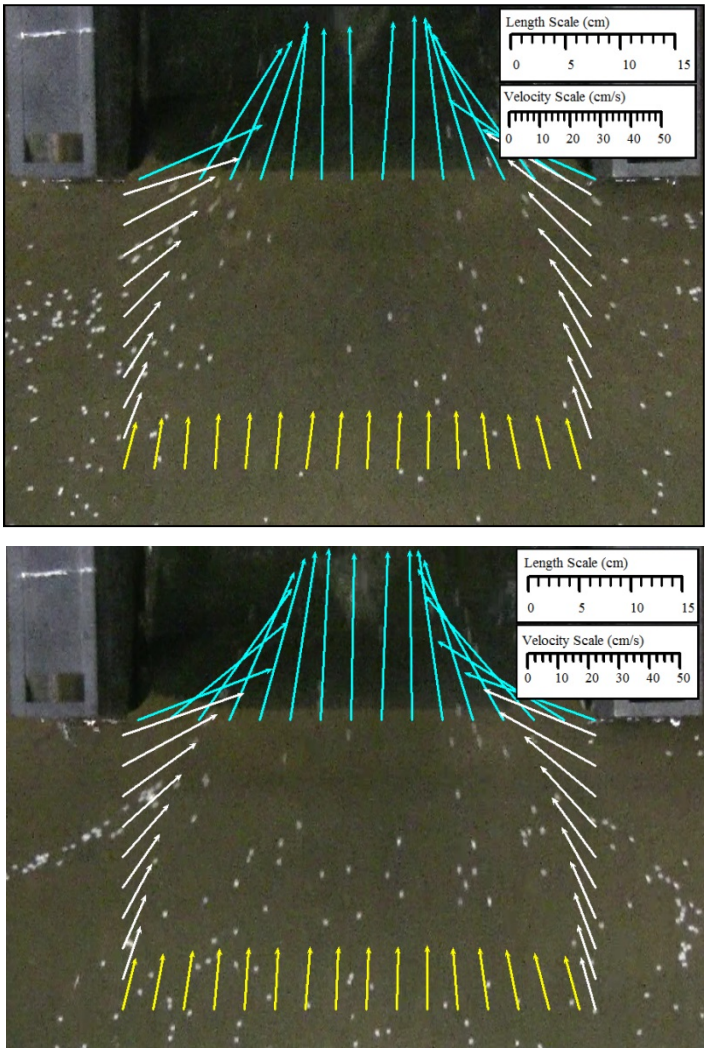

Figure F.1 (cont.) Surface velocity distribution plots for the prototype for (j) Test 10, (k) Test 11